THE UNIVERSITY *of* EDINBURGH

THE UNIVERSITY *of* EDINBURGH
School of Engineering

Contact models for Discrete-Element Method simulations of non-spherical particles

Stephanos Constandinou

(Supervisors: Kevin Hanley & Jane Blackford)

Doctor of Philosophy
The University of Edinburgh
December 27, 2023

Abstract

Computational modelling of granular systems has increased significantly in recent years, particularly using the Discrete-Element Method (DEM), a simulation tool proposed by Cundall & Strack (1979). In the most common implementation of DEM, particles are modelled as rigid bodies, for which the deformations at the contact points are captured by permitting overlaps between the interacting particles. These correlations between force and overlap are referred to as 'contact models'.

Particles in 3D DEM simulations are generally modelled as spheres because of their computational simplicity. Particle shape though is an important factor, causing a major increase in scientific interest in DEM modelling of non-spherical particle systems. One of the greatest limitations of using non-spherical particles in DEM modelling is the lack of appropriate mathematical relationships between the contact force and interparticle overlap. For this reason, contact models suitable for spheres are usually adopted which is not physically justifiable.

One of the most common methods of emulating non-spherical granules is the Multi-Spherical (MS) approach, where a number of spheres are 'glued' together in a cluster in order to construct a more complex shaped granule. Such an approach, however, leads to two sources of errors: (i) the contact model error arising from adopting a contact model suitable for individual spheres and (ii) the shape approximation error arising from modelling a specific desired particle shape using a finite number of spheres. Taking spherocylinders as an exemplar shape, a Finite Element Analysis (FEA) study was conducted to quantify both sources of errors. The study focused on the force responses obtained from the uniaxial compression of spherocylinders and the collisions between two identical spherocylinders. It should be noted that only the normal contact forces are considered in this thesis and any tangential interactions were disregarded.

For the contact model error, the rods used in the tests consisted of three spheres and had a variable aspect ratio by adjusting the sphere overlaps between the constituent spheres. The force response comparison was performed between the FEA results of MS rods and the results that would have been obtained in a DEM setting when different contact models were applied. A number of contour plots were generated showcasing the errors of 3 different contact models: Hertz, Hooke, Tatara. For the shape approximation error all granules tested had a fixed aspect

ratio of 3:1. The force response comparison was performed entirely using FEA where the force responses of MS rods with a variable number of spheres was compared against that of a perfect spherocylinder. A number of contour plots were generated showcasing the errors as the number of constituent spheres increases. The results indicate that the MS approach with spherical contact models should generally be avoided for contact overlaps exceeding 1.5% of the constituent spheres' diameters. Additionally, while greater sphere overlaps mean more accurate shape representation, sphere overlaps of 60% should not be exceeded if contact models designed for spheres are to be used.

Going beyond distance-overlap based contact models, two volume-overlap based contact models were evaluated by performing indentation tests on a spherical granule with different shaped indenters using FEA. The energy-conserving model proposed by Feng (2021c) [Feng, Y. T. (2021c). An energy-conserving contact theory for discrete element modelling of arbitrarily shaped particles: Contact volume based model and computational issues. *Computer Methods in Applied Mechanics and Engineering* **373**, 113493, doi: 10.1016/j.cma.2020.113493] cannot be recommended for practicality reasons. A linear volume-based model though seems like a better alternative since the stiffness index constant k is independent of the contacting bodies' shapes according to the FEA conducted. However, both models rely on calculating an accurate contact volume overlap which is difficult to obtain for arbitrary shapes and not in good agreement with the deformed volume obtainable from FEM.

Finally, the influence of the Poisson effect on the stress dependence of the elastic moduli of soil was examined. Hertzian spheres neglect the Poisson effect, so it was examined whether this omission contributes to the inability of smooth-sphere DEM simulations to correctly capture the stress dependence of the elastic moduli of soil. This was done by isotropically compressing a spherical granule of silica sand using FEM. At low-to-moderate confining stresses the Poisson effect had a measurable but very limited influence. It was found that the Poisson effect became significant only at confining stresses on the order of 100 MPa. Thus, at lower stresses, rough-surface contact models remain the most justifiable way to match the stress–stiffness response measured in laboratory testing using DEM simulations.

Lay Summary

Granular flows are everywhere, spanning industries from agriculture to pharmaceuticals and even natural phenomena like landslides. Understanding and predicting the behaviour of these granular materials is critical for various applications. The challenge lies in their intricate dynamics, where individual particles interact in ways that are not always intuitive. This thesis focuses on the inner workings of the Discrete-Element Method (DEM), a powerful computational tool that can predict the behaviour of individual particles within a granular system. Modelling the behaviour of granular materials becomes notably challenging when dealing with non-spherical particles.

One of the primary hurdles is the lack of suitable mathematical relationships that accurately depict how contact forces between these particles correspond to their deformations. These mathematical relationships, known as contact models, pose a challenge in scenarios where the shape of the particles deviates from perfect spheres. In such cases, a common approach involves 'gluing' together a number of spheres to form irregular-shaped particles, while still using the common contact models that were designed for spheres. However, the extent to which predictions obtained by this method diverge from reality is not clear. This aspect is thoroughly investigated in this thesis. Additionally, another variation of contact models that rely on the volumetric deformations is investigated and the force predictions of the volume-based contact models is compared with the force predictions of the conventional contact models. Finally, the factors responsible for how the elasticity of soil responds to stress are examined.

Declaration

I declare that this thesis is my original work except where explicitly stated otherwise, and that this work has not been submitted for any other degree or professional qualification except as specified.

Publication

Constandinou, S. & Hanley, K. J. (2022). Influence of the Poisson effect on the stress dependence of the elastic moduli of soil. *Géotechnique Letters* **12**, No. 1, 80–84, doi: 10.1680/jgele.21.00135

Signed:

Stephanos Constandinou, June 5, 2024

Acknowledgements

First and foremost I would like to thank my supervisor, Kevin Hanley, for his support over the last four years. Thank you for granting me the freedom to pursue any idea no matter how silly it sounded, while always being there to guide me until the very end. I could not have asked for a better supervisor. None of this would have been possible without your help and for this thank you.

I would like to thank Jane Blackford for all her feedback and the fruitful discussions we had over the years. Many thanks to Francisca Martinez-Hergueta for her patience, guidance and willingness to help me get started using FEM and providing me with all the tools I needed to fulfil my research objectives. On that I would also like to thank Stefanos Papanicolopulos for his advice and input on the FEM modelling. I would like to thank Oguzhan Erken for his help with the DEM simulations, that is greatly appreciated. I would also like to thank Lev Sarkisov for planting the "seed" of pursuing research in my head and pushing me to do my best before I even started this journey.

A big thank you to my friends George, Athina, Helena, Nerea and Alan that kept me sane during the pandemic times, whether that was long walks or board game nights (rule permitting, always!). A massive thank you to Yiangos for always having my back and patiently listening to me go on about problems with simulations, writing, marking or just in general seeking life advice.

I would like to offer a big thank you to all the wonderful people I met that helped me unwind during the last stressful year, be it through dancing or all the music jams. I would like to especially thank Harry and Dara for being the kindest souls and Frauke for looking after me. Last but not least, I would like to thank my family, who even though still struggle to understand what I actually do, they have always been supporting me in their own way.

Contents

Abstract i

Lay Summary iii

Declaration v

Acknowledgements vii

List of Figures xiii

List of Tables xxi

1 Introduction 1

1.1 Scope . . . 2

1.2 Thesis outline . . . 3

2 Literature review 5

2.1 Discrete-Element Method (DEM) . . . 5

2.1.1 DEM Theory . . . 6

2.2 Particle shapes in DEM . . . 8

2.2.1 Ellipsoids . . . 8

2.2.2 Superquadrics . . . 9

2.2.3 Spherocylinders . . . 9

2.2.4 Polyhedra . . . 10

2.2.5 Spherical Harmonics . . . 10

2.2.6 Multi-Spherical clumps . . . 11

2.2.7 Level sets . . . 12

2.2.8 Potential Particles . . . 12

2.3 Contact Models commonly used in DEM . . . 13

2.3.1 Hertz (spheres) . . . 13

2.3.2 Linear Contact Model . . . 15
2.4 Other Contact Models . . . 15
2.4.1 Tatara . . . 15
2.4.2 Feng . . . 16
2.4.3 Dintwa . . . 17
2.4.4 Hertz (ellipsoids) . . . 17
2.4.5 Kumar . . . 18
2.4.6 Aspherix Advanced Multi-Sphere Method . . . 20
2.5 Contact models employing the Multi-Sphere approach . . . 21
2.6 Soil mechanics application of DEM . . . 22
2.7 Contact model usage and knowledge gaps . . . 23

3 Methodology **25**
3.1 Uniaxial compression of a sphere . . . 25
3.2 Kinematic collisions of a sphere . . . 30
3.3 Mesh dependence study . . . 31
3.3.1 Mesh dependence study: Quasi-static compression results . . . 32
3.3.2 Mesh dependence study: Kinematic collision results . . . 34

4 Multi-Spherical Errors **37**
4.1 Simulation-Model Setup . . . 40
4.1.1 Angled Collisions: Kinematic Collisions . . . 40
4.1.2 Parallel Contacts: Quasi-static Compressions . . . 42
4.2 Contact Model Errors . . . 42
4.2.1 Preliminary Study: Parallel contact of two-sphere rods . . . 44
4.2.2 Three-sphere rod contacts . . . 46
4.2.2.1 Hertz model multi-spherical error evaluation . . . 49
30° contour plot . . . 49
45° contour plot . . . 49
60° & 90° contour plots . . . 52
4.2.2.2 Tatara model multi-spherical error evaluation . . . 52
30° contour plot . . . 55
45° contour plot . . . 55
60° & 90° contour plots . . . 55
4.2.2.3 Linear (Hooke) model multi-spherical error evaluation . . . 56
4.2.2.4 Aspherix Advanced Multi-Sphere Method . . . 60
4.2.2.5 Expanded Point of Contact regions . . . 60
4.3 Shape Approximation Errors . . . 64
4.3.1 Fixed-Length Multi-Spherical Rods vs. Perfect Spherocylinder . . . 66

4.4 Optimal rod configuration . . . 72
4.5 Multi-Spherical errors conclusions . . . 73

5 Volume vs. Distance Overlap **75**
5.1 Volume overlap-based contact models . . . 75
5.1.1 Feng contact model . . . 75
5.1.2 Linear Volume-Based (LVB) contact model . . . 76
5.2 Methodology: Spherical granule indentations . . . 77
5.3 Indentation tests & discussion . . . 78
5.3.1 Feng model evaluation . . . 78
5.3.2 LVB model evaluation . . . 81
5.3.2.1 LVB vs. Linear CM . . . 85
5.4 Summary . . . 88

6 Influence of the Poisson effect **89**
6.1 Verification by uniaxial compression . . . 90
6.2 Isotropic compression and data analysis . . . 93
6.3 Results and discussion . . . 94
6.4 Conclusions . . . 96

7 Conclusions **97**
7.1 Conclusions . . . 97
7.2 Recommendations & further research . . . 98

Nomenclature **102**

Reference List **103**

A Kumar **113**

B Abaqus Options **117**
B.1 Step properties . . . 117
B.2 Interaction properties . . . 117
B.3 Overview of models . . . 117
B.3.1 Uniaxial compressions . . . 117
B.3.2 Kinematic collisions . . . 118
B.3.3 Indentations . . . 118
B.3.4 Isotropic compressions . . . 119

C Multi-Sphere DEM errors: additional figures **121**

D Smooth Cone contact **123**
D.1 Smooth cone measurements 123
D.1.1 Spherical overlap 123
D.1.2 Overlap beyond spherical tip of cone 125

List of Figures

1.1 DEM-related article evolution. Taken from European Cooperation in Science and Technology (2023). 1

2.1 Flowchart of DEM algorithm, adapted from O'Sullivan (2011a). The 'Force calculation at contact points' stage is the main focus of the thesis. 7
2.2 Examples of 3D superquadrics, reproduced from Lu *et al.* (2015). The blockiness parameters range from 0.2 to 10, with ε_1 increasing from left to right and ε_2 increasing from top to bottom. 9
2.3 A spherocylinder formed using a cylinder and two hemi-spheres, reproduced from Kodam *et al.* (2010). 9
2.4 Examples of polyhedra used in DEM, reproduced from Park *et al.* (2021). . . . 10
2.5 Spherical harmonics method for particle shape representation in DEM simulations, reproduced from Capozza & Hanley (2021). Particle representations with maximum degrees $N = 0$, 8, 20 and 100 are shown. 10
2.6 Multi-Spherical clumps representing various shaped granules, reproduced from Haeri (2017). The constituent spheres in the MS granules are colour coded according to their respective size. 11
2.7 Level set function illustrated in 2D, adapted from Kawamoto *et al.* (2016). (a) Original granule surface. (b) Contour lines representing the signed distance from the granule surface. (c) Superimposition on grid. (d) Discretized level set function. (e) Level set function with interpolation between grid points. (f) Reconstruction of original grain surface via interpolation. 12
2.8 Potential particles representation, adapted from Boon *et al.* (2013). The mesh represents the particle surface and the different contours indicate the space inside or outside the particle. 12
2.9 Typical DEM contact between two spheres of radius R. The normal contact force is typically related to the contact overlap δ. The spherical contact radius is denoted by a. 13

2.10 Schematic comparing particle–particle contact with particle–wall contact highlighting the perceived difference in deformations δ taking place. 15

2.11 Contact between two bodies/ellipsoids with principal axes x_1, y_1, z for Body 1 and x_2, y_2, z for Body 2. The elliptical contact area is shown on the right, also indicating the angle ω between the principal axes. Figure reproduced from Kumar *et al.* (2018). 18

2.12 Schematic of a spherocylinder showing the transition regions between a circular contact area and an elliptical contact area. The length of the buffer region is defined by l_t. Figure reproduced from Kumar *et al.* (2018). 20

3.1 Schematic showing a single sphere with radius R before and after uniaxial compression between two rigid plates, with F being the normal force applied on the granule by the rigid plates and δ being the deformation of the sphere at each point of contact. 26

3.2 Schematic indicating how strain is applied on a spherical granule during quasi-static compressions (left) and kinematic collisions (right). The average strain applied in both cases is 5%, but it is distributed differently due to the nature of each contact. 26

3.3 Octant of the sphere simulated in Abaqus FEA at an average strain of 5%. The contours represent the y-axis displacement (perpendicular to the plate) measured in mm. 27

3.4 Comparison between Rathbone results (includes plasticity), Hertz and the FEA up to 0.05% strain. In this case, the material's Poisson's ratio $\nu = 0$. 28

3.5 Comparison between FEA, Hertz and Tatara contact models when a sphere is compressed by two rigid plates until a strain of 2.5% is applied per contact. The comparison is performed for Poisson's ratios of $\nu = 0$ and $\nu = 0.3$, shown in blue and red respectively. 29

3.6 Kinematic collision Force–Strain curve obtained from a parametric study. The force response obtained from the uniaxial compressions is also included, as well as the force responses predicted from Hertz and Tatara's models. 31

3.7 Spherical granule cross-section view (for uniaxial compressions). The shaded areas indicate the designated PoC regions, where the mesh is more refined. 32

3.8 The residuals of the forces obtained at maximum strain in the uniaxial compressions of a sphere were plotted against the Degrees of Freedom. The negative signs represent an underprediction of the forces obtained. 33

3.9 The residuals of the forces obtained at maximum strain in the kinematic collisions of a sphere on a flat plate were plotted against the Degrees of Freedom. The negative signs represent an underprediction of the forces obtained. 34

4.1 Examples of the multi-spherical approach used to represent ellipsoids with various aspect ratios s and number of constituent spheres N: (a) $s = 1.5$, $N = 3$, (b) $s = 1.5$, $N = 7$, (c) $s = 1.5$, $N = 13$, (d) $s = 2.35$, $N = 5$, (e) $s = 2.35$, $N = 9$, (f) $s = 2.35$, $N = 17$, (g) $s = 5.0$, $N = 11$, (h) $s = 5.0$, $N = 17$, (i) $s = 5.0$, $N = 33$, (j) $s = 10$, $N = 23$, (k) $s = 10$, $N = 37$, (l) $s = 10$, $N = 55$. Image reproduced from Markauskas *et al.* (2010). 38

4.2 Examples of the multi-spherical approach used to represent different multi-sphere approximations of an aluminium oxide particle using 7, 12, 17, 22, 135, 190, 245 and 300 spheres respectively. Image reproduced from Kruggel-Emden *et al.* (2008). 38

4.3 Schematic showing the errors present in multi-spherical DEM and the methods used to quantify them. 39

4.4 Schematic demonstrating how the kinematic collision simulations were set up on Abaqus. The top view is on the left of the figure while the side view is on the right. The angle changing in the different cases is the designated angle θ in the schematic. 40

4.5 Metrics comparison for defining the simulation endpoint used for the kinematic collisions in Abaqus. The moments where each candidate endpoint is reached for the different variables tested are noted with a dotted line. The case shown is that of perfect spherocylinders coming into contact at a 90° angle. 41

4.6 Schematic representation of various two-sphere rod configurations based on spatial location within the contour plot. The configurations shown have 5 %, 50 % and 80 % sphere overlaps throughout the different stages of compression. Deformations have been exaggerated to enhance clarity of representation. 44

4.7 Comparison of the force response of a two-sphere rod at various sphere overlaps obtained through the FEA against the one obtained through (a) the Hertzian contact model and (b) Tatara's contact model. The contours are indicating the relative errors present, while the signs of the errors represent whether the contact models are overpredicting (positive error) or underpredicting (negative error) the contact force based on the FEA results. 45

4.8 Comparison of the force response of a three-sphere rod at various sphere overlaps obtained through the FEA against the one obtained through (a) the Hertzian contact model and (b) Tatara's contact model. The contours are indicating the relative errors present, while the signs of the errors represent whether the contact models are overpredicting (positive error) or underpredicting (negative error) the contact force based on the FEA results. 48

4.9 Contour plots showing the error bounds between the force responses of the MS rods in the FEA and the Hertzian contact model at the various angles. The positive errors in red indicate the configurations where the contact model overestimates the force response and the negative errors in blue indicate an underestimation of the force response when compared to that of the Finite Element model. 51

4.10 Schematic of contact areas (highlighted in red) of multi-spherical rods and spherocylinders in contact as seen from above. 52

4.11 Contour plots showing the error bounds between the force responses of the MS rods in the FEA and Tatara's contact model at the various angles. The positive errors in red indicate the configurations where the contact model overestimates the force response and the negative errors in blue indicate an underestimation of the force response when compared to that of the Finite Element model. 54

4.12 Comparison of the force response during parallel contact of a three-sphere rod at various sphere overlaps obtained through the FEA against the one obtained through the Linear contact model. The contours are indicating the relative errors present, while the signs of the errors represent whether the contact model is overpredicting (positive error) or underpredicting (negative error) the contact force based on the FEA results. 57

4.13 Contour plots showing the error bounds between the force responses of the MS rods in the FEA and the Linear contact model at the various angles. The positive errors in red indicate the configurations where the contact model overestimates the force response and the negative errors in blue indicate an underestimation of the force response when compared to that of the Finite Element model. 59

4.14 Aspherix Advanced Multi-Sphere Method comparison with FEM and Hertz in parallel and perpendicular three-sphere rod contacts. 62

4.15 (a) Original and (b) Expanded Point of Contact regions used to confirm that the side contact forces were captured properly in an angled collision. The original PoC region has a radius of $0.3R$ and the expanded PoC region has a radius of $0.7R$, where R is the rod radius. The side contacts of concern can be seen in the schematic in Figure 4.10. 63

4.16 Comparison of the force–strain curves of two identical collision configurations, testing the impact of an expanded PoC region in the mesh. The force–strain curve of the model using the original PoC region is plotted in orange, while the one with the expanded PoC region is plotted in blue. Collision configuration: three-sphere rods, 30° angle, 20% sphere overlap, 5% strain. 63

4.17 Schematic representation of the shape approximation error when modelling a perfect spherocylinder using the Multi-Sphere method. 64

4.18 Comparison of two methods of MS rod characterisation: volume fraction occupied by the MS rod compared to the perfect spherocylinder and the overlap fraction of the constituent spheres in the MS rod. 66
4.19 Contour plot showing the error bounds between the force responses of the MS rods and the perfect spherocylinder. The negative errors in blue indicate the configurations where the MS rods underestimate the force response when compared to that of the perfect spherocylinder. Since the responses of the MS rods are compared against that of the perfect spherocylinder, all the errors are negative. . 70
4.20 Force responses of rods at 2.5% strain at a parallel contact against the number of constituent spheres. 71
4.21 Comparison between MS rod and perfect spherocylinder force responses at a parallel contact up to 2.5% strain. 72

5.1 The model detects two contact points at the vertices of the polygonal granule, but the force is calculated at the point with the largest overlap in (a). The particle then rotates and the position of the force vector "jumps" to the other contact point in (b). Schematic adapted from Fraige *et al.* (2008). 76
5.2 With enough rotational energy, an elongated particle can suddenly reach a position where its elongated part completely overlaps with a wall (or another particle) during contact. This can cause a massive spike in the contact force calculation due to the large distance overlap increase. 76
5.3 Indenters used for the indentation tests. The apex of the conical indenter and the edges of the cylindrical indenter were rounded to a spherical surface with radius 0.005 mm. 77
5.4 Axisymmetric model example used for the indentation tests. There is a symmetry plane at the bottom boundary while the left boundary is defined as the axis of axisymmetry for the spherical granule. 78
5.5 Conical indentation force responses. Feng's fitted parameters are given in Table 5.1. 80
5.6 Stress distributions at the surface of a spherical granule and along the axis of symmetry caused by a uniform pressure (left) and a Hertzian pressure (right) acting on a circular area with radius a. Taken from Johnson (1985, p. 94). 81
5.7 Indenter force responses of two different materials plotted against the volumetric deformation obtained from FEM. 82
5.8 Conical indentation force responses plotted against the analytical contact volume overlap rather than the volumetric deformation obtained from FEA. 83
5.9 The analytical contact volume overlap was plotted against the volumetric deformation obtained from FEA. The dotted line represents the $y = x$ line along which ideally all curves would lie. 84

5.10 Conical indentation force responses. Comparison between LVB and the Conventional Linear CM. The y-axis of the 15° conical indenter plot was coloured red to highlight the different scale used. The relative k values are shown in Table 5.2. . 86
5.11 Uniaxial compressions of a sphere force responses. 87
5.12 Percentage errors obtained from the contact models evaluated against the FEA. The positive errors represent an overprediction of the force response while the negative errors represent an underprediction when compared with the FEA results. 88

6.1 Schematic showing a single sphere before (left) and after (right) uniaxial compression between rigid plates. The lateral extension at the central diameter of the sphere is represented by $U(R)$. Deformations have been exaggerated to enhance clarity of representation. 90
6.2 The octant of the sphere simulated in Abaqus FEA at a total compressive strain of 5%. The contours represent the von Mises stress measured in Pa. 91
6.3 Relationships between (a) contact force, F, and total compressive strain on granule and (b) lateral extension at the central diameter of the sphere, $U(R)$, and total compressive strain on granule for a single sphere subjected to uniaxial compression in FEM, compared with analytical curves of Hertz (1882) and Tatara (1991). . . 92
6.4 Octant of spherical granule being isotropically compressed. The contours represent the von Mises stress measured in Pa when the maximum confining stress is applied. 93
6.5 Elastic bulk modulus, K_0, against effective confining stress, σ', at six Poisson's ratios, ν. The FEM data is shown using black markers; results for a Hertzian sphere are shown as grey dashed lines. The slopes of the best-fit linear regressions to the FEM data, n, are provided in the legend. 94
6.6 The elastic bulk modulus, K_0, against the effective confining stresses, σ', at Poisson's ratios, ν, of 0.01, 0.1, 0.2, 0.3, 0.4 and 0.49 for effective confining stresses of 50 MPa–200 MPa. Black dotted linear regressions are shown for the FEM data (black markers). As for Figure 6.5, results for a Hertzian sphere are shown as grey dashed lines 95

A.1 Force responses of spherocylinder collisions at various angles. Comparison between the FEA results and the contact model by Kumar *et al.* (2018). 115

C.1 Force–strain plots shown of the parametric study performed in order to obtain the force response of perfect spherocylinders colliding at a 90° angle. The endpoints of each simulation which contribute to the final force response of the specific contact scenario are also shown. 121
C.2 Example of curve fitting performed for the Fixed-Length Rod collisions at 90° for more accurate comparison of the force response of the perfect spherocylinder and the FLRs 122

C.3 Fixed-Length Rod parallel contact contour plot displaying the location of all datapoints where errors were calculated. 122

D.1 Contact between a spherical granule and a smoothed cone from a DEM perspective. In (a) the overlap is limited to the spherical tip of the cone, whereas in (b) the conical body also overlaps with the granule. 124

List of Tables

2.1 Contact area scenarios in spherocylinder–spherocylinder contact or spherocylinder–wall contact. Figure reproduced from Kumar *et al.* (2018). 19
2.2 Contact model and shape usage in DEM literature. 24

3.1 Material properties used for both the quasi-static compression and kinematic collision simulations. 25
3.2 The element sizes at the Point of Contact (PoC) are displayed next to the total Degrees of Freedom (DoF) of the model for the uniaxial compressions of a sphere. The final mesh size selected for the quasi-static compressions is the one depicted in the 4^{th} row of the table. 33
3.3 The element sizes at the Point of Contact (PoC) is displayed next to the total Degrees of Freedom (DoF) of the model for the kinematic collisions of a sphere on a flat plate. The final mesh size selected for the kinematic collisions is the one depicted in the 3^{rd} row of the table. 34

4.1 Three-Sphere Rod configurations 43
4.2 Fixed-Length Rod configurations 65
4.3 Fixed-Length Rod configurations simulated with their respective sphere overlap percentages as well as the occupied volume fraction with respect to the PSC. The additional rod configurations used for the parallel contact are also displayed in the bottom section of the table. 67

5.1 Feng parameters m and k obtained after fitting as shown in Figure 5.5. 79
5.2 k values used for the Conventional Linear CM and LVB for each material in the conical indentations. The k values for both models were calibrated with the force obtained at 1.5% with the 30° conical indenter. 85

Chapter 1

Introduction

Computational modelling of granular systems has increased significantly in recent years, particularly using the Discrete-Element Method (DEM), a simulation tool originally developed by Cundall & Strack (1979). The Discrete-Element Method is becoming widely used for granular simulations both in industry and in academia. In Figure 1.1 it is shown how the number of DEM-related articles has grown exponentially since its conception. One of the main advantages of DEM is that it can provide information on the micromechanical behaviour of individual particles, which can be used to explore the relationship between macro- and microscopic properties in granular materials.

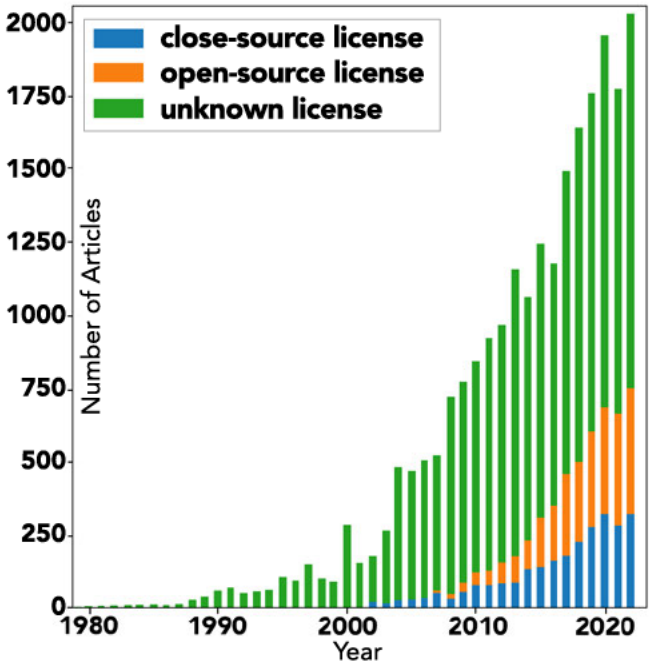

Figure 1.1: DEM-related article evolution. Taken from European Cooperation in Science and Technology (2023).

These individual particles in DEM are generally modelled as spheres due to their computational simplicity. However, particle shape is an important factor that significantly impacts the bulk behaviour of particulate systems, thus causing a major increase in scientific interest in DEM modelling of non-spherical particle systems. One popular way of representing non-spherical granules in DEM simulations is using multi-spherical clusters. A cylindrical granule for instance can be emulated by fixing together a number of collinear spheres. The constituent spheres may be overlapping or even have different diameters, thus permitting virtually any shape to be reproduced.

In the 'soft-particle' DEM approach, a contact model is needed to relate finite interparticle overlaps to the force. Regardless of particle shape, these contact models are usually based on Hooke's law, i.e., the normal component of contact force is proportional to the overlap, or Hertzian mechanics. Although sophisticated contact models have been developed recently for non-spherical particle simulations, the overwhelming majority of non-spherical simulations still use Hooke or Hertz. Very limited research has been done however that quantifies how large the errors are for adopting these models in non-spherical DEM simulations. This is the knowledge gap that is addressed in Chapter 4.

Furthermore, the majority of contact models (e.g. Hooke, Hertz) relate the force to the interparticle *distance* overlap during collisions, mainly due to its comparative simplicity to be obtained. A viable alternative that has not been extensively researched is relating the force to the contact volume overlap instead, which is further explored in Chapter 5.

1.1 Scope

The focal point of this thesis is on contact models for the normal contact forces of fully elastic contacts. A contact is considered elastic when the deformation upon contact is reversible and independent of the rate at which the deformation develops. All the factors listed below are outside the scope of this thesis:

- Contact models for the tangential components of contact forces
- Plasticity
- Viscoelasticity/damping
- Friction
- Adhesion/cohesion
- Particle fragmentation
- specific algorithms for contact evaluation or detection

Related to the last point, one of the assumptions being made is that the relevant quantities for computing the contact forces are available: deformations, overlap volume, contact surface area; how any of these might be computed within a DEM code is not considered in this thesis. Additionally, for all non-spherical granules implementing the multi-spherical approach in this work, the Multi-Spherical (MS) clumps taken into consideration are rigid and not bonded.

1.2 Thesis outline

This thesis is divided into 7 chapters. Following this brief introduction in Chapter 1, Chapter 2 contains the literature review which explores different ways non-spherical particles can be represented in DEM simulations as well as various contact models that are currently being used. Chapter 3 presents the main Finite Element Modelling methodology used throughout the thesis as well as its verification and a mesh dependence study. In Chapter 4 the errors present when the Multi-Spherical approach is used to represent non-spherical particles are identified and quantified for the exemplar shape of spherocylinders. In Chapter 5 two volume-based contact models are evaluated and their applicability in DEM is discussed. In Chapter 6 the influence of the Poisson effect on the stress dependence of the elastic moduli of soil was examined. Finally, Chapter 7 contains the overall conclusions and recommendations for future work.

Chapter 2

Literature review

Understanding the effects of particle movement is vital for a wide range of applications and research areas. It enables precise manipulation, transport, and dispersion of particles, provides insights into material behaviour, and helps optimise processes involving particles. By studying particle movement, researchers can gain valuable insights into the dynamics and interactions of particles, leading to advancements in various fields of science and engineering.

2.1 Discrete-Element Method (DEM)

The Discrete-Element Method (DEM) is a numerical technique used to simulate the behaviour of granular materials, particles, and discontinuous systems. Proposed by Cundall & Strack (1979), it has gained significant importance in various fields due to its ability to capture the complex interactions and behaviour of discrete elements (O'Sullivan, 2011a).

DEM has been widely applied in geotechnical engineering, powder technology, and rock mechanics. In geotechnical engineering, DEM allows for the analysis of soil behaviour, slope stability, and the response of granular materials under different loading conditions (Yimsiri & Soga, 2000; Cheng *et al.*, 2003; O'Sullivan, 2011b; Zheng *et al.*, 2021). In powder technology, DEM is used to study particle flow, mixing, segregation, and the behaviour of granular materials in industrial processes (Cleary, 2004; Govender *et al.*, 2018; Tang *et al.*, 2020). In rock mechanics, DEM enables the analysis of rock fragmentation, rock cutting, and the behaviour of discontinuous rock masses (Rojek *et al.*, 2011; Knowles *et al.*, 2021).

One of the key advantages of DEM is its ability to model the behaviour of individual particles and their interactions. It provides insights into the microscale behaviour of granular materials, allowing for a better understanding of phenomena such as particle rearrangement, compaction, and failure (Shire *et al.*, 2016; Giannis *et al.*, 2021; Chen *et al.*, 2022). DEM also offers the advantage of being able to simulate systems with irregular particle shapes, providing a more realistic representation of real-world scenarios (Cleary & Sawley, 2002). This aspect is discussed in detail in Section 2.2.

Another important aspect of DEM is its ability to capture the collective behaviour of particles, such as the formation of particle clusters, arching, and the emergence of macroscopic properties (Yang *et al.*, 2015; Sassel *et al.*, 2023). By simulating the interactions between individual particles, DEM can provide valuable information on the bulk behaviour of granular materials, such as flow patterns, packing density, and stress distribution (Feng *et al.*, 2009; Zhao *et al.*, 2017).

DEM has also been combined with other numerical methods, such as the Finite Element Method (FEM) and Computational Fluid Dynamics (CFD), to study coupled phenomena. This allows for the simulation of complex multiphysics problems, such as fluid–particle interactions, particle–fluid flow, and the behaviour of granular materials in fluidized beds or mixing processes (Kloss *et al.*, 2012; Zhong *et al.*, 2016; Yang *et al.*, 2020; Liu & Hanley, 2023).

2.1.1 DEM Theory

The general DEM solver algorithm (O'Sullivan, 2011a) is shown in Figure 2.1 indicating the different stages taking place during each timestep Δt in a DEM simulation. At each individual timestep all the contacts between particles or between particles and non-particle elements (e.g. walls) are detected and the forces are calculated. The acceleration is then obtained using Newton's 2^{nd} law of motion and subsequently the velocities and displacements of each particle are obtained by integration. Particle positions are finally updated for the next timestep and the process is repeated until the end of the simulation.

In the most common implementation of DEM, particles are modelled as rigid bodies, where the deformations at the contact points are captured by permitting overlaps between the interacting particles. Generally, $\textbf{Force} = \boldsymbol{f}\,\textbf{(Distance overlap)}$, so the contact forces applied on each particle can be calculated from those contact overlaps. Typically the greater the overlap between the particles in contact, the greater the contact force.

This relation between the contact forces and the overlaps is referred to as a contact model. It should be highlighted that there are separate contact models for the normal component and for the tangential component of the contact forces. The normal component encompasses the forces acting perpendicular to the contact surface between particles during contact, mainly influencing the deformation of the particles. As for the tangential component, it encompasses the forces acting parallel to the contact surface, representing the frictional behaviour and sliding motion between particles during contact. Different combinations of contact models can be used in a single DEM simulation, for example having different particle–particle forces to particle–wall forces, although this is beyond the scope of the thesis.

Both 2D and 3D scenarios can be simulated using DEM, however the focus of this thesis is on 3D DEM simulations. The particles in (3D) DEM simulations are generally modelled as spheres because of their computational simplicity; they can be fully defined just by using one dimension, their radius. However, in order to achieve quantitatively accurate results compared to a real, physical system, spherical particles are often an inadequate representation of real particles.

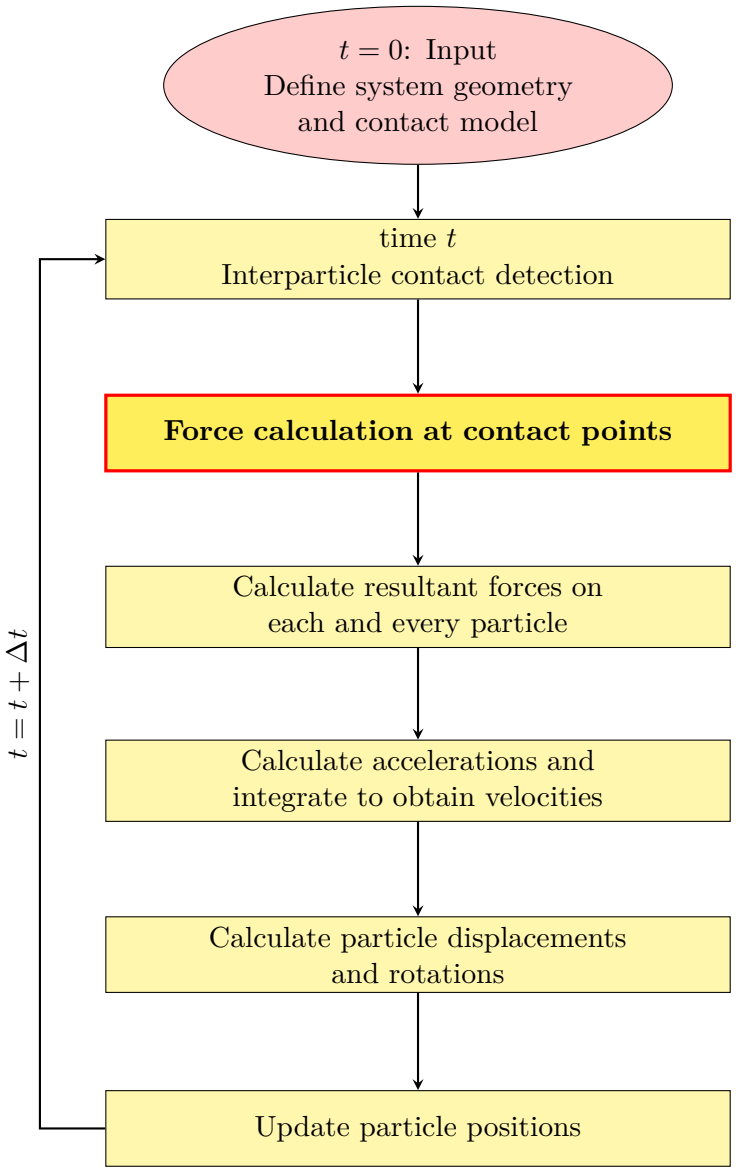

Figure 2.1: Flowchart of DEM algorithm, adapted from O'Sullivan (2011a). The 'Force calculation at contact points' stage is the main focus of the thesis.

2.2 Particle shapes in DEM

Particle shape is an important factor which also increases complexity. Real particles are non-spherical and shape has been shown to have an important effect on the bulk behaviour of particulate systems, thus causing a major increase in scientific interest in DEM modelling of non-spherical particle systems (Lu *et al.*, 2015; Zhong *et al.*, 2016; Nguyen & Plimpton, 2019). Additionally, the increase in the availability of computational resources in recent years further drives the demand for a solution. There are multiple ways to incorporate shape in DEM. A short overview of different methods used to represent different particle shapes follows. Contact detection in all the different ways particle shape is represented within DEM is beyond the scope of this thesis.

Rolling Friction The simplest option is to keep the spherical particles but apply rolling friction, which essentially adds some resistance to the rolling motion of the particles (Ai *et al.*, 2011; Wensrich & Katterfeld, 2012; Huang *et al.*, 2017). This is achieved by incorporating torque terms at the interparticle contacts. While it is relatively simple to include rolling friction, it requires calibration and on its own it does not accurately capture the motion of non-spherical particles since shape in a particle can also cause rotation rather than just oppose rolling motion. For example, a rod-shaped particle would be toppled over if placed upright but at an angle, with momentum generated due to its weight. The application of rolling friction though in a similar situation would resist that motion.

Non-spherical particles

Switching to non-spherical particles introduces the need to determine the particles' exact orientation. The particle orientation is necessary in order to obtain the rotational motion of the particles but also for accurate contact detection, which further complicates the situation.

2.2.1 Ellipsoids

The simplest non-spherical particles that can be used in a DEM simulation are ellipsoids (Lin & Ng, 1995). They are defined by Equation 2.1:

$$f(x,y,z) = \left(\frac{x}{a}\right)^2 + \left(\frac{y}{b}\right)^2 + \left(\frac{z}{c}\right)^2 - 1 \tag{2.1}$$

where the coordinates in the body-fixed coordinate system are depicted as x, y, z and a, b, c are the half lengths of the principal axes of the particle. In the special case when $a = b = c$, the resulting shape is a sphere where a, b, c can be replaced with the radius of the sphere R.

2.2.2 Superquadrics

Superquadrics are a generalized form of ellipsoids. Equation 2.2 (Barr, 1981) that defines them:

$$f(x,y,z) = \left[\left(\frac{x}{a}\right)^{2/\varepsilon_2} + \left(\frac{y}{b}\right)^{2/\varepsilon_2}\right]^{\varepsilon_2/\varepsilon_1} + \left(\frac{z}{c}\right)^{2/\varepsilon_1} - 1 \tag{2.2}$$

is similar to Equation 2.1 but introduces additional parameters ε_1 and ε_2 which control the blockiness of the particle while still maintaining their symmetry. This is further illustrated in Figure 2.2. In the special case when $\varepsilon_1 = \varepsilon_2 = 1$, the resulting shape is an ellipsoid.

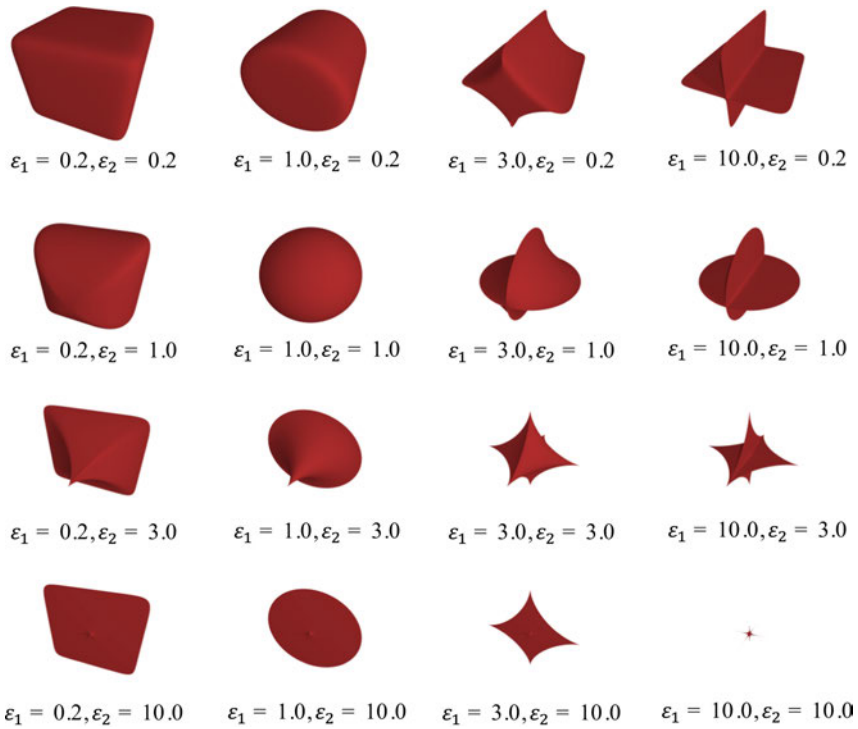

Figure 2.2: Examples of 3D superquadrics, reproduced from Lu *et al.* (2015). The blockiness parameters range from 0.2 to 10, with ε_1 increasing from left to right and ε_2 increasing from top to bottom.

2.2.3 Spherocylinders

Spherocylindrical particles can also be used in DEM simulations (Kodam *et al.*, 2010). They are represented by attaching hemi-spheres to both ends of a cylinder. The same radius is used for the cylinder and hemi-spheres in order to ensure a smooth continuous transition between the different parts, therefore creating a uniform granule as shown in Figure 2.3.

Figure 2.3: A spherocylinder formed using a cylinder and two hemi-spheres, reproduced from Kodam *et al.* (2010).

2.2.4 Polyhedra

Moving away from continuous particle surfaces, polyhedra can also be used in DEM simulations (Hart *et al.*, 1988; Ghaboussi & Barbosa, 1990) to model particles with sharp edges and flat surfaces as shown in Figure 2.4. They can also introduce an element of asymmetry which is not possible with the aforementioned methods.

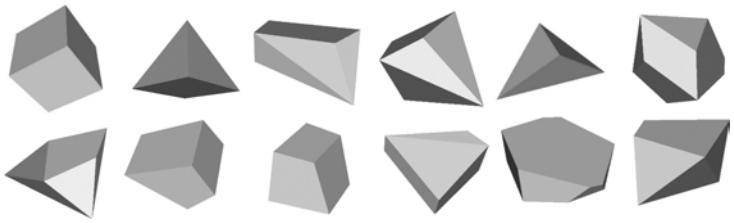

Figure 2.4: Examples of polyhedra used in DEM, reproduced from Park *et al.* (2021).

2.2.5 Spherical Harmonics

The spherical harmonic approach offers a hierarchical representation of particle shape, allowing for different levels of detail to be captured. This hierarchical nature enables the method to efficiently describe the intricate features of irregularly shaped particles while maintaining computational efficiency (Wang *et al.*, 2021; Capozza & Hanley, 2021). An example of the detail that can be captured using this method is shown in Figure 2.5 where N is the maximum degree at which the spherical harmonic expansion is truncated. The greater N is, the higher the level of that accuracy can be obtained.

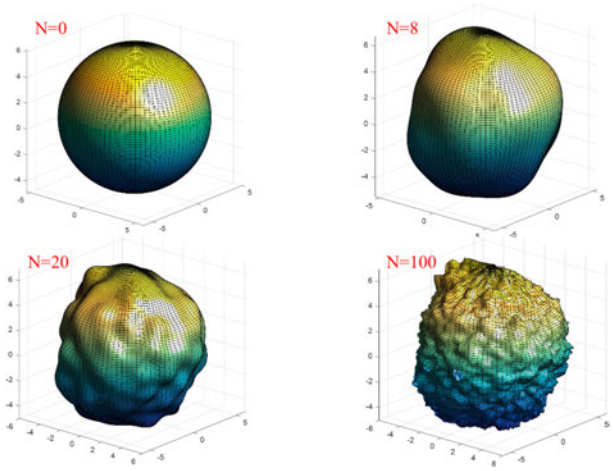

Figure 2.5: Spherical harmonics method for particle shape representation in DEM simulations, reproduced from Capozza & Hanley (2021). Particle representations with maximum degrees $N = 0,\ 8,\ 20$ and 100 are shown.

2.2.6 Multi-Spherical clumps

One of the most common methods of emulating non-spherical particles is the Multi-Spherical (MS) approach (Favier *et al.*, 1999; Lu *et al.*, 2015; Marigo & Stitt, 2015; Zhong *et al.*, 2016; Haeri, 2017), where a number of spheres are 'glued' together in a cluster in order to construct a more complex shaped granule as shown in Figure 2.6. The spheres may be overlapping and can also have different dimensions allowing for a very accurate representation of a wide variety of shapes.

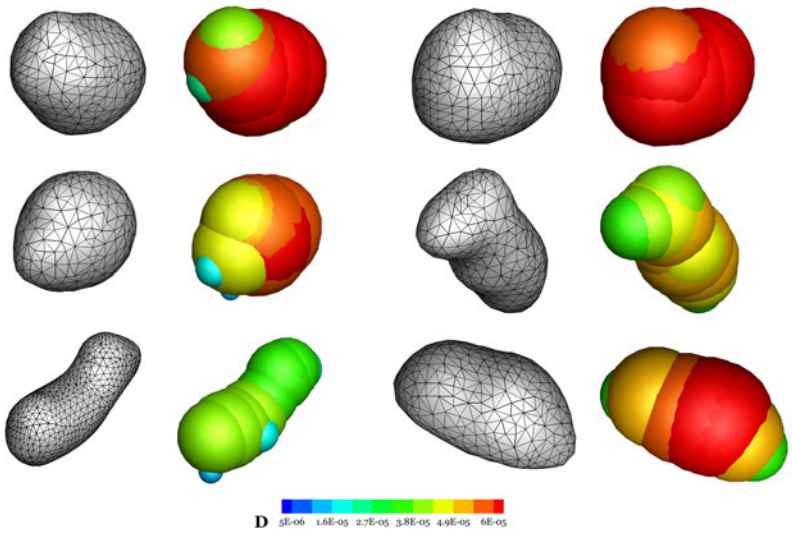

Figure 2.6: Multi-Spherical clumps representing various shaped granules, reproduced from Haeri (2017). The constituent spheres in the MS granules are colour coded according to their respective size.

A great advantage is that, since the granules are composed of spheres, the already established contact detection algorithms can be directly applied. The downside is that, depending on the accuracy needed for the shape representation, a large number of constituent spheres has to be used. This in turn affects the particle mass and moment of inertia calculations when spheres overlap as the excess mass of the overlapping regions within a granule need to be considered.

Additionally, the gaps between the constituent spheres also have a great impact on how the granules behave during contact. Depending on the point of contact (single, double, triple contact, etc...) during a collision, the macroscopic roughness induced from the interspherical gaps can affect the particle trajectories as well as other macroscopic collision properties (Kruggel-Emden *et al.*, 2008). Some of them include the rotational speed of the granule, its rebound angle, the collision time and coefficient of normal restitution. Nonetheless, the MS approach is already widely used in most DEM packages including EDEM (DEM Solutions Ltd., 2019) and LIGGGHTS (Kloss *et al.*, 2012).

In addition to the 'glued' together approach, the spheres in a MS cluster may also be bonded to one another. Different properties can be assigned on those bonds defining their strength. This

method can be used to simulate fragmentation scenarios of agglomerates in DEM (Cheng *et al.*, 2003), although particle crushing is beyond the scope of this thesis.

2.2.7 Level sets

In the level set method, a level set function is employed to represent the boundaries of particles or interfaces within the system (Kawamoto *et al.*, 2016; Davis *et al.*, 2021). This function is defined as a signed distance function, which assigns positive or negative values to points inside or outside the particle boundary, respectively. The simulation of particle motion, contact and deformation is then enabled by tracking the evolution of the level set function on the global grid. A 2D illustration of the level set function is shown in Figure 2.7.

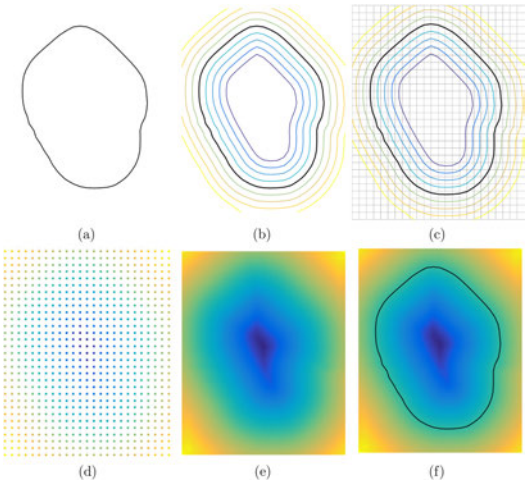

Figure 2.7: Level set function illustrated in 2D, adapted from Kawamoto *et al.* (2016). (a) Original granule surface. (b) Contour lines representing the signed distance from the granule surface. (c) Superimposition on grid. (d) Discretized level set function. (e) Level set function with interpolation between grid points. (f) Reconstruction of original grain surface via interpolation.

2.2.8 Potential Particles

With the potential particles approach, the particles are defined in terms of some function of a local coordinate system $f(x, y, z) = 0$, where x, y, z are the granules' local coordinates (Houlsby, 2009; Boon *et al.*, 2013). The function is defined in such a way that $f = 0$ defines the particle surface, $f < 0$ indicates the space inside the particle and $f > 0$ indicates the space outside the particle. This is shown in Figure 2.8 for a 3D potential particle.

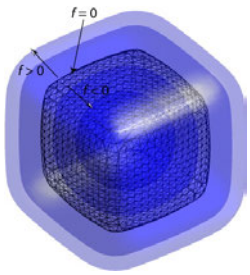

Figure 2.8: Potential particles representation, adapted from Boon *et al.* (2013). The mesh represents the particle surface and the different contours indicate the space inside or outside the particle.

Two-dimensional DEM shapes

All of the aforementioned shape representation methods have equivalents for 2D DEM simulations. Using circles instead of spheres, ellipses instead of ellipsoids, superellipses instead of superquadrics, polygons instead of polyhedra, circular harmonics instead of spherical harmonics and multi-disk clumps instead of multi-spherical clumps. The remaining methods — rolling friction, level sets and potential particles — can be directly applied in 2D DEM simulations.

2.3 Contact Models commonly used in DEM

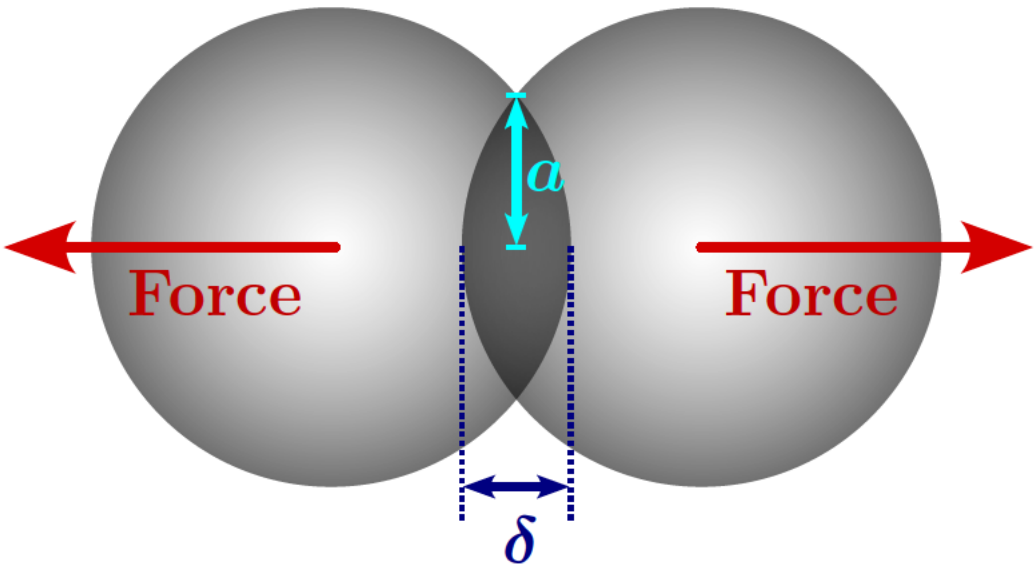

Figure 2.9: Typical DEM contact between two spheres of radius R. The normal contact force is typically related to the contact overlap δ. The spherical contact radius is denoted by a.

2.3.1 Hertz contact model for spheres

The main assumptions made for the Hertzian contact model (Hertz *et al.*, 1896; Johnson, 1985; Dintwa *et al.*, 2008; O'Sullivan, 2011b) are listed below:

- The contacting bodies are isotropic and homogeneous.
- The contact area is small relative to the bodies' dimensions, which can be considered as elastic half-spaces.
- The surfaces are smooth and frictionless, with no asperities, continuous and non-conforming.
- The induced strains are sufficiently small so the material response remains linearly elastic (constant Young's modulus).
- There is no interaction outside the loaded area such as adhesion or tensile forces.

- As long as the stiffnesses of the two contacting bodies are equal, friction is not brought into play as there is no relative tangential straining along the contact surface.

According to Hertzian theory, the normal contact force, F, is given by Equations 2.3–2.5:

$$F_{\text{Hertz}} = \frac{4}{3} E^* \sqrt{R^*} \delta^{3/2} \tag{2.3}$$

$$\frac{1}{E^*} = \frac{1-\nu_i^2}{E_i} + \frac{1-\nu_j^2}{E_j} \tag{2.4}$$

$$\frac{1}{R^*} = \frac{1}{R_i} + \frac{1}{R_j} \tag{2.5}$$

where δ is the deformation of the sphere (analogous to contact overlap in a DEM simulation of Hertzian spheres) and R^* is the effective radius of the contact, with R_i and R_j being the radii of the two particles in contact. The effective elasticity E^* depends on the individual Young's moduli of the two particles in contact, E_i and E_j, as well as their respective Poisson's ratios ν_i and ν_j. There are two types of contacts which result in slightly different formulations of the contact model: particle–particle contacts and particle–wall contacts.

Particle–Wall contact The particle–wall version of the contact model can still be derived from the same set of equations (2.3–2.5) with the main difference being that $E_{\text{wall}} \to \infty$ (for a rigid wall) and $R_{\text{wall}} \to \infty$. When these are substituted in Equations 2.4 and 2.5 respectively they result in:

$$E^* = \frac{E}{1-\nu^2} \qquad \text{and} \qquad R^* = R$$

where E, ν and R are the particle material properties. Therefore, for a sphere contacting a rigid wall/plate, the normal contact force F is simplified to:

$$F_{\text{Hertz}} = \frac{4}{3} \frac{E\sqrt{R}}{(1-\nu^2)} \delta_{\text{wall}}^{3/2} \tag{2.6}$$

where δ_{wall} is the deformation of the particle in the particle–wall contact.

Particle–Particle contact For the particle–particle contact, focusing on the special case when all particles have the same radius R, the effective elasticity and effective radius obtained are:

$$E^* = \frac{E}{2(1-\nu^2)} \qquad \text{and} \qquad R^* = \frac{R}{2}$$

Thus, for two particles coming into contact, the normal contact force F_{Hertz} is simplified to:

$$F_{\text{Hertz}} = \frac{\sqrt{2}}{3} \frac{E\sqrt{R}}{(1-\nu^2)} \delta_{\text{pp}}^{3/2} \tag{2.7}$$

where δ_{pp} is the deformation of the particle in the particle–particle contact.

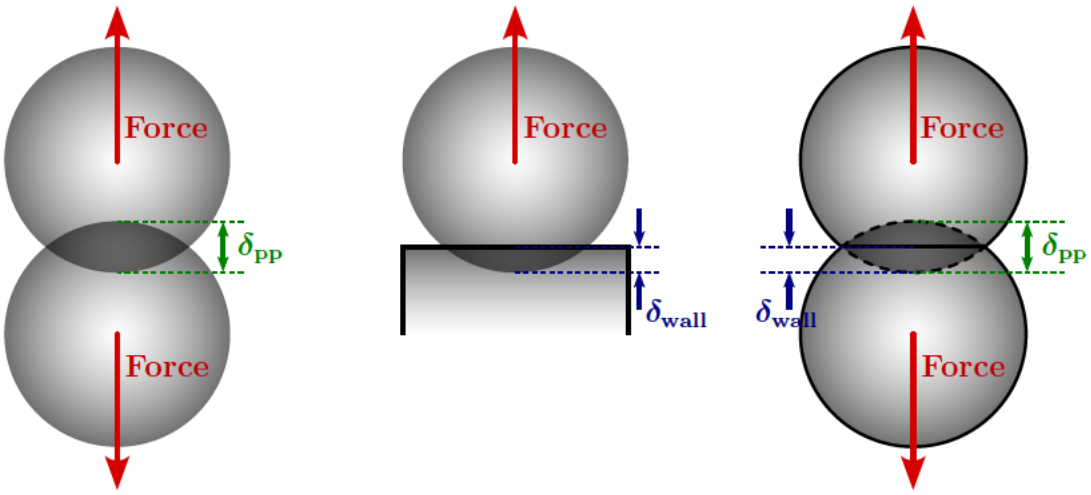

Figure 2.10: Schematic comparing particle–particle contact with particle–wall contact highlighting the perceived difference in deformations δ taking place.

While these two cases seem different at a first glance, when the contacting particles have the same radius and material properties, it can be seen from Figure 2.10 that $\delta_{pp} = 2\delta_{wall}$. Substituting δ_{pp} in Equation 2.7 results in Equation 2.6:

$$F_{\text{Hertz}} = \frac{\sqrt{2}}{3}\frac{E\sqrt{R}}{(1-\nu^2)}\left(2\delta_{\text{wall}}\right)^{3/2} = \frac{4}{3}\frac{E\sqrt{R}}{(1-\nu^2)}\delta_{\text{wall}}^{3/2}$$

2.3.2 Linear Contact Model

The Linear contact model is the simplest contact model (Thornton *et al.*, 2011) as the contact is described as a linear spring and is given by:

$$F = k\delta \tag{2.8}$$

The constant k is arbitrarily selected, usually so that the resulting force F matches a given force — obtained perhaps from experimental results — at a specific deformation δ. While that essentially means that it only produces an accurate force at the deformation where it was calibrated, it is extremely easy to apply even for non-spherical particle contacts making it widely used.

2.4 Other Contact Models

2.4.1 Tatara contact model: spheres under large deformations

Tatara (1991), recognising the limitations of the Hertzian contact model, expanded the model to account for large strains. Tatara's contact model is primarily based on the Hertzian theory. The

main difference is that some assumptions are effectively relaxed in order to develop the model. Those two main assumptions being relaxed are the constant Young's modulus (even though that was still the case in this work) as well as the infinitesimal deformations. The model was validated by uniaxially compressing spheres at extreme strains (Tatara *et al.*, 1991) and reached good agreements for up to 60% strains (Strain = $\frac{\delta}{2R}$) applied. Tatara went even further by taking into account the non-linear elasticity of rubber in compression, and added an extension to Hertz by considering the difference in vertical displacement corresponding to an applied load, compared to Hertz, arising from the reaction force generated within the depth of the compressed sphere (Tatara, 1989). Both factors within the contact model (extensive term and non-linear elasticity) can independently be considered or not, on one hand raising the complexity but on the other hand allowing the model to reach a better agreement at higher strains applied on the rubber spheres accordingly.

For application within this thesis, the extensive term was considered with a constant Young's modulus/linear elasticity. For the strains examined in this thesis ($\frac{\delta}{2R} \leq 5\%$), the simplified version that assumes linear elasticity is appropriate since the Finite Element Method (FEM) contact laws used for the analysis performed also assume that.

Therefore, the relationship between the normal contact force F and deformation δ is given by the Equations (2.9)–(2.11):

$$\delta = \frac{F}{E}\left[\frac{3\left(1-\nu^2\right)}{4a} - \frac{c}{\pi}\right] \tag{2.9}$$

$$a^3 = \frac{3\left(1-\nu^2\right)RF}{4E} \tag{2.10}$$

$$c = \frac{2(1+\nu)R^2}{\left(a^2+4R^2\right)^{\frac{3}{2}}} + \frac{1-\nu^2}{\sqrt{a^2+4R^2}} \tag{2.11}$$

where a is the radius of the circular contact area. While Tatara's contact model is more accurate than Hertz for larger deformations, the fact that the equations have to be solved iteratively in order to obtain the contact force from the deformation impedes its use in DEM simulations, as that greatly increases the computational time. Furthermore, since in conventional DEM simulations point contacts are assumed, contacts have to remain small so a contact model designed for extreme deformations should not become necessary.

In addition, Tatara presents equations for computing the lateral expansion of the spherical granules corresponding to an applied load which are used in Chapter 6. Similar to the deformation equations given above, the extensive term as well as non-linear elasticity can independently be considered or not for obtaining the lateral expansion.

2.4.2 Feng volume-based contact model

Feng (2021b) presented an energy-conserving approach for modelling the contacts of arbitrarily shaped particles. The energy-conserving nature of the contact model ensures that the total

energy of the system is conserved during particle interactions (Feng, 2021a,c).

The normal contact force takes the form given in Equation 2.12:

$$F_{\text{Feng}} = mkV_c^{m-1}S \tag{2.12}$$

where constant $m \geq 1$, k is a constant index of normal stiffness, V_c is the contact volume overlap, S is the (scalar) contact area. This contact model is adopted and discussed in more detail in Chapter 5.

2.4.3 Dintwa contact model: Hertz calibration

Dintwa *et al.* (2008) tested the effect of finite strains on the Hertzian contact model by comparing the results predicted by Hertz for two contact cases against those obtained using the Finite Element Method (FEM). The two contact cases were essentially sphere–sphere contact and sphere–wall contact. After testing up to strains ($\frac{\delta}{2R}$) of 1.25% an extension to the Hertzian contact model was suggested. Given that in the equations presented in Dintwa *et al.* (2008) both E^* and R^* are defined just as in the Hertzian contact model, it has to be noted that neither of these equations seem to be dimensionally consistent. In Dintwa *et al.* (2008) E^* seems to have the same units as the force F.

The suggested corrections incorporate both the geometric dimensions as well as the elastic properties of the material and hence should apply to spheres of different sizes and materials of various elastic properties. However, the effectiveness of this contact model was not investigated when different parameters are used or higher strains applied.

2.4.4 Hertz contact model for ellipsoids

The popular Hertzian contact model has a more generic form that can be used for ellipsoids (Johnson, 1985; Kumar *et al.*, 2018). During deformation an elliptical contact area is formed. The force equation for the elliptical contact area takes the form shown in Equation 2.13:

$$F_{\text{Hertz}} = \frac{4}{3}E^*\sqrt{R^*}\left(\frac{\delta}{\phi}\right)^{3/2} \tag{2.13}$$

with the effective elasticity E^* defined the same as in Equation 2.4. The effective radius R^* however takes the form shown in Equation 2.14:

$$R^* = \frac{1}{2\sqrt{AB}} \tag{2.14}$$

where A and B account for the contact geometry and are given by:

$$A + B = \frac{1}{2}\left(\frac{1}{R_1} + \frac{1}{R_1'} + \frac{1}{R_2} + \frac{1}{R_2'}\right) \tag{2.15}$$

$$|B-A| = \frac{1}{2}\left[\left(\frac{1}{R_1}-\frac{1}{R_1'}\right)^2 + \left(\frac{1}{R_2}-\frac{1}{R_2'}\right)^2 + 2\left(\frac{1}{R_1}-\frac{1}{R_1'}\right)\left(\frac{1}{R_2}-\frac{1}{R_2'}\right)\cos(2\omega)\right]^{\frac{1}{2}} \tag{2.16}$$

The geometry at the point of contact is characterised by two principal radii of curvature for each of the two contacting ellipsoids: R_1, R_1', R_2 and R_2' corresponding to principal axes P_1, P_1', P_2, P_2', as shown in Figure 2.11. For the cases when $R_i = R_i'$, the contact model gets reduced to the standard Hertzian model. The angle ω is the angle between the principal axes.

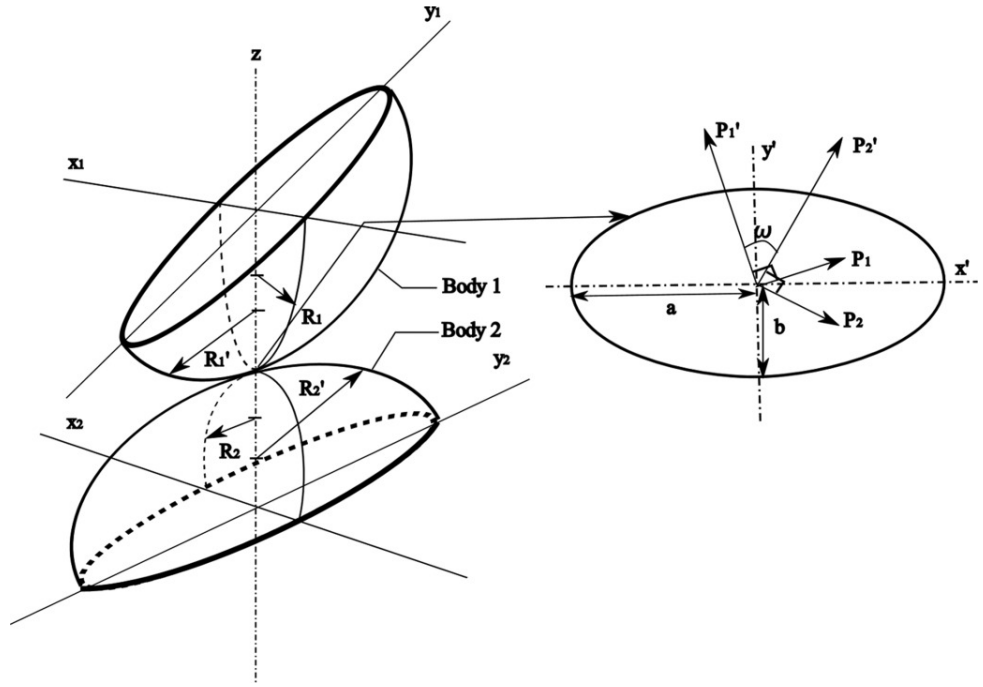

Figure 2.11: Contact between two bodies/ellipsoids with principal axes x_1, y_1, z for Body 1 and x_2, y_2, z for Body 2. The elliptical contact area is shown on the right, also indicating the angle ω between the principal axes. Figure reproduced from Kumar *et al.* (2018).

The factor ϕ accounts for the geometry of the elliptical contact area which involves evaluating elliptic integrals and is the main limitation of this contact model. Since solving the integrals adds computational complexity in the overall solution of the DEM simulation, there are different algebraic approximations available for use in terms of the ratio A/B. The one used by Kumar *et al.* (2018) is the approximation proposed by Hale (1999):

$$\phi = 1 - \left[\left(\frac{B}{A}\right)^{0.0684} - 1\right]^{1.531} \tag{2.17}$$

2.4.5 Kumar contact model for spherocylinders

Kumar *et al.* (2018) modified the Hertzian contact model (MFM) in order to be used with spherocylindrical particles. This was achieved by taking into account all the different contact scenarios in a spherocylinder–spherocylinder contact and spherocylinder–wall contact as shown

in Table 2.1. The contact scenarios effectively result in three different contact areas: circular, elliptical and rectangular. The transitions between the different contact scenarios also need to be taken into account.

Table 2.1: Contact area scenarios in spherocylinder–spherocylinder contact or spherocylinder–wall contact. Figure reproduced from Kumar *et al.* (2018).

Circular contact area (C)	Elliptical contact area 1 (E1)	Elliptical contact area 2 (E2)	Rectangular contact area (R)
 Hemisphere-hemisphere contact	 Cylinder-cylinder non-parallel contact	 Hemisphere-cylinder contact	 Plane-cylinder parallel contact
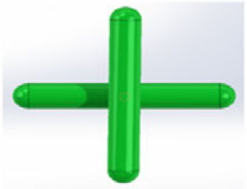 Cylinder-cylinder perpendicular contact			 Cylinder-cylinder parallel contact
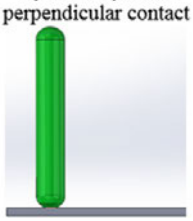 Plane-hemisphere contact			

For the circular and elliptical contact area scenarios, the generalized Hertzian (elliptical) contact model is used (Section 2.4.4), while for the rectangular contact area scenarios the linear model is used (Section 2.3.2). In order to negate any sudden changes in the contact forces when the contact takes place between the standard scenarios listed, the transitions between them need to also be taken into account.

A buffer zone is effectively put in place for the transition areas as shown in Figure 2.12. The length l_t of the buffer zone is empirically set. Within that buffer zone, a linear function is applied in order to transition between the contact scenario applicable for region 1 (spherical cap) to the contact scenario applicable for region 3 (cylindrical body).

This contact model was evaluated for a specific subset of contact cases, considered in Chapter 4. Since the chapter on contact model errors is not focused on just spherocylinders but rather uses spherocylinders simply as an exemplar shape, the results obtained were collated in Appendix A.

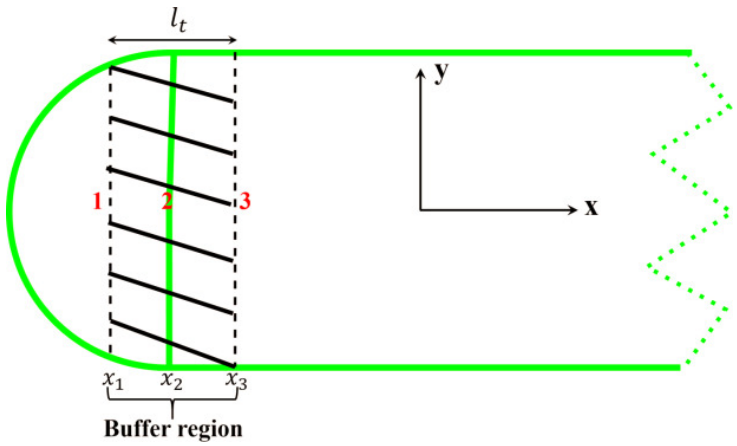

Figure 2.12: Schematic of a spherocylinder showing the transition regions between a circular contact area and an elliptical contact area. The length of the buffer region is defined by l_t. Figure reproduced from Kumar *et al.* (2018).

Limitations For the contact model formulation of the rectangular contact area scenarios, an iterative process is needed which make it less ideal for use in a DEM simulation. Additionally, the contact model should only be used at small deformations. The reason mainly lies in the methodology used in the FEA performed to derive the model. With all the simulations performed quasi-statically, some artificial boundary conditions were used in order to test specific contact scenarios. While the effect of those boundary conditions should be minimal at small strains, further testing should be performed at greater strains to evaluate its applicability.

2.4.6 Aspherix Advanced Multi-Sphere Method

Aspherix (DCS Computing, 2021) is a commercial DEM software developed by DCS Computing and successor of the open-source code LIGGGHTS (Kloss *et al.*, 2012). Within Aspherix, there is a contact model called the 'Advanced Multi-Sphere' (AMS) method which serves as a (partial) solution to the problems listed in Section 2.2.6 and by Kruggel-Emden *et al.* (2008) for the Multi-Spherical clumps method.

Beyond what is mentioned in the Aspherix documentation, there is very limited information available about how the AMS method works. According to the documentation, the contact forces are re-scaled in order to correct the coefficient of restitution. The re-scaling is performed by considering the interaction forces for each particle–particle contact, as well as the number of body–body contacts, and then re-scaling the contact forces by the number of body–body contacts. This seems to work similar to an averaging method of particle–particle contacts over body–body contacts. The effectiveness of the AMS method is further investigated in Chapter 4.

2.5 Contact models employing the Multi-Sphere approach

Expanding more on the MS approach and how contact models utilise it, the MS cluster in the DEM simulations is treated as a single rigid body and no contact forces are calculated between the cluster's constituent spheres. Where contacts are detected between the sphere of one cluster and another external body — whether that be a wall/boundary or a different particle — the contact forces are calculated depending on the contact model being used. Taking the Hertzian contact model as an example, the contact force acting on a constituent sphere of a MS cluster is calculated using Equation 2.3, where the radius of the constituent sphere in contact is used to obtain R^* in Equation 2.5.

As outlined by O'Sullivan (2011b), following the works of Das *et al.* (2008) and Garcia *et al.* (2009), the parallel axis theorem is then used to calculate the contribution of each constituent sphere to the cluster moments of inertia about a local Cartesian axis centered at the cluster centroid $\mathbf{I}^{\text{cluster}}$, as follows:

$$\mathbf{I}_{ij}^{\text{cluster}} = \sum_{s=1}^{N_s} \left(\mathbf{I}_{ij}^{s} \delta_{ij} + m^s \boldsymbol{a}_i^s \boldsymbol{a}_j^s \right) \tag{2.18}$$

where the cluster comprises N_s spheres, each with mass m^s and inertia $\mathbf{I}^s$ relative to the sphere local Cartesian axis, and δ_{ij} is the Kronecker delta. The vector $\boldsymbol{a}^s$ is given by $\boldsymbol{a}^s = \mathbf{x}_i^s - \mathbf{x}_i^{\text{cluster}}$, where $\mathbf{x}^s$ and $\mathbf{x}^{\text{cluster}}$ are the vectors describing the constituent sphere and cluster centroids, respectively.

If the cluster consists of spheres that are not overlapping between them, the total mass of the cluster is simply the sum of the masses of all the constituent spheres. In the case where the constituent spheres are overlapping, the overlap volume needs to be considered. For simple symmetric geometries the overlap volume can be analytically determined by integration and the mass and inertia values can be adjusted. For more complex geometries however, Garcia *et al.* (2009) use an approach where the cluster is overlain by a grid of cells. At the parts where a cell is overlain by one or more spheres, its mass and position are used to calculate the mass and moments of inertia.

The motion of the particle is then calculated by summing the contact forces acting on its constituent spheres. The resultant moments are determined by taking the cross product of each contact force with the vector from the contact point to the cluster's centroid. When a body or external force is applied to a constituent sphere, it must be included in both the translational and rotational equilibrium equations for the cluster. Unlike perfectly spherical particles, the normal forces can create a moment because the contact normals and vectors from the contact point to the cluster's centroid are not collinear. Additionally, shear forces generate torque, similar to single-sphere particles, but the lever arm for this tangential force moment is not equal to the sphere's radius.

Using this approach, the clusters themselves are rigid and each cluster is itself a single particle, with six degrees of freedom (in three dimensions). Once the centroidal position and the

rotations of the clusters have been updated, then the new positions of the constituent spheres are calculated, prior to progressing to the contact resolution stage of the analysis and moving on to the next time increment.

While the MS approach provides a versatile way of modelling non-spherical particles, its greatest disadvantage arises when the constituent spheres have significant overlaps. Due to these large overlaps, if one constituent sphere contacts a particle or boundary, the adjacent spheres are likely to also contact the same particle or boundary. This leads to a single contact being detected multiple times, resulting in an increased resultant force. The implications of this phenomenon are examined in detail in Chapter 4.

2.6 Soil mechanics application of DEM

Moving beyond just particle shape and the various contact models in DEM, its application in soil mechanics is examined and a brief overview is provided. The elastic or small-strain shear modulus of soil, G_0, depends on the effective confining stress, σ', as do the elastic bulk modulus, K_0, and Young's modulus. Considering the relation $G_0 \propto \sigma'^m$, experiments have found that the exponent $m \approx 1/2$ for many real soils. However, theoretical analyses based on Effective Medium Theory (EMT), which can describe the macroscopic properties of composite materials, have consistently found $m = 1/3$ for a range of regular and random packings, matching analytical solutions for smooth spheres with Hertzian interactions (Duffy & Mindlin, 1957; Walton, 1987; Chang *et al.*, 1991; Santamarina & Cascante, 1996; Mcdowell & Bolton, 2001). A nonlinear contact interaction (for example, based on Hertz) is required to capture the stress dependence of the elastic moduli (Yimsiri & Soga, 2000). The limitations of EMT for capturing the variation of the bulk modulus, K, of soft two-dimensional particle assemblies were recently highlighted by Cantor *et al.* (2021). Goddard (1990) proposed two mechanisms to explain the discrepancy between theoretical analyses and experiments which were investigated by Mcdowell & Bolton (2001): (i) the presence of conical asperities at real interparticle contacts; (ii) an increasing number of contacts with increasing confining stress due to the buckling of force chains.

DEM simulations naturally incorporate the second mechanism. In addition, micro-mechanical expressions have been developed for the elastic moduli which incorporate the coordination number, allowing for a varying number of contacts (Agnolin & Roux, 2007). Allowing the number of interparticle contacts to vary improves agreement with experimental data compared to EMT (Makse *et al.*, 1999). However, buckling is irreversible and not strictly applicable to elastic soil (Mcdowell & Bolton, 2001). Furthermore, this mechanism is ineffectual for idealised packings of monosized spheres in which new contacts cannot form. Rough-surface DEM contact models have been proposed to account for the first mechanism – for example, Yimsiri & Soga (2000) and Otsubo *et al.* (2017), the latter building on the work of Cavarretta *et al.* (2010) and O'Donovan *et al.* (2015). The underlying idea is that, at small strains, the response at a contact is dominated by the deformation of asperities and hence the stiffness is low. At high confining stresses, beyond

a threshold which depends on the surface roughness, the response reverts to that for Hertzian spheres, where $m \approx 1/3$. These models succeed in increasing m in the $G_0 \propto \sigma'^m$ relationship and enable good agreement with experimental data at low-to-moderate confining stresses.

One of the key assumptions of Hertzian mechanics (Hertz, 1882) is very small deformations (Dintwa *et al.*, 2008). At high confining stresses, at which the exponent $m \approx 1/3$ in the $G_0 \propto \sigma'^m$ relationship for rough-surface contact models, the validity of the theory proposed by Hertz becomes questionable. As mentioned in Section 2.4.1, Tatara (1991) extended Hertz's theory for one special case: uniaxial compression of a single unbreakable sphere to large strains between two rigid plates. The extended theory developed by Tatara includes the lateral extension of the sphere at its equator due to the Poisson effect to give an oblate spheroid. This lateral extension is precluded in conventional DEM simulations, where fundamental spheres remain spherical and cannot deform. Therefore, at large strains, any cross-sectional area of a uniaxially compressed Hertzian sphere in DEM, and hence its stiffness, is underpredicted. The influence of the Poisson effect on soils is further studied in Chapter 6.

2.7 Contact model usage and knowledge gaps

A representative sample of the contact models and shapes used in DEM literature has been been compiled in Table 2.2. It can be seen that mainly the Hertzian or the Linear model is used even though their efficacy for use in non-spherical particles is questionable.

Generally, the established contact models used in DEM simulations have been developed for spheres. Attempts have been previously made to establish contact models for non-spherical particles, however the overwhelming majority of non-spherical simulations still use the Linear model or Hertz.

The focus of this thesis is addressing the knowledge gaps identified:

- Chapter 4 — providing a comprehensive quantification of errors for using the MS method coupled with contact models based on spheres in non-spherical particle simulations.

- Chapter 5 — examining whether contact models based on volume overlaps are more suitable for non-spherical particle contacts rather than conventional distance overlap-based models.

Additionally, the methodology that has been established in Chapter 3 has been applied to an open question in geomechanics/geotechnics: which factors are responsible for the stress dependence of the elastic moduli of soil. This is further explored in Chapter 6.

Table 2.2: Contact model and shape usage in DEM literature.

Particle Shape	Contact Models & Literature
Ellipsoids 	**Hertz (Ellipsoids):** Zheng *et al.* (2013); Kildashti *et al.* (2018)
Superquadrics 	**Hertz:** Soltanbeigi *et al.* (2018); Arifuzzaman *et al.* (2020) **Gaussian curvature radius*:** Podlozhnyuk *et al.* (2017)
Spherocylinders 	**Linear:** Pournin *et al.* (2005); Guo *et al.* (2018); Mahajan *et al.* (2018) **Kumar*:** Kumar *et al.* (2018)
Polyhedra 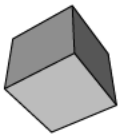	**Hertz:** Harkness *et al.* (2016) **Linear:** Höhner *et al.* (2011) **LVB:** Eliáš (2014); Govender *et al.* (2020)
Spherical Harmonics 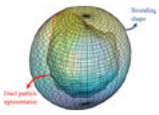	**LVB:** Wang *et al.* (2021) **Lennard-Jones potential:** Capozza & Hanley (2021)
Multi-Spherical clumps 	**Hertz:** Marigo & Stitt (2015); Soltanbeigi *et al.* (2018) **Linear:** Favier *et al.* (2001); Höhner *et al.* (2011); Haeri (2017); Berry *et al.* (2021)
Level Sets 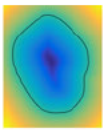	**Linear:** Kawamoto *et al.* (2016); Davis *et al.* (2021)
Potential Particles 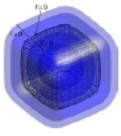	**Linear:** Harkness (2009); Boon *et al.* (2013)

*Contact model proposed in paper.

Chapter 3

Methodology and Verification

In this chapter, the underlying methodology used throughout the entire thesis is presented, along with the verification process followed. It was presumed that understanding how the contact forces are formed on a particle-by-particle basis was integral. Since the Finite Element Method (FEM) requires the use of a mesh, which further divides the granules of interest in smaller elements, it provides a good resolution of the contact forces present in various contact situations. Therefore, the FEM was used as the primary method to obtain the contact forces as was previously done in the works of Wu (2001); Dintwa *et al.* (2008); Rathbone *et al.* (2015); Kumar *et al.* (2018).

3.1 Uniaxial compression of a sphere

The methodology used, as well as its verification, was developed following a similar process from Rathbone *et al.* (2015). The commercial software Abaqus (Dassault Systèmes, 2015) was used to quasi-statically compress a sphere between two rigid plates as shown in Figure 3.1. The granule and material properties match the ones used by Rathbone *et al.* (2015), albeit ignoring plasticity. Those included a radius R of 0.1 mm, Young's modulus E of 6.1 GPa and Poisson's ratio ν of 0. The specific Poisson's ratio though is considered a special case so a more common Poisson's ratio of 0.3 was selected beyond the first verification stage. Therefore, for subsequent analyses the material properties used were the ones listed in Table 3.1, unless otherwise stated in the relevant section. While not necessary for the quasi-static compressions, the density $\rho = 1{,}000\,\mathrm{kg/m^3}$ was arbitrarily selected for the kinematic collisions explained in Section 3.2.

Table 3.1: Material properties used for both the quasi-static compression and kinematic collision simulations.

Property	Value	Units
Poisson's ratio (ν)	0.3	–
Elasticity/Young's modulus (E)	6.1	GPa
Density (ρ)	1,000	$\mathrm{kg/m^3}$

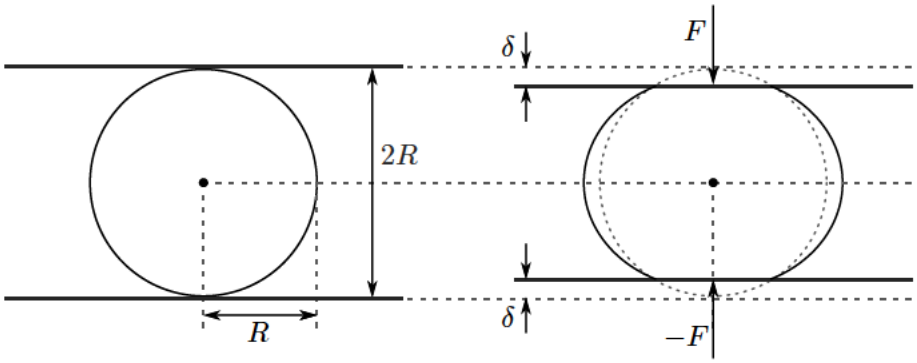

Figure 3.1: Schematic showing a single sphere with radius R before and after uniaxial compression between two rigid plates, with F being the normal force applied on the granule by the rigid plates and δ being the deformation of the sphere at each point of contact.

Strain Definition It is important to note that strain in this work is defined as:

$$\text{Strain} = \frac{\delta}{2R} \times 100\% \tag{3.1}$$

it is expressed as a percentage of the deformation (δ) per point of contact divided by the diameter ($2R$) of the granule. For the purpose of this thesis the terms 'axial strain' and 'average strain' are interchangeable. Additionally, to maintain consistency, the deformation δ considered for the strain definition is that seen in the FEM approach which more closely resembles reality and is equivalent to δ_{wall} from Figure 2.10. Although the maximum deformation in all compression cases was still equivalent to 5% average strain, it was split between 2 different points of contact. Therefore only 2.5% average strain was effectively applied per contact as opposed to having the full 5% applied on a single contact in a kinematic collision. This is also demonstrated in Figure 3.2.

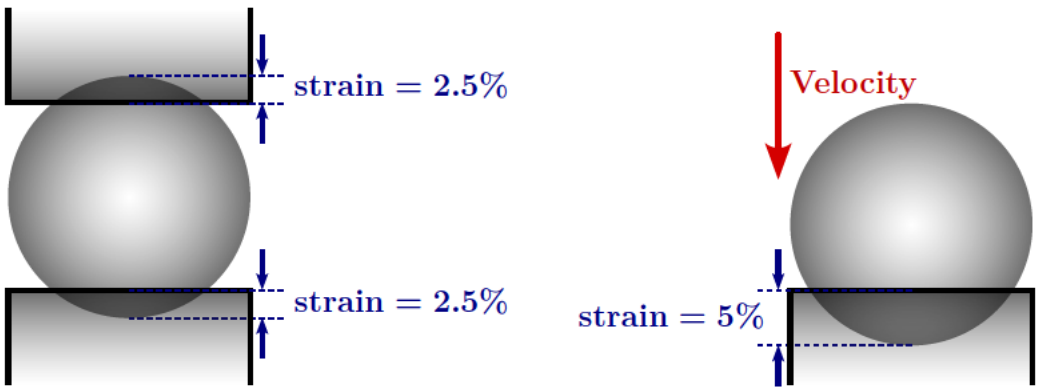

Figure 3.2: Schematic indicating how strain is applied on a spherical granule during quasi-static compressions (left) and kinematic collisions (right). The average strain applied in both cases is 5%, but it is distributed differently due to the nature of each contact.

In order to replicate the granule conditions from a DEM simulation, the granule was modelled as an elastic body using the inbuilt routine in Abaqus for isotropic materials which requires

only the Young's modulus and Poisson's ratio. An octant of the entire sphere was simulated using three planes of symmetry and 2,196 'C3D8R' (8-node linear brick, reduced integration with hourglass control) elements as shown in Figure 3.3. The full list of options applied when setting up the Abaqus simulations can be found in Appendix B. The mesh was refined at the point of contact to properly capture the normal force acting on the rigid plate as well as the granule deformations. Following a mesh dependence study (Section 3.3), which also included meshing with quadratic elements, the selected mesh was deemed sufficient as the difference in the results was of the order of 0.1–0.2%. The use of linear elements was favoured in order to keep the comparison with further research involving kinematic collisions consistent.

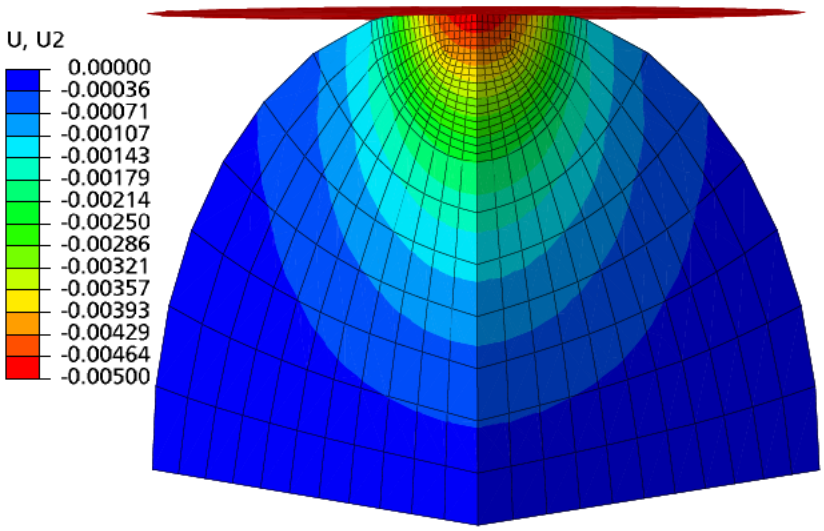

Figure 3.3: Octant of the sphere simulated in Abaqus FEA at an average strain of 5%. The contours represent the y-axis displacement (perpendicular to the plate) measured in mm.

The plate used to compress the sphere was modelled as a 3D analytical rigid shell and the compression was performed by setting a predefined displacement boundary condition on the plate. The sphere's deformation in the simulation was obtained from the distance the plate was displaced while compressing the spherical granule and the normal contact force was obtained from the reaction force applied on the plate. An initial comparison was performed with Rathbone *et al.*'s work to determine the best way to set up the model, where the granule was subjected to deformations of up to 0.1% average strain. The results are shown in Figure 3.4 and as can be seen, the FEA results match up with both Hertz and the literature results. As already mentioned, plasticity was also modelled in Rathbone *et al.* and that is the reason why the FEA results of this study appear to be in better agreement with the Hertzian contact model than those of Rathbone *et al.* (2015).

For the final stage of the verification, the compression was stopped when the total deformation applied reached an average strain of 5%: a common heuristic for the maximum permissible overlap between spheres in DEM simulations as well as the limit to Abaqus' inbuilt elastic

material model routine (Dassault Systèmes, 2015). The results of the FEA were once again compared with the analytical solutions of Hertz (1882) and Tatara (1991) given in Equation 2.3 and Equations 2.9–2.11 respectively. The comparison with the latter allows the reliability of these implicit simulations to be verified against an analytical solution developed for non-infinitesimal strains.

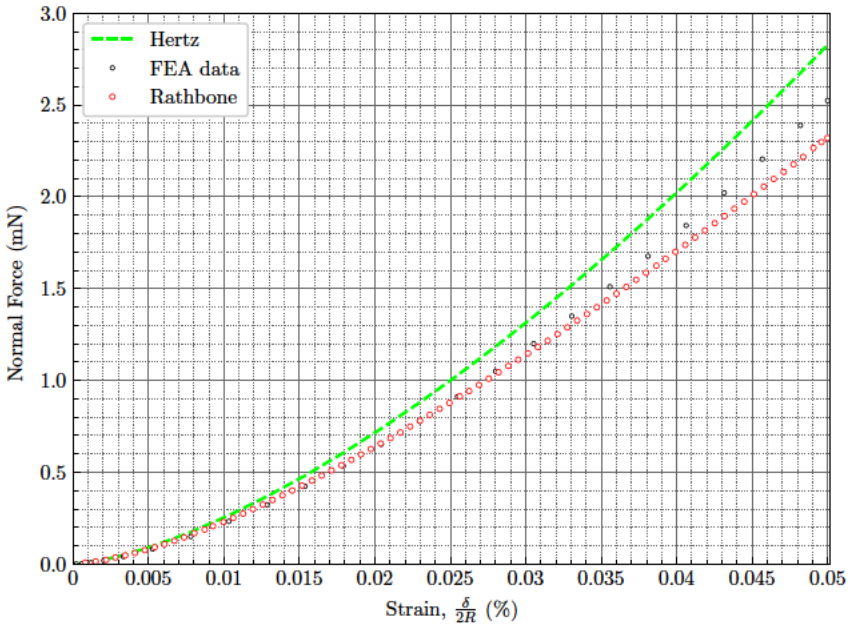

Figure 3.4: Comparison between Rathbone results (includes plasticity), Hertz and the FEA up to 0.05% strain. In this case, the material's Poisson's ratio $\nu = 0$.

The normal contact force F is plotted against axial strain and the results are presented in Figure 3.5 for both values of Poisson's ratio used. In both cases, the FEM force curve was between the Hertz and Tatara analytical solutions throughout the deformation range that was tested. For the first case, where the sphere had a Poisson's ratio of 0, the disparity between the Hertz force increases monotonically with strain. At maximum strain, the disparity reaches about 5.5%. When the FEM force data is compared with the Tatara force, the disparity stabilises at around 5% at strains beyond 1%.

As for the sphere with a Poisson's ratio of 0.3, at maximum strain the discrepancy of the FEM force data and the Hertz analytical solution reaches about 11%. For comparison, the disparity between the FEM force data and the Tatara analytical solution stabilises at around 2% at strains beyond 1%. This is considered acceptable for the purposes of verification. On the contrary, the magnitude of the disparity between the FEA force data and Hertz increases monotonically with strain: from 3.8% at 0.5% strain to 8.0% at 1.5% strain to 11.0% at 2.5% strain. The deviations present very clearly capture the difference between a contact model designed for infinitesimal deformations (Hertz) and one designed for large deformations (Tatara).

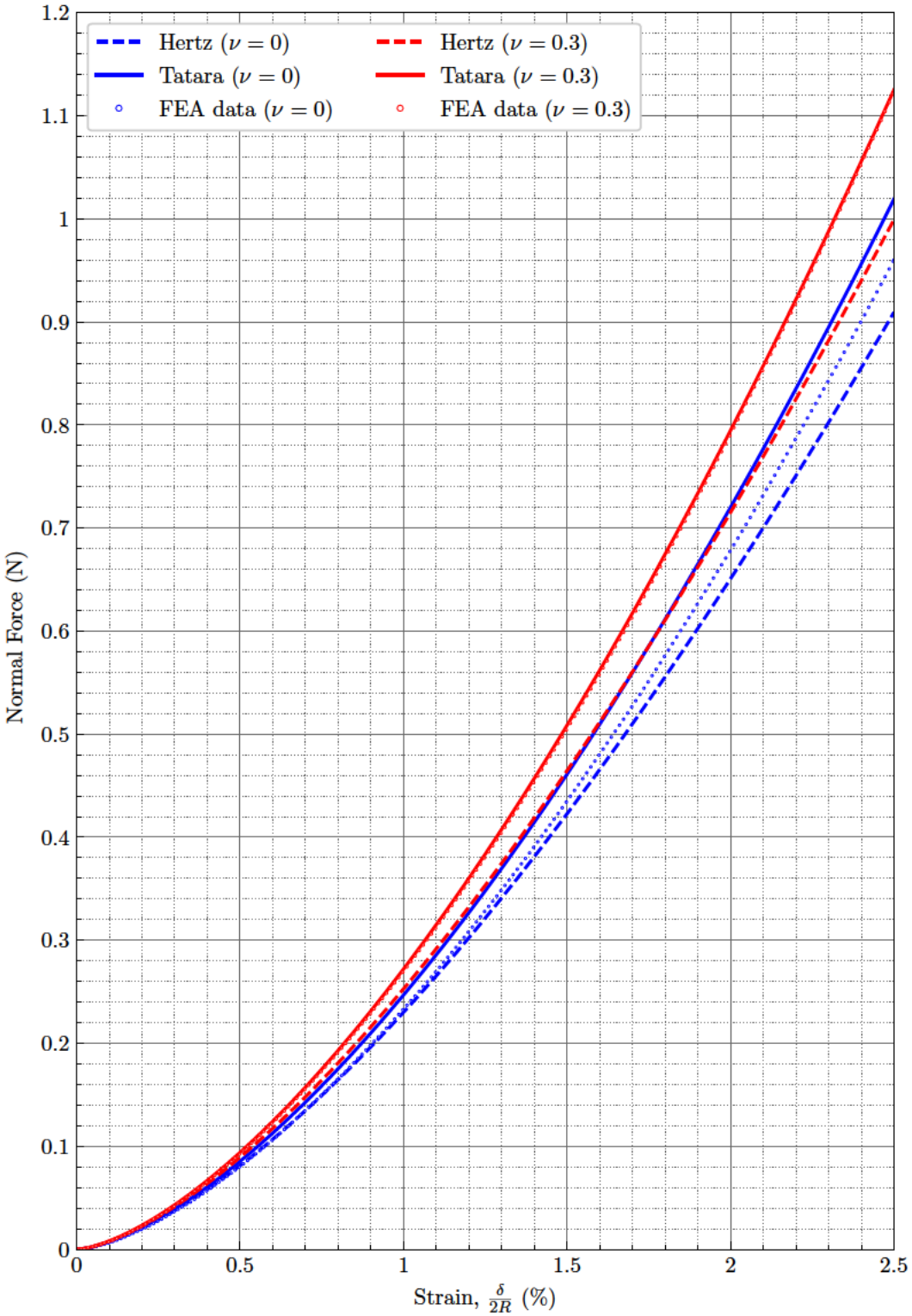

Figure 3.5: Comparison between FEA, Hertz and Tatara contact models when a sphere is compressed by two rigid plates until a strain of 2.5% is applied per contact. The comparison is performed for Poisson's ratios of $\nu = 0$ and $\nu = 0.3$, shown in blue and red respectively.

3.2 Kinematic collisions of a sphere

The quasi-static compressions are convenient for simulating parallel granule–granule contact. However, for non-parallel and non-spherical granule interactions the entire kinematic collision has to be simulated. Therefore, in order to verify the kinematic collisions, a series of simulations of a sphere colliding with a rigid plate were performed.

The simulations were performed kinematically by setting a sphere to collide perpendicularly with a rigid plate. The Abaqus assembly consisted of a quadrant of a spherical granule using two symmetry planes and a rigid plate positioned horizontally. The plate was fixed while the sphere was assigned an initial velocity in the y-axis direction in order to ensure a perpendicular collision.

Since the collisions were modelled kinematically, a parametric study was necessary to plot the entire force–deformation curves in order to minimise any inertial effects present. That is to ensure that the results are not affected by any material properties used such as the density of the sphere. This was done by setting the initial velocity of the sphere and extracting the force and deformation at the endpoint of the simulation. That would be the moment where the sphere momentarily reaches a static state, which in this case coincides with the moment the maximum deformation is achieved.

Therefore the data obtained at the designated simulation endpoints were the reaction force acting on the plate and the deformation applied on the sphere during the collision. The reaction force was straightforward to obtain directly from Abaqus, whereas the strain needed some additional processing. A set of two nodes was created on the sphere, one at the top and one at the bottom. The deformation applied was defined as the difference between the length of the original diameter formed by the two nodes and the deformed one at the simulation endpoint. The strain was then obtained by dividing the deformation applied on the spherical granule by its diameter. Additional information regarding the setup of the kinematic collision models for more complex assemblies is provided in Section 4.1.1.

The final force–strain curve obtained from the kinematic collisions was then compared with the contact force obtained from the sphere compressions. As can be seen from the comparison in Figure 3.6 the results are in good agreement and still fall in between the predictions from Hertz and Tatara, with the errors consistently being $\leq 2.8\%$, which is acceptable. Consequently, the kinematic collision simulations can also be considered verified. Therefore, while not perfect, the results obtained from the FEA performed are considered as the correct solutions and the comparisons performed in the subsequent chapters use the FEA results as a basis unless specified. One of the limitations of using FEM is that the results obtained can be affected by the mesh used. To alleviate this, a mesh dependence study was performed and presented in the following section.

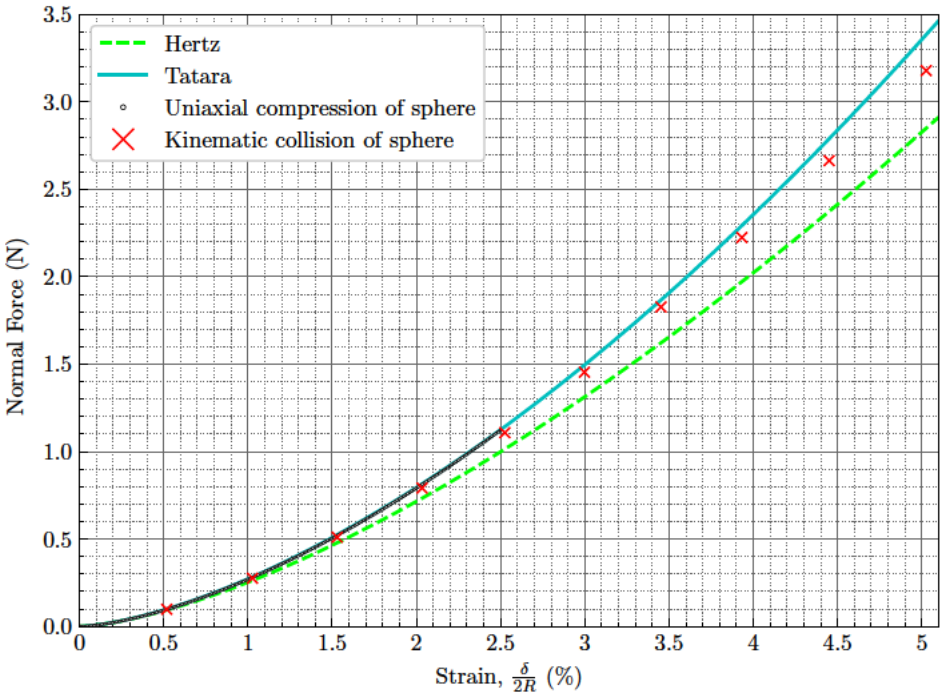

Figure 3.6: Kinematic collision Force–Strain curve obtained from a parametric study. The force response obtained from the uniaxial compressions is also included, as well as the force responses predicted from Hertz and Tatara's models.

3.3 Mesh dependence study

In order to properly capture the contact forces as well as how the granules deform in all the different simulations performed, a proper meshing strategy had to be established. Ideally a very fine mesh would be used on the entire granule but such an approach was not practical as that would entail a larger number of elements being used and thus more computational power/time needed for the simulations to run. Therefore, after some iteration, it was determined that designating Point of Contact (PoC) regions where the mesh would be more refined and having a coarser mesh for the rest of the granule was the most appropriate approach. Hence a proper balance between accuracy and speed was achieved.

In order to accommodate the PoC regions, the granule was partitioned within Abaqus. A vertical cross-section through the center of the spherical granule is shown in Figure 3.7 for visual aid. The granule was partitioned by using an auxiliary sphere centered at the exact points of contact and a radius $= 0.3 \times R$. The shaded areas indicate the designated PoC regions where the mesh was finer. The radius of the auxiliary sphere was iteratively selected based on the deformations and the von Mises stress contours produced when strain was applied on the granule. The ability to capture the contours of both variables well (refer back to Figure 3.3) seemed like a good starting point that led to the final radius selected. The sizes of the elements at the PoC region were overall about 10–20 times smaller in terms of volume compared to the sizes of the

elements on the rest of the granule body. This meshing technique that incorporates a general mesh size and a more refined PoC region was used as a blueprint for all simulations performed in the thesis, regardless of the shapes of the granules modelled.

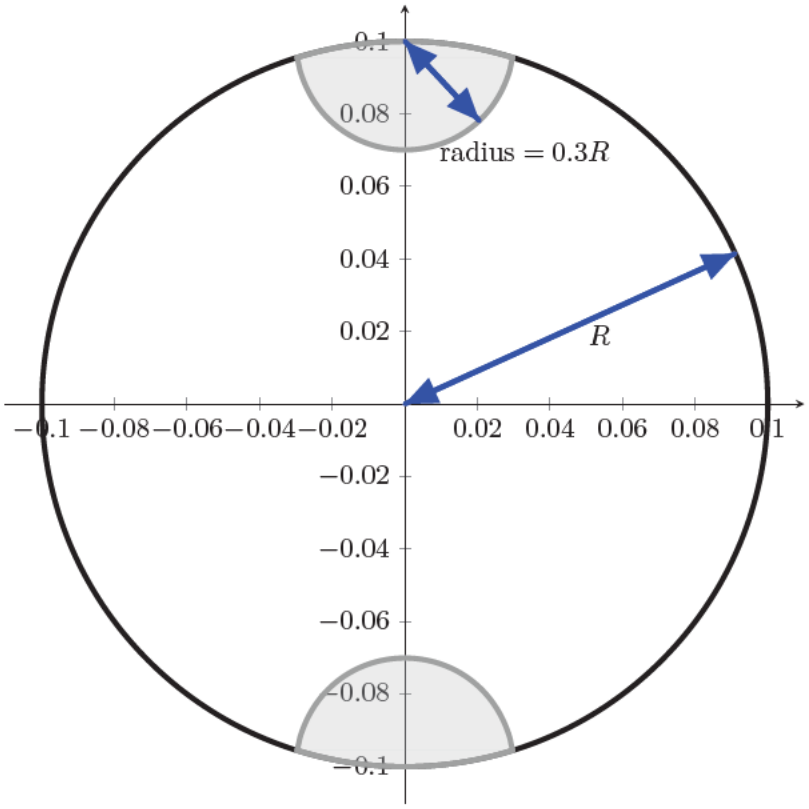

Figure 3.7: Spherical granule cross-section view (for uniaxial compressions). The shaded areas indicate the designated PoC regions, where the mesh is more refined.

3.3.1 Mesh dependence study: Quasi-static compression results

A mesh sensitivity analysis was performed by plotting the residuals of the force obtained at maximum deformation from the uniaxial compressions of a sphere against the number of Degrees of Freedom (DoF). The residuals were calculated by comparing the force at maximum deformation obtained using the different meshes tested against the one obtained with the finest mesh. The results are summarised in Figure 3.8 for the uniaxial compressions, with the relevant element sizes at the PoC and their respective DoF shown in Table 3.2.

Instead of using linear elements, quadratic elements could have been used. With a smaller number of elements they can provide superior accuracy compared to the linear elements. However, taking into account that only hexahedral elements were used in the models, the quadratic elements could not be used for the kinematic collision simulations. Hence, the linear elements were selected for all the work performed except where explicitly stated otherwise.

The residuals were calculated by using the finest mesh as the basis to calculate the errors

Table 3.2: The element sizes at the Point of Contact (PoC) are displayed next to the total Degrees of Freedom (DoF) of the model for the uniaxial compressions of a sphere. The final mesh size selected for the quasi-static compressions is the one depicted in the 4^{th} row of the table.

PoC element size (mm)	Degrees of Freedom
0.01	636
0.006	948
0.003	3260
0.002	**6484**
0.0015	12210

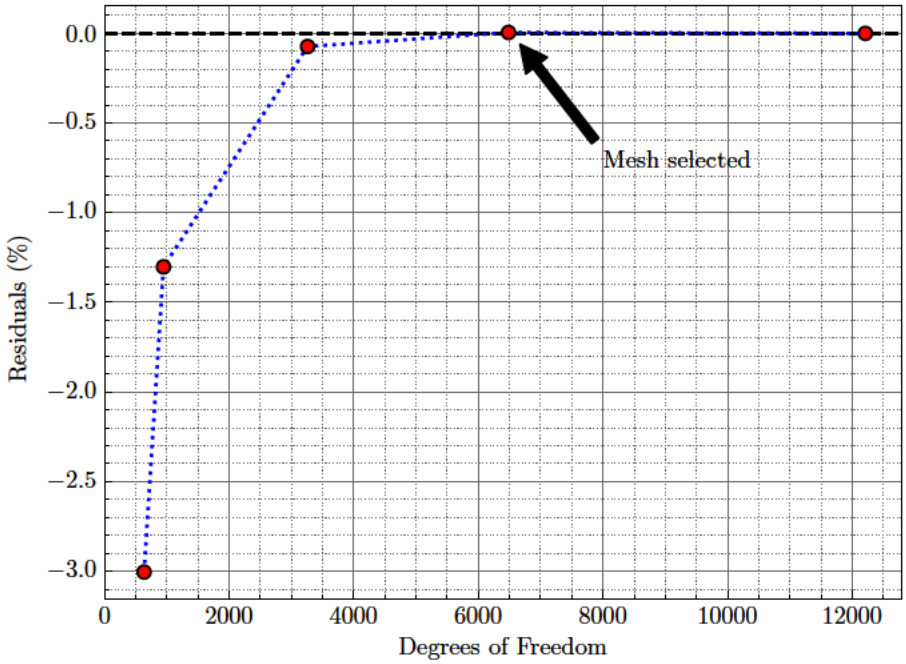

Figure 3.8: The residuals of the forces obtained at maximum strain in the uniaxial compressions of a sphere were plotted against the Degrees of Freedom. The negative signs represent an underprediction of the forces obtained.

from the coarser meshes used. That is the reason the mesh that has the most Degrees of Freedom is lying on top of the 0% residual line. The mesh selected is the one with an element size of 0.002 mm at the PoC as it is clear that the mesh is sufficiently fine to produce virtually the same answer as the finest mesh tested. The residuals calculated for the selected mesh are less than 0.005% in absolute terms.

3.3.2 Mesh dependence study: Kinematic collision results

Following a similar procedure, an additional mesh sensitivity analysis was performed for the kinematic collision cases. The same PoC region was selected for a finer mesh, although a quarter of the sphere was modelled in the kinematic collision simulations.

The results are summarised in Figure 3.9, with the relevant element sizes at the PoC and their respective DoF shown in Table 3.3. While the PoC element sizes are similar to those used for the uniaxial compressions, the reason the DoF is higher is that a quarter of the sphere was modelled in the kinematic collisions rather than just an octant of one.

Table 3.3: The element sizes at the Point of Contact (PoC) is displayed next to the total Degrees of Freedom (DoF) of the model for the kinematic collisions of a sphere on a flat plate. The final mesh size selected for the kinematic collisions is the one depicted in the 3rd row of the table.

PoC element size (mm)	Degrees of Freedom
0.006	1488
0.003	4548
0.002	**8607**
0.0018	16644
0.0016	31175

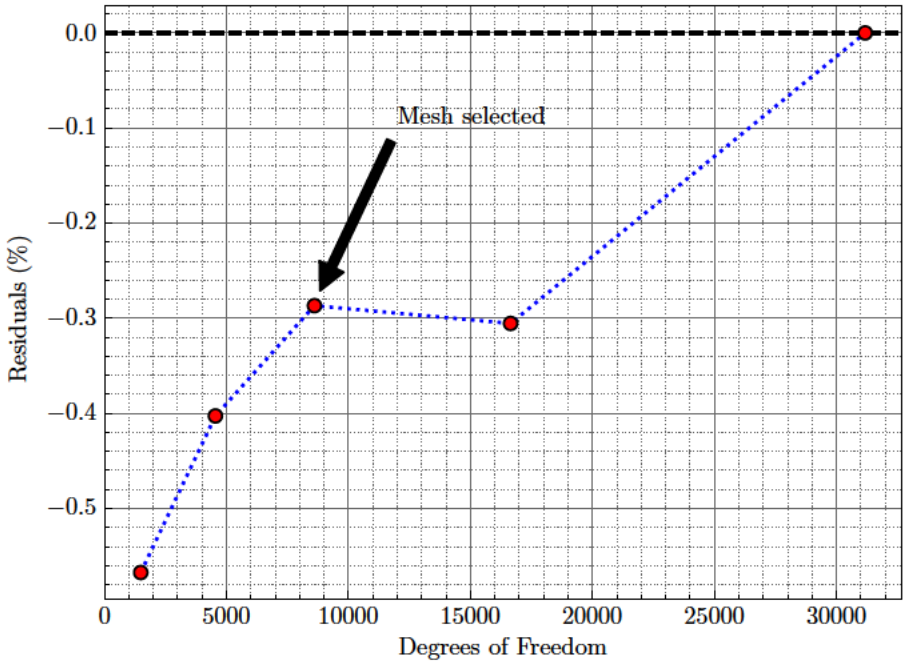

Figure 3.9: The residuals of the forces obtained at maximum strain in the kinematic collisions of a sphere on a flat plate were plotted against the Degrees of Freedom. The negative signs represent an underprediction of the forces obtained.

The residuals were obtained using the same method as used for the uniaxial compressions. However, because these are kinematic collisions which require the use of the explicit solver in Abaqus, the situation is not as straightforward.

At a first glance it can be seen from Figure 3.9 that the results do not seem to converge to a single solution. The residuals however at that point are all less than 0.6% in absolute terms which is acceptable. The reason for this fluctuation can be attributed to the fact that the endpoints of the five different simulations were slightly different, unlike the uniaxial compressions. With the implicit solver (used for the uniaxial compressions) the data for all five simulations was collected at the exact same strains, whereas the explicit solver does not have the same capability. The mesh differences have a slight effect on the endpoint of each simulation, which causes the endpoint strain at each simulation to differ ever so slightly from the rest of the simulations even though the rest of the simulation parameters remained unchanged. It was observed that the endpoint strain was increasing as more elements were used, which also affects the force obtained in every case. As can be seen from the results in Figure 3.9 though, the residuals are negligible. Therefore, to simplify the simulation setup, the element size selected for the kinematic collisions was the same as the one used for the uniaxial compressions as the residuals were already sufficiently small ($< 0.3\%$).

Normally, the element size of the mesh for these kinematic collisions should also take into account the wavelengths of the waves propagating within the particle after the initial impact. Monitoring the stresses in the particle, however, and the waves propagating after impact is not a focal point of this work. Since the main interest is the normal contact forces present during impact, as long as those are captured accurately, the mesh can be considered sufficient. Therefore a more extensive analysis for determining the mesh size was deemed unnecessary.

With both the quasi-static compression and kinematic collision simulations verified and appropriate meshing sizes selected this chapter is concluded. The main simulation methods used throughout the thesis are summarized here. While this is not an extensive breakdown of the methodology, additional information is provided in the following chapters where relevant.

Chapter 4

Quantifying the errors in Multi-Sphere DEM

Two sources of error can be identified by using the multi-spherical approach of modelling non-spherical particles (Figures 4.1 and 4.2) that directly affect the normal contact forces present in particle collisions. The first one stems from the difference between the actual particle shape and its multi-spherical approximation. Although similar, the multi-spherical cluster will always be a mere approximation of the true particle. The second source of error arises from the contact model used in the DEM simulations since in such cases a contact model developed for spheres is usually adopted, even though the original granule that is emulated is not a sphere. How these two errors were quantified and their significance will be the focal point of this chapter.

There is a case to be made about an additional source of error coming from the Poisson effect, which may be considerable at Poisson's ratios approaching 0.5 (Constandinou & Hanley, 2022). This will be further expanded on in Chapter 6. For this part of the thesis, the error stemming from the Poisson effect was considered negligible compared to the other two sources of error identified, as a Poisson's ratio of 0.3 was used. While the potential for inaccuracy when using the multi-spherical approach is well known (Kruggel-Emden *et al.*, 2008; Höhner *et al.*, 2011), to the author's knowledge, no rigorous quantification of the errors present has been conducted previously.

For the quantification of both errors highlighted, the Finite Element Method was used to simulate two granules coming into contact. While there are infinitely many particle shapes that can be constructed from spheres, rod shaped spherocylindrical particles were chosen as an exemplar particle shape since rods are simple and easy to parametrise. Results using this exemplar shape are expected to be qualitatively applicable to any Multi-Spherical (MS) system.

The chapter will be split in five sections; 4.1 detailing the techniques used to model the MS rod contacts, 4.2 quantifying the contact model error in MS DEM, 4.3 quantifying the shape approximation error in MS DEM, 4.4 suggesting the optimal rod configuration and 4.5 containing

the chapter conclusions. For Section 4.2, the contact model error in MS DEM was quantified by comparing the forces obtained from MS rod contacts in the FEA against the forces predicted by different DEM contact models in an identical contact scenario. The contact models mainly examined were the Hertzian CM (Hertz, 1882) due to its importance for spherical granules and Tatara's CM (Tatara, 1991; Tatara *et al.*, 1991) as it was designed to be used for large strains. In DEM terms, values beyond roughly 1–2% could be considered to be large strains. Furthermore, the Linear CM (Thornton *et al.*, 2011) and the 'Advanced Multi-Sphere Method' used in Aspherix (DCS Computing, 2021) were also evaluated. For Section 4.3, the shape approximation error was quantified by comparing the force responses of perfect spherocylinder rod contacts against MS rod contacts of the same length but consisting of a variable number of spheres. The errors and quantification methods are summarized in the schematic provided in Figure 4.3.

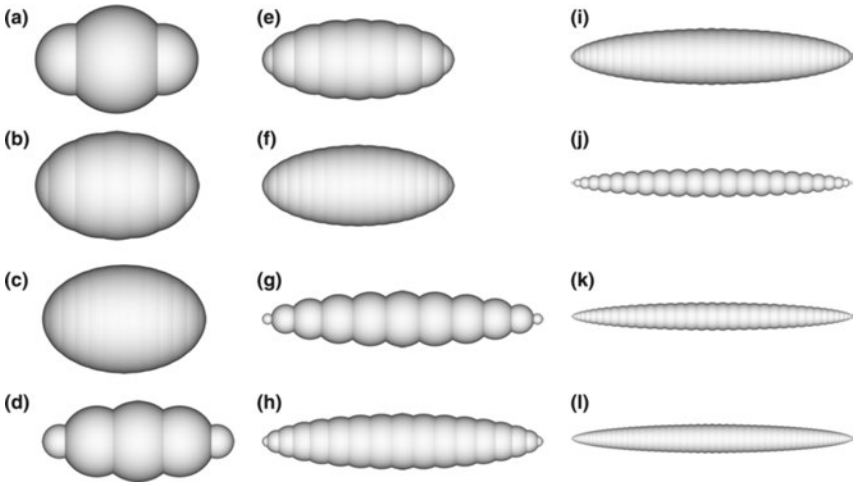

Figure 4.1: Examples of the multi-spherical approach used to represent ellipsoids with various aspect ratios s and number of constituent spheres N: (a) $s = 1.5$, $N = 3$, (b) $s = 1.5$, $N = 7$, (c) $s = 1.5$, $N = 13$, (d) $s = 2.35$, $N = 5$, (e) $s = 2.35$, $N = 9$, (f) $s = 2.35$, $N = 17$, (g) $s = 5.0$, $N = 11$, (h) $s = 5.0$, $N = 17$, (i) $s = 5.0$, $N = 33$, (j) $s = 10$, $N = 23$, (k) $s = 10$, $N = 37$, (l) $s = 10$, $N = 55$. Image reproduced from Markauskas *et al.* (2010).

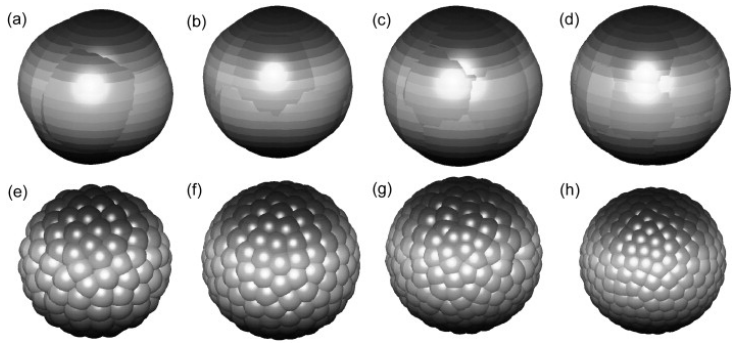

Figure 4.2: Examples of the multi-spherical approach used to represent different multi-sphere approximations of an aluminium oxide particle using 7, 12, 17, 22, 135, 190, 245 and 300 spheres respectively. Image reproduced from Kruggel-Emden *et al.* (2008).

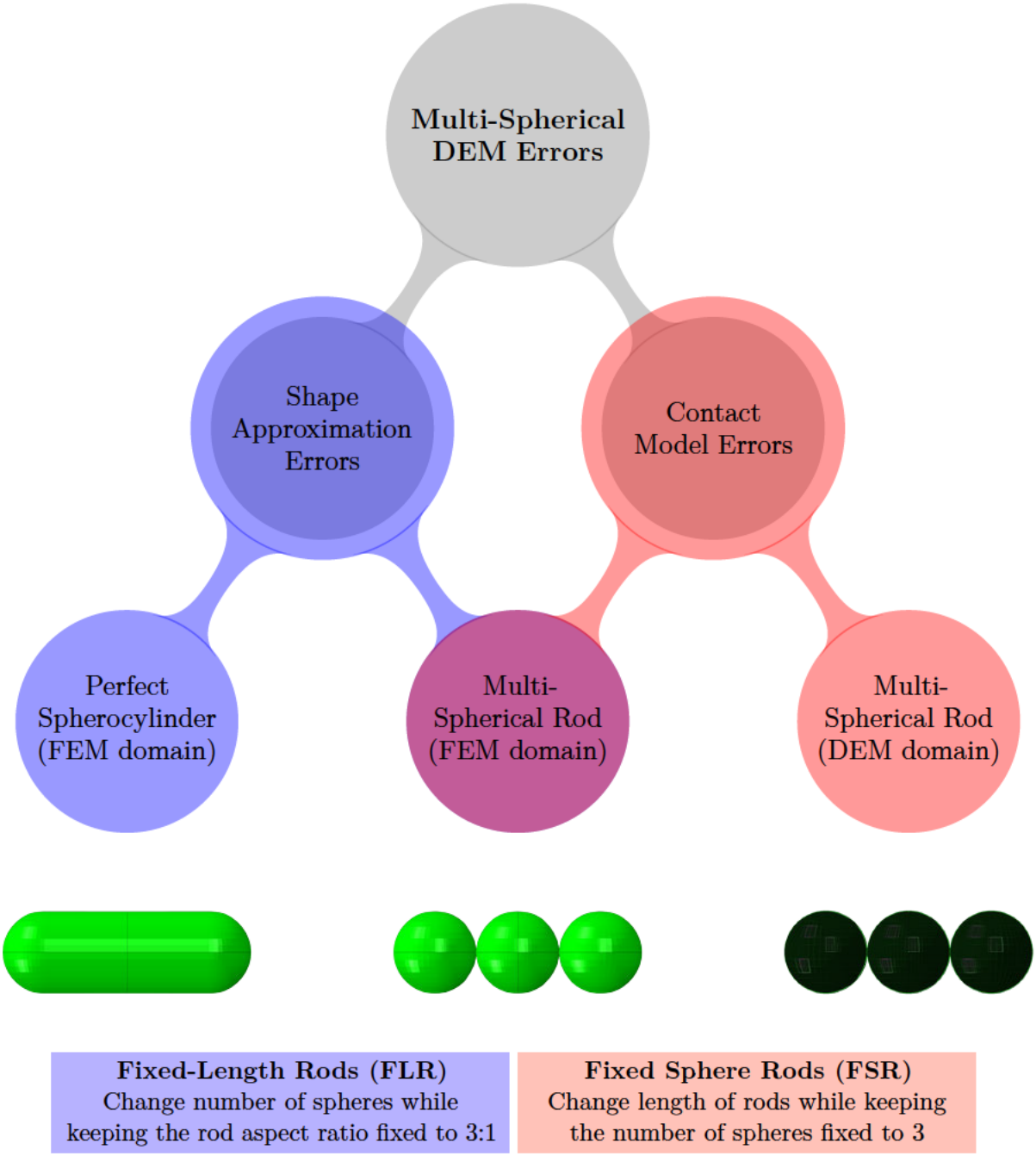

Figure 4.3: Schematic showing the errors present in multi-spherical DEM and the methods used to quantify them.

4.1 Simulation-Model Setup

As mentioned in Section 3.2, quasi-static compressions are convenient for simulating parallel granule-granule contact. However, for non-parallel and non-spherical granule interactions the entire kinematic collision has to be simulated in order to obtain the correct force responses due to the lack of symmetry.

4.1.1 Angled Collisions: Kinematic Collisions

All non-parallel contact simulations were performed kinematically by setting two identical granules on a collision course vertically along the y-axis. The Abaqus assembly consisted of just the two granules. This can be seen in the schematic in Figure 4.4 with a variable angle θ used to test different contact configurations. Both of the granules were given initial velocities with the same magnitude but in opposite directions along the y-axis. No other boundary conditions were set.

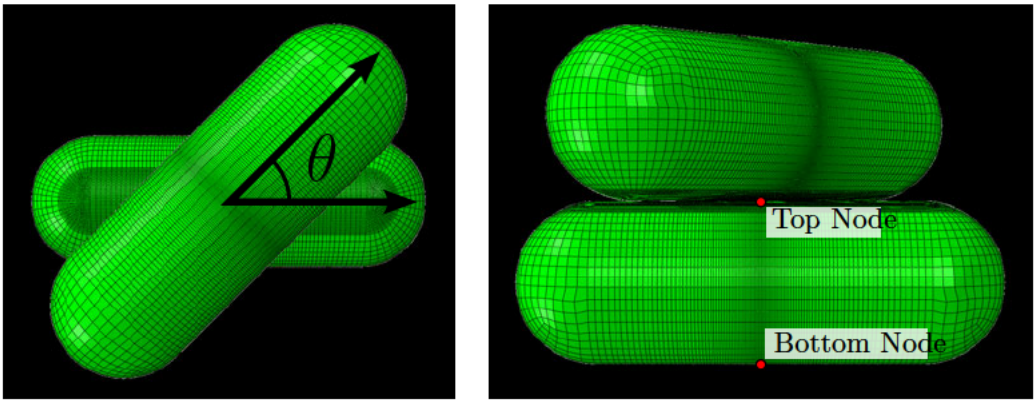

Figure 4.4: Schematic demonstrating how the kinematic collision simulations were set up on Abaqus. The top view is on the left of the figure while the side view is on the right. The angle changing in the different cases is the designated angle θ in the schematic.

Since the collisions were modelled kinematically, parametric studies were necessary for data collection in order to minimise any inertial effects present. That is to ensure that the results are not affected by any material properties used such as the density of the granules. This was done by setting the initial velocities of the granules and extracting the force and deformation at the endpoint of the simulation. That would be the moment where the granule — or at least the part of interest of the granule — momentarily reaches a static state.

There were a few different ways to define the simulation endpoint: when the force on each granule would be at a maximum; when the deformation would be at a maximum; or when the total kinetic energy of the system would be at a minimum. The latter method proved to be reliable only when the granules were perfectly spherical since any non-spherical granules would still have kinetic energy even after the collision if they were colliding at an angle due to bending of the granules. As for the other two methods, the decision was less straightforward.

The points in time when the maximum force or maximum strain are achieved are always very

close to each other. However, the moment the strain reaches a maximum tends to be consistently closer to when the kinetic energy is at a minimum (in the case of spheres) throughout the strain range tested. Therefore the maximum deformation reached during contact was selected as the simulation endpoint for consistency. Figure 4.5 illustrates the different simulation endpoint candidates plotted against time when two identical perfect spherocylinders come into contact at a 90° angle. It should be noted that the seemingly non-conservative nature observed in Figure 4.5, where the second peak of kinetic energy does not reach as high as the first, is due to a significant amount of internal energy in the system at that point, as indicated by the strain curve. Since the collision involves two rods colliding perpendicularly, there is still a significant amount of bending within each granule when they separate.

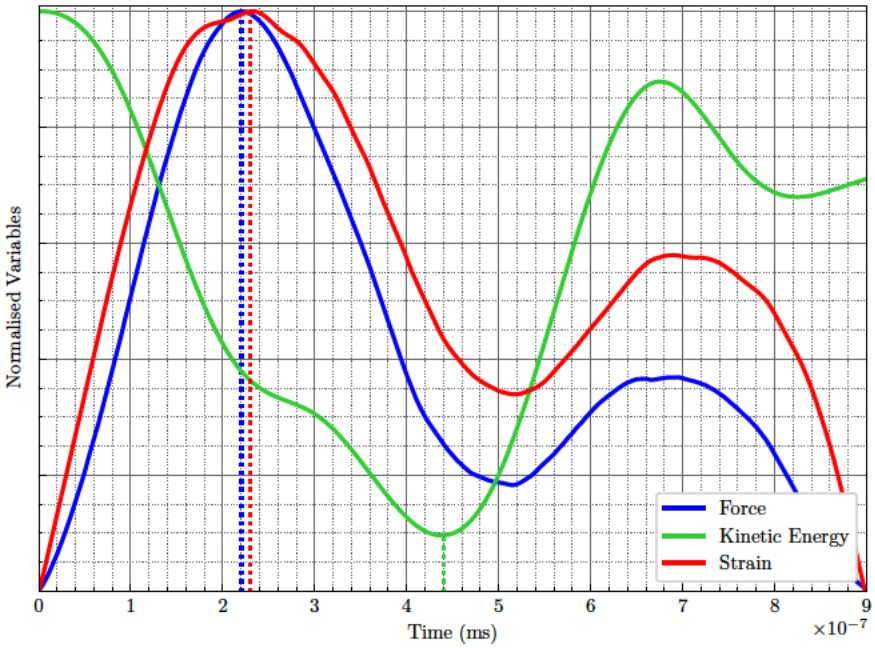

Figure 4.5: Metrics comparison for defining the simulation endpoint used for the kinematic collisions in Abaqus. The moments where each candidate endpoint is reached for the different variables tested are noted with a dotted line. The case shown is that of perfect spherocylinders coming into contact at a 90° angle.

Therefore the data obtained at the designated simulation endpoints were the reaction force (as described in Abaqus) and the deformation applied on each granule during the collision. The reaction force on the bottom granule was straightforward to obtain directly from Abaqus, whereas the deformation needed some additional processing. A set of two central nodes was created on every granule (shown in Figure 4.4), one at the very top and one at the very bottom. The distance between the position of the two nodes at the granules' original state was compared to the distance between the two nodes at the simulation endpoint. The deformation applied on the granule is defined as the difference between the two distances measured. The strain is then obtained by dividing the deformation applied on the granule with its diameter, as defined in

Equation 3.1.

The final force–strain curve for each configuration was assembled by plotting the data obtained at the endpoints of each simulation, producing curves similar to those in Figure C.1 in Appendix C. The process was then repeated for different angles θ. The angles chosen were 30°, 45°, 60° and 90°. For the parallel contacts however, where $\theta = 0°$, a different procedure was followed.

4.1.2 Parallel Contacts: Quasi-static Compressions

For parallel contacts, the simulations were performed under quasi-static conditions instead. Following a quasi-static approach inherently negates any inertial effects by definition. This eliminates the need for additional parametric studies, thus simplifying the process. However, it could not be used for all the configurations tested, only for the parallel contacts and most simulations involving spherical granules (special multi-spherical rod cases with the consisting spheres having a 100% overlap between them).

As stated in Chapter 3, the Abaqus assembly for the quasi-static simulations consisted of a single granule being compressed between two rigid flat plates. It was determined that all configurations which could be modelled under quasi-static conditions were also symmetrical. Therefore symmetry planes were used to minimise computation times, leaving an assembly consisting only of an octant of the granule similar to what is shown in Figure 3.3.

Additionally, the data extraction with these simulations was also simplified as both the force and deformation can be obtained directly from Abaqus. The deformation applied can be taken from the distance the rigid plates have travelled in order to compress the granule, while the force can be obtained from the reaction force acting on the rigid plates when they compress the granule. Strain as defined in Equation 3.1 is used to represent a unitless measure of deformation.

4.2 Contact Model Errors – Fixed-Sphere Rods (FSR) with changing sphere overlaps

In order to quantify the error caused by the contact model used in DEM, a comparison was made between the forces obtained from a collision between two MS rods in an FEM setting and a DEM setting using various different contact models. That was accomplished by first fixing the number of spheres for all the different configurations examined. The main changing parameter for the parametric study conducted was the amount of overlap (based on distance) between the constituent spheres of the MS rods. Although initially the number of spheres in the MS rods was fixed to 2, it was soon changed to 3 in order to easily accommodate the angled collision simulations performed. The three-sphere rod configurations used are shown in Table 4.1.

Table 4.1: Three-Sphere Rod configurations

Sphere overlap	Three-sphere rod
0% overlap	
10% overlap	
20% overlap	
30% overlap	
40% overlap	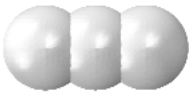
50% overlap	
60% overlap	
70% overlap	
80% overlap	
90% overlap	
100% overlap	

4.2.1 Preliminary Study: Parallel contact of two-sphere rods

Starting with the parallel contact of two-sphere rods, a parametric study was conducted by uniaxially compressing the two-sphere rods as previously explained. The main variable was the sphere overlaps of the MS rods based on distance as defined in Equation 4.1:

$$\text{Sphere Overlap} = \frac{2R - L}{2R} \times 100\% \tag{4.1}$$

with $2R$ being the diameter of the constituent spheres and L being the distance between their centers. An overlap of 0% corresponds to two spheres (within a MS rod) in touching contact, whereas an overlap of 100% would correspond to both spheres occupying the same space, represented as a single sphere in FEM. Since all spheres in a rod had the same radius, it can be redefined as shown in Equation 4.2:

$$\text{Sphere Overlap} = \frac{N_{\text{spheres}} - \text{Rod Aspect Ratio}}{N_{\text{spheres}} - 1} \times 100\% \tag{4.2}$$

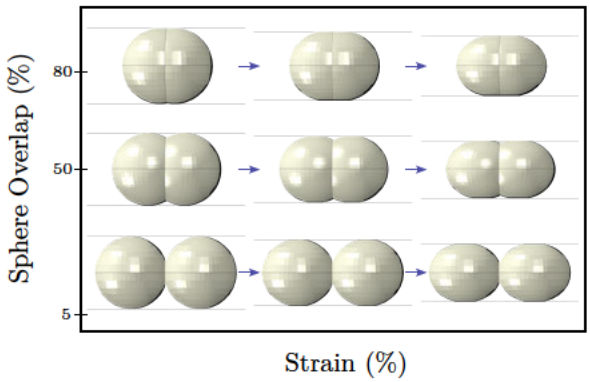

Figure 4.6: Schematic representation of various two-sphere rod configurations based on spatial location within the contour plot. The configurations shown have 5 %, 50 % and 80 % sphere overlaps throughout the different stages of compression. Deformations have been exaggerated to enhance clarity of representation.

The parametric study consisted of 21 quasi-static compression simulations of two-sphere rods with sphere overlaps ranging from 0–100%. The two-sphere rods were compressed along their length. There are about 200 data points obtained from each simulation which are distributed along the strain axis.

The results of the parametric study are summarised in the contour plots in Figure 4.7, presented along with a schematic (Figure 4.6) of a number of two-sphere rod configurations for visual aid. The x-axis indicates the axial strain applied on the two-sphere rods, while the y-axis indicates the percentage sphere overlap within the two-sphere rods based on distance. The contours indicate the relative errors between the FEA results and the DEM contact models according to Equation 4.3:

$$\text{Error} = \frac{F_{\text{CM}} - F_{\text{FEA}}}{F_{\text{FEA}}} \times 100\% \tag{4.3}$$

The FEA is taken as the basis for the relative errors; therefore a positive error is when the contact model is overpredicting the normal contact force and a negative error is when the Contact Model (CM) is underpredicting the normal contact force.

The contour plots were constructed using Matplotlib's (Hunter, 2007) `tricontourf` command.

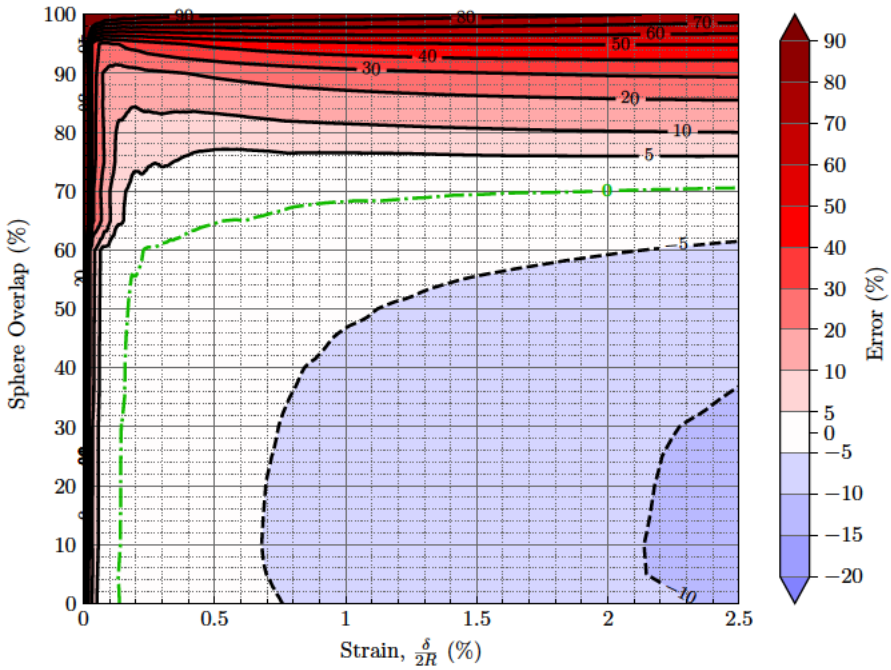

(a) Two-sphere rod parallel contact – Hertz

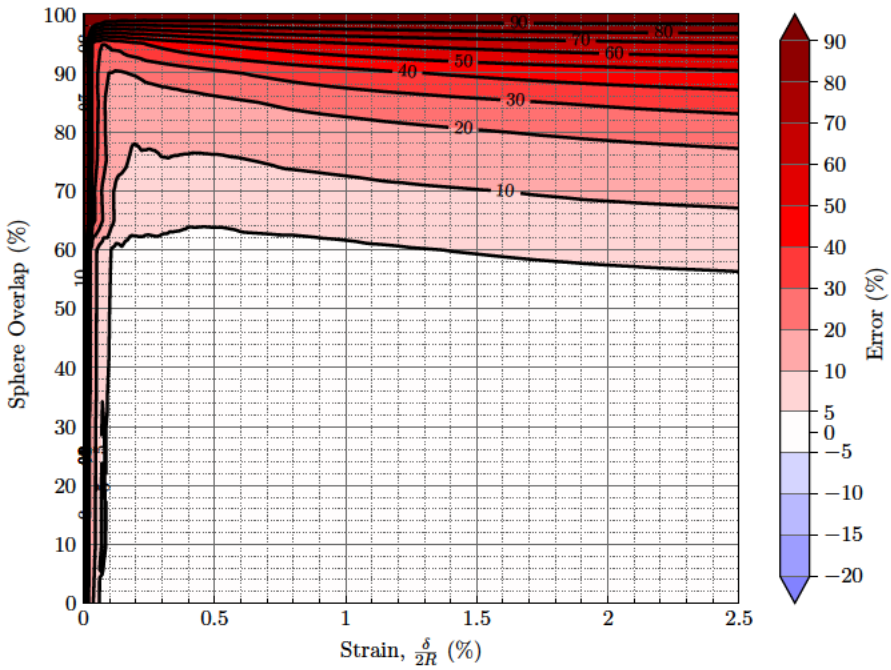

(b) Two-sphere rod parallel contact – Tatara

Figure 4.7: Comparison of the force response of a two-sphere rod at various sphere overlaps obtained through the FEA against the one obtained through (a) the Hertzian contact model and (b) Tatara's contact model. The contours are indicating the relative errors present, while the signs of the errors represent whether the contact models are overpredicting (positive error) or underpredicting (negative error) the contact force based on the FEA results.

The command internally takes care of the triangulation necessary for any contour plots with datapoints which are not perfectly aligned on a grid. While this is not necessary for the quasi-static compression cases, the kinematic collisions are not always perfectly aligned as is further explained in Section 4.3.1.

Focusing on the comparison with Hertz from Figure 4.7a, for the rods with a sphere overlap less than 70%, Hertz generally underpredicts the contact force applied. At low deformations up to about 0.75% strain Hertz has a good agreement with the FEA results. The relative errors remain less than 5%. As the strain increases, the deviation between the FEA model and Hertz force increases monotonically in magnitude. As for the rods with a sphere overlap greater than 70%, Hertz overpredicts the normal contact forces. However, the strain ceases to be the main factor and instead the sphere overlap becomes the main driver of this deviation. As a result of this dependency change, the two-sphere rod with a sphere overlap of 70% shows a very good agreement with the Hertzian contact model even at high strains.

In the comparison with Tatara's CM in Figure 4.7b, increasing the strain does not appear to significantly affect the errors in the contour plot. The sphere overlaps have a slightly more prominent effect when compared with the Hertzian comparison. It can be seen that the 5% error bound starts at sphere overlaps of about 65% rather than at 75% but both plots roughly follow the same pattern at greater overlaps. The main difference though between the two CM is that at the lower sphere overlaps, Tatara's CM has a really good agreement with the FEA results, irrespective of how much strain is applied.

4.2.2 Three-sphere rod contacts

Considering the fact that there was a need for testing the force responses of these collisions at various angles, the focus was shifted from two-sphere rods to three-sphere rods. This allowed for a consistent point of contact on the middle sphere of the rods irrespective of the angle chosen for the collision. The alternative would require a need to consider how to handle the collisions taking place in the interspherical gap of the rods. That intrinsically would entail the tangential forces having an influence on the contact force obtained while also introducing great inconsistencies at the point of contact, both due to the varying sphere overlaps in addition to the varying collision angles. Such collisions taking place in the interspherical gap of the rods cause the contacting particles to interlock, which adds additional unnecessary complexity in the system considering it is not a focal point.

The three-sphere rod simulations were set up in a very similar way. For the parametric study, the overlap of the spheres was changing based on distance, again ranging from 0% to 100%. This was accomplished by fixing the position of the middle sphere and repositioning the adjacent spheres accordingly. The results for the parallel contact of the three-sphere rods are summarised in the contour plots in Figures 4.8a and 4.8b, where they are compared with Hertz and Tatara's contact models respectively. It should be noted that the colourmap scale used for the two-sphere

rod errors is different compared to the one used for the three-sphere rod errors in the contour plots.

The main difference between the two-sphere rod and the three-sphere rod error plots is the scale of the errors at higher sphere overlaps. The three-sphere rods seem to follow a very similar trend when it comes to increasing strains. Taking the comparison with Hertz first, at sphere overlaps less than 65%, strain is the main driving force for the deviation but that changes once the 65% sphere overlap was reached. Consequently, due to the large sphere overlaps the error becomes rapidly greater with the Hertzian contact model overpredicting the force response. As there are now 3 constituent spheres, at greater overlaps this error increases at substantially greater rates compared to the two-sphere case. Similarly, while the strain does not seem to affect the errors in the Tatara comparison, at sphere overlaps beyond 55% the errors become larger at a greater rate compared to the two-sphere case.

Angled collisions of three-sphere rods As for the kinematic angled collisions that will be covered in the following sections, the process was more complex. As outlined in Section 4.1.1 in order to minimise the inertial effects, for each sphere overlap case an additional parametric study had to be conducted. Out of those simulations, only the data from the endpoint of each kinematic simulation was used for the contour plots. Therefore, the force–strain data from the FEA was only obtained every 0.5% of strain. As for the sphere overlaps, eleven of these parametric study campaigns were run for every 10% increment of spherical overlaps within the rods. This gives a total of 11 rod configurations which were each tested at 10 different strains (11 counting the no-strain data points which were set to zero). This process was repeated for all angles tested which totals to 411 FEM simulations (ignoring some recurring cases). Since the data used for these contour plots is more sparse, these points were also shown in the relevant contour plots. Moreover, due to the sparsity of the data in the kinematic collisions, the contour lines appear much more jagged in comparison to the contour lines in the parallel contact plots. In the following sections the three-sphere rod FEA will be compared with the various different contact models used in DEM.

Furthermore, it is important to note that the positive errors at high sphere overlaps in all angled three-sphere error contour plots (particle–particle collisions) reach values beyond 640%. The greatest error recorded with Hertz is around 700%. Although higher than expected, considering how DEM works and that this occurs when the spheres are almost completely overlapping, it seems logical. The reason being that at such high overlaps, in a DEM setting, each sphere within one rod is interacting with every sphere of the other rod having a total of 9 different interactions constituting the total contact force and hence causing such a massive overprediction.

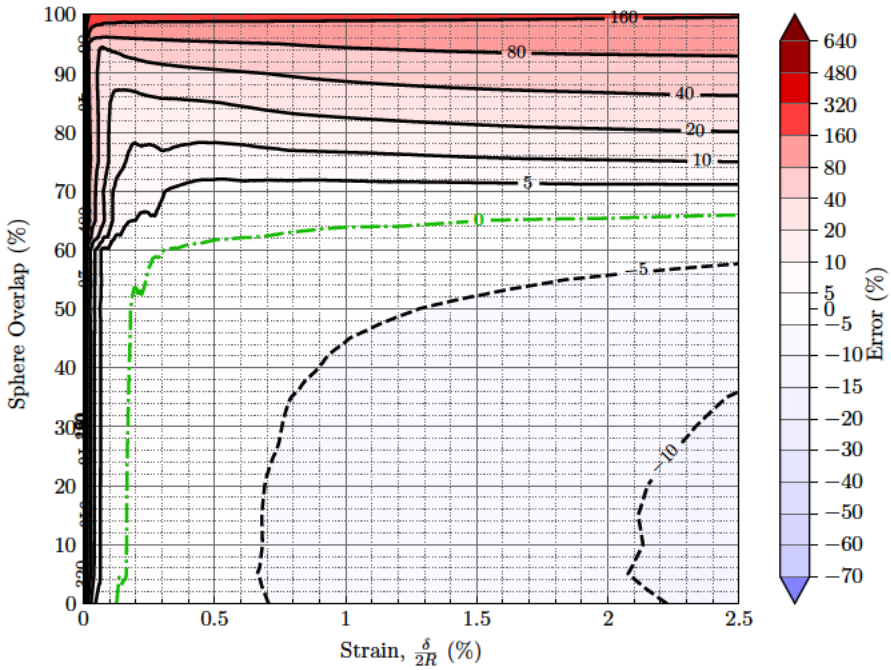

(a) Three-sphere parallel contact – Hertz

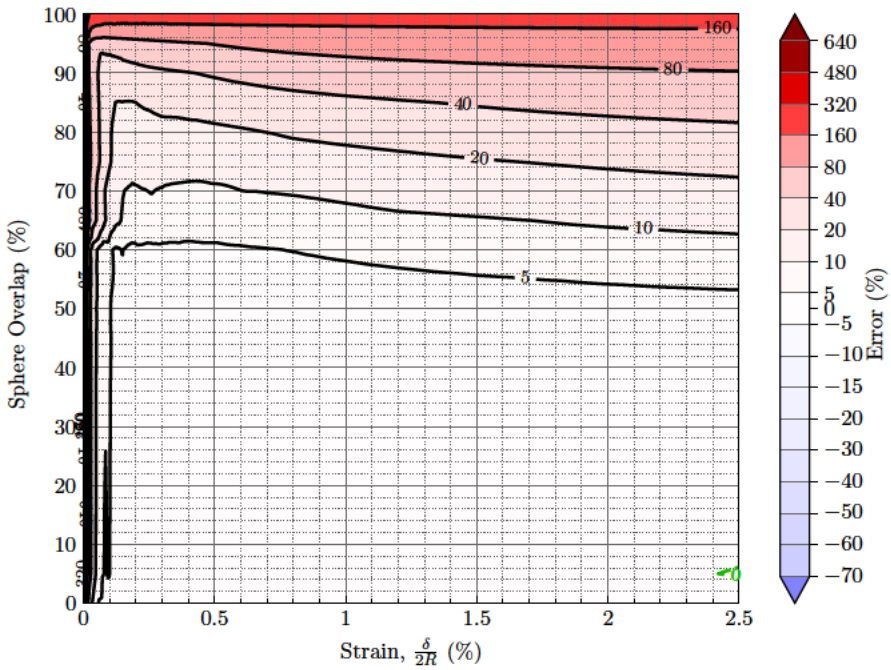

(b) Three-sphere parallel contact – Tatara

Figure 4.8: Comparison of the force response of a three-sphere rod at various sphere overlaps obtained through the FEA against the one obtained through (a) the Hertzian contact model and (b) Tatara's contact model. The contours are indicating the relative errors present, while the signs of the errors represent whether the contact models are overpredicting (positive error) or underpredicting (negative error) the contact force based on the FEA results.

4.2.2.1 Hertz model multi-spherical error evaluation

Focusing initially on the comparison between the parallel contacts presented in Figure 4.8a and the angled collisions presented in Figure 4.9, the 0% contour line — represented with a green dash-dotted line — does not cross the strain axis in any of the angled collisions. This is simply because of the difference in the resolution between the parallel contact plots and the angled collision plots. In the parallel contact case the 0% contour line becomes vertical at around 0.12% strain, however the first data points in all the kinematic collision plots have a strain of around 0.5%. This results in the 0% contour line to split all the angled collision contours, starting at around 80–90% sphere overlap and finishing at about 55% sphere overlap when following a path of ascending strain values.

Additionally, for the portion of the plots below the green contour line — where the negative errors occur — all the contour lines seem to have receded with respect to strain, except for the 30° case which will be discussed below. This indicates a less prominent underprediction of the force response at higher strains, which is most probably because the contact in each case was focused on the central sphere rather than the entire length of the rod. Furthermore, as the angle of the collisions increases it is noted that the white region — around the 0% contour line — gets narrower, hinting at the contact model's decreasing suitability at higher strains. As for the portion of the plots above the green contour line — where the positive errors occur — all plots follow a very similar pattern. The errors are mainly driven by the increasing spherical overlaps within the MS rods themselves rather than strain. The comparison for the angled collisions of the MS rods will be performed in ascending order of angles:

30° contour plot (Figure 4.9a) The contour plot for the 30° collision is the one that deviates the most from the rest of the plots. Additional contour lines of −15 %, −20 % and −30 % appear at higher strains below 50% sphere overlap. While still following the general trends of the receding contour lines in terms of strains, this only holds true at the lowest sphere overlaps, below 20%. At up to around 55% sphere overlap, the contour lines are greatly advancing to the point where the −10% contour line is present at strains as low as 1.6%. The reason behind this change can be attributed to the fact that as the granules collide at a 30° angle the contact is not confined just to the central sphere at higher strains: it expands to the sides of the rods, thus causing the underprediction indicated (refer to schematic in Figure 4.10). The point within the plotted error contours that signifies the force that was underpredicted the most by Hertz was at 5% strain with a sphere overlap of 20%. The error at that point reached a value of −37%. That is the largest underprediction out of all the error contour plots by far when comparing with the analytical solution by Hertz.

45° contour plot (Figure 4.9b) At the 45° contour plot the contour lines below the 0% contour line recede more uniformly with respect to strain. The only additional contour line compared to the parallel contact case is the one signifying a −15% error, which is mainly confined

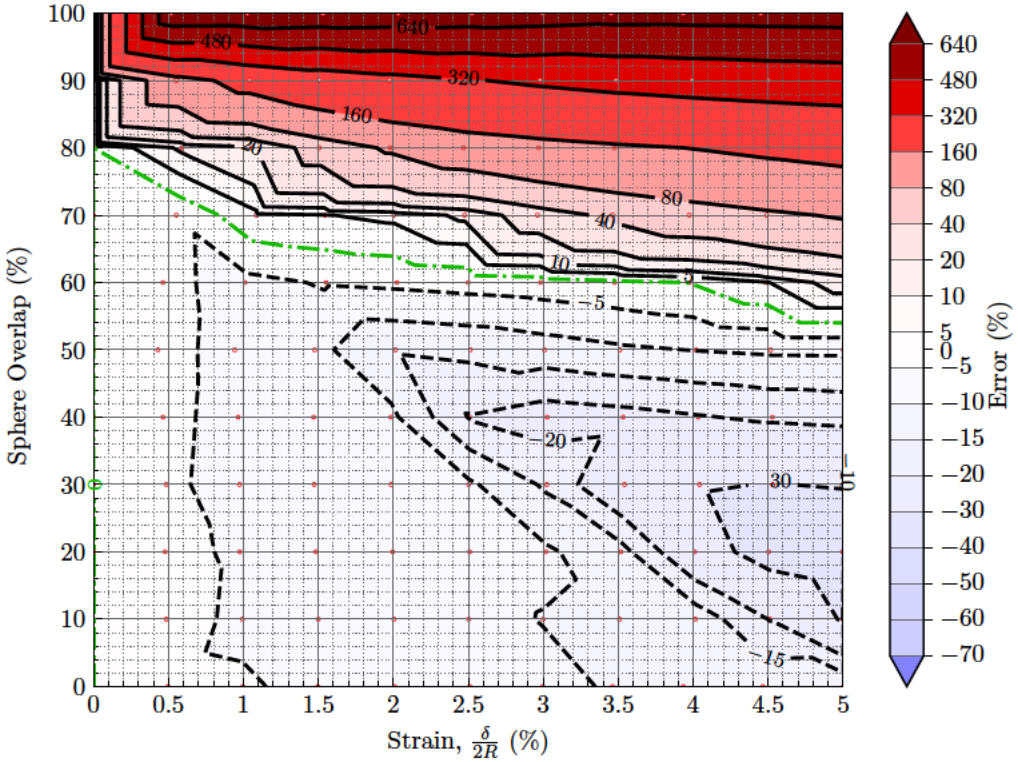

(a) 30° collision comparison with Hertz

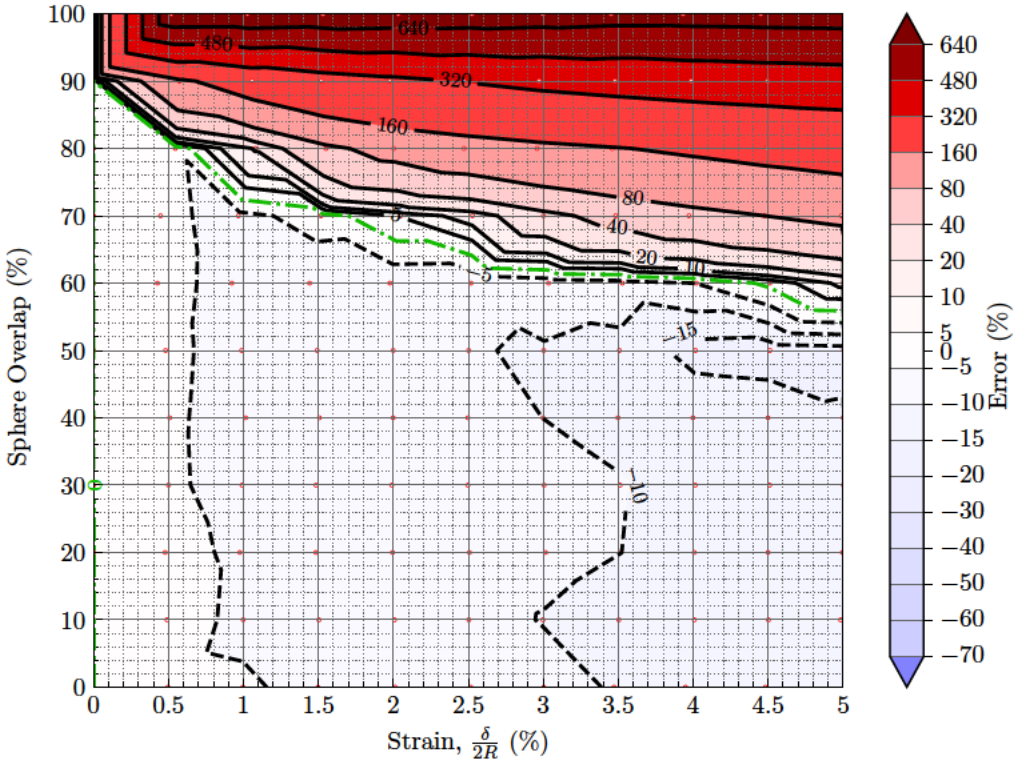

(b) 45° collision comparison with Hertz

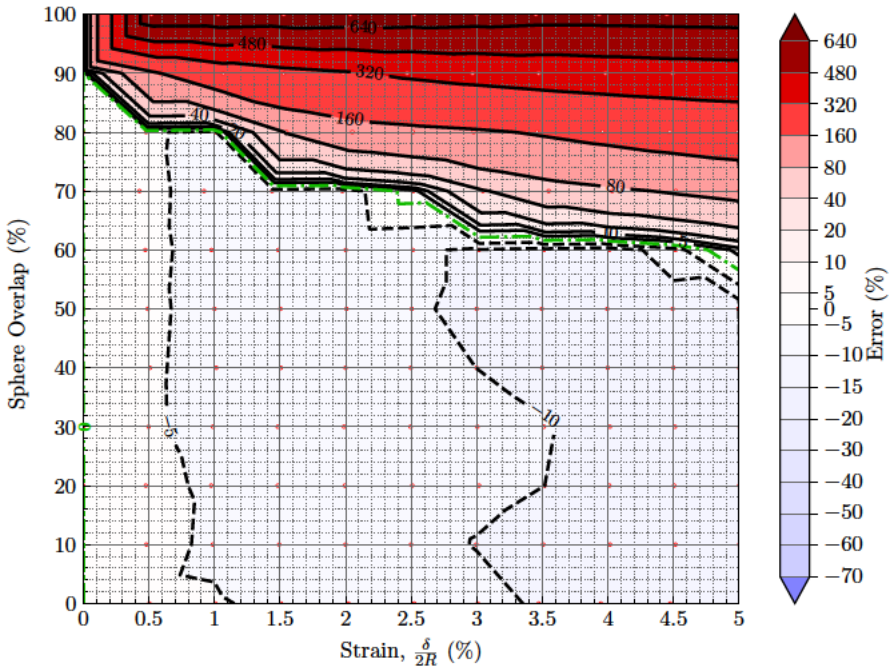

(c) 60° collision comparison with Hertz

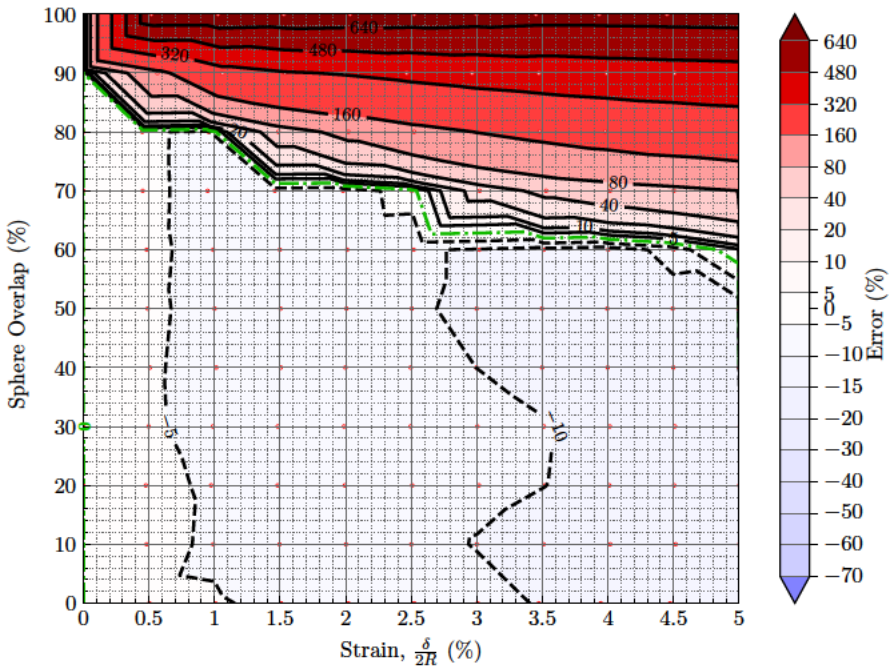

(d) 90° collision comparison with Hertz

Figure 4.9: Contour plots showing the error bounds between the force responses of the MS rods in the FEA and the Hertzian contact model at the various angles. The positive errors in red indicate the configurations where the contact model overestimates the force response and the negative errors in blue indicate an underestimation of the force response when compared to that of the Finite Element model.

to a small area at strains beyond 4% and sphere overlaps around 40–50%. This indicates that the side contact has less of an influence at the 45° angle collision.

60° contour plot (Figure 4.9c) & 90° contour plot (Figure 4.9d) The contour plots at 60° and 90° are marginally different from one another and only have two noticeable changes compared to the one at 45°. The first change is the complete disappearance of the −15% contour line within the strain region tested. This is an indication that at these angles the side contact no longer occurs at the low sphere overlap region. The second change is the shift of the −10% contour line higher up, narrowing the gap between that and the −5% contour line. This makes the change in sphere overlap much more dramatic at higher strains, most probably because at those angles the contact resembles more the contact between two spheres.

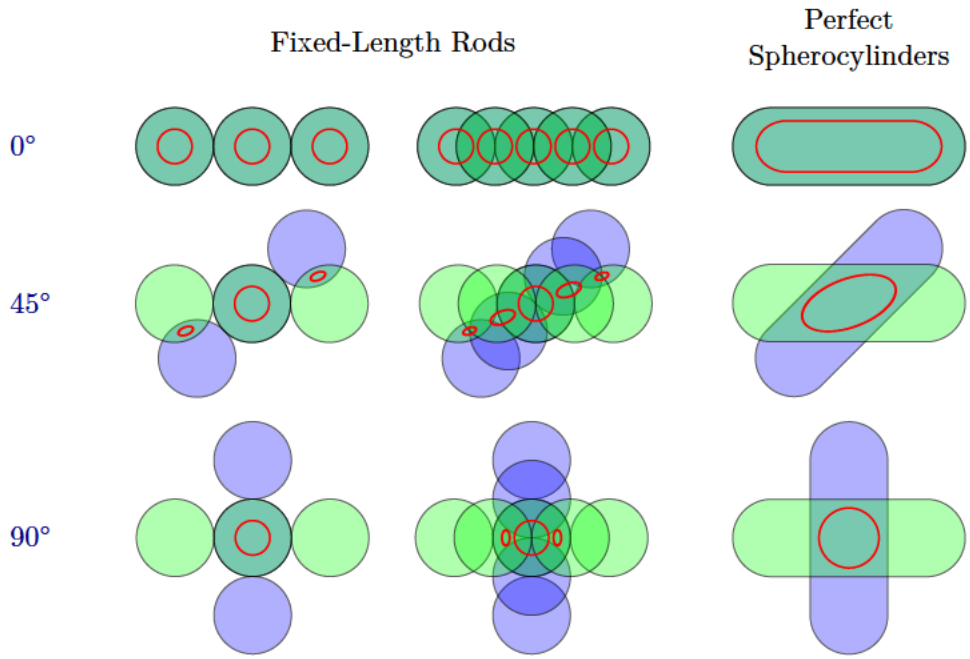

Figure 4.10: Schematic of contact areas (highlighted in red) of multi-spherical rods and spherocylinders in contact as seen from above.

4.2.2.2 Tatara model multi-spherical error evaluation

Focusing initially on the comparison between the parallel contacts presented in Figure 4.8b and the angled collisions presented in Figure 4.11, strain seems to have more of an impact in the angled collisions. This is demonstrated by most positive contour lines which are no longer parallel to the x-axis in the angled collisions as well as the additional contour lines that appear even at low sphere overlaps. The 5% contour line for example only wavers around 55–60% sphere overlaps in the parallel contacts, whereas in most angled collisions even contour lines up to 20% errors cross through all sphere overlaps.

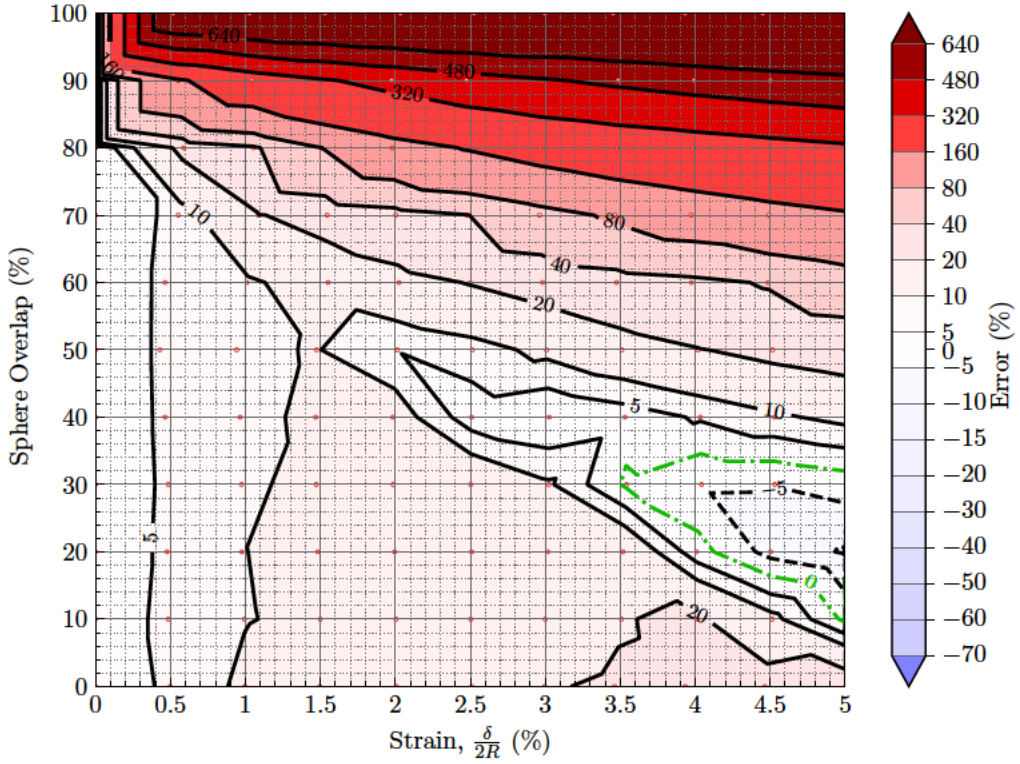

(a) 30° collision comparison with Tatara

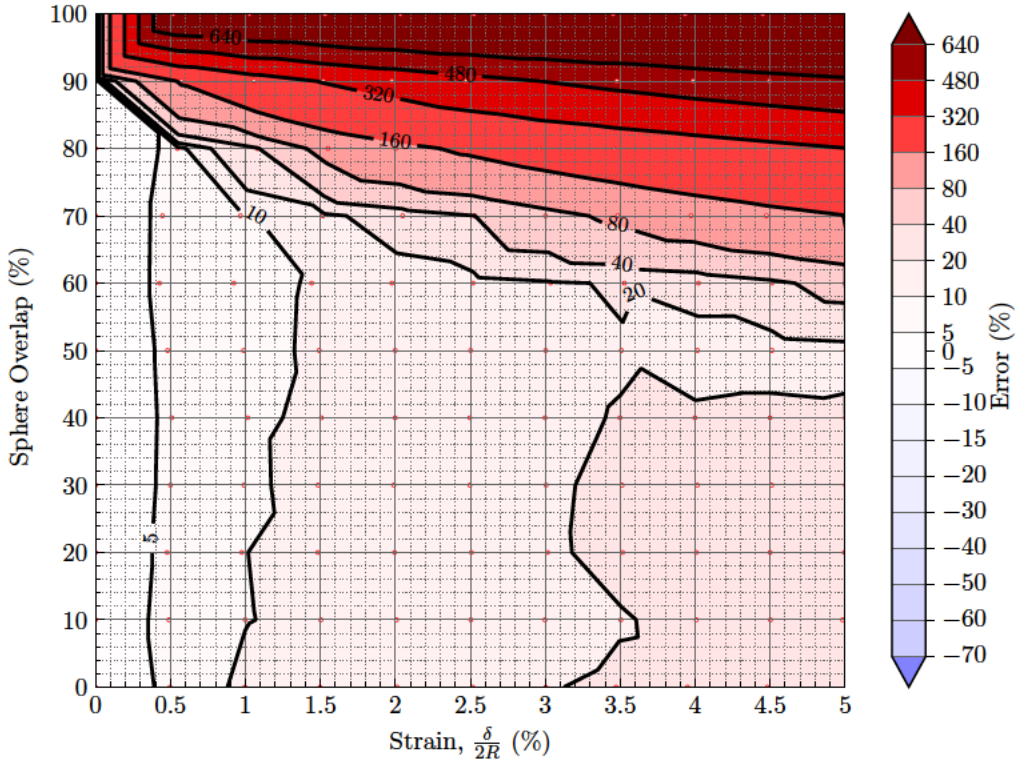

(b) 45° collision comparison with Tatara

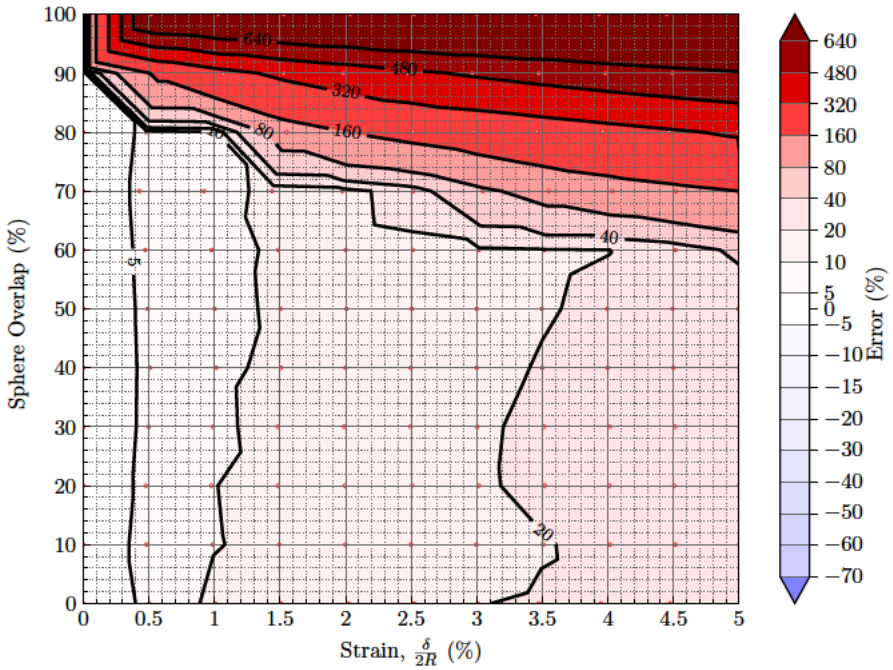

(c) 60° collision comparison with Tatara

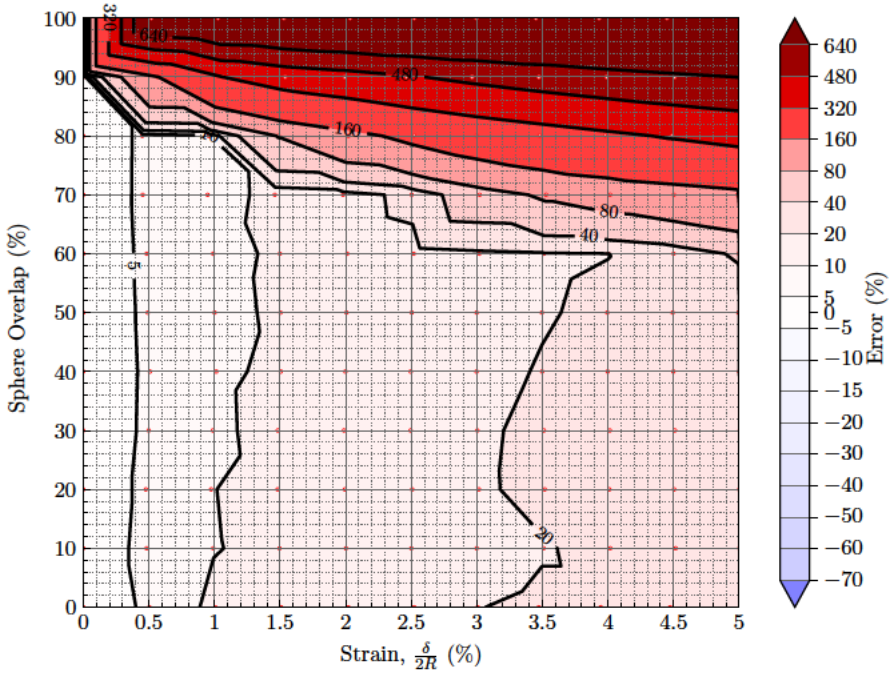

(d) 90° collision comparison with Tatara

Figure 4.11: Contour plots showing the error bounds between the force responses of the MS rods in the FEA and Tatara's contact model at the various angles. The positive errors in red indicate the configurations where the contact model overestimates the force response and the negative errors in blue indicate an underestimation of the force response when compared to that of the Finite Element model.

30° contour plot (Figure 4.11a) Similar to the Hertz error contours, the 30° contour plot seems to be the most interesting compared to the other plots in Figure 4.11. Additionally, it is the only contour plot when comparing with Tatara's analytical solution that negative error contour lines appear in. The contour lines of the two 30° contour plots also follow very similar trends. The main difference between them is that, since Tatara's contact model typically predicts higher forces, the contour lines present in Tatara's comparison are generally about 20% higher compared to the relevant Hertz contour lines. This is more obvious at high strains and low sphere overlap rod configurations, where the contour lines are almost identical to those appearing in the relative relevant contour plot with Hertz (Figure 4.9a). The 10%, 5%, 0% and −5% contour lines in the Tatara comparison take the place of the −10%, −15%, −20% and −30% contour lines respectively in the Hertz comparison. The greatest underprediction is happening again at the MS rod with 20% sphere overlaps at the maximum strain just like in the comparison with Hertz. The error at that point is −10%. Just like with the Hertz contour plots, the reason for these underpredictions can be attributed to the occurrence of that side contact in the rods (schematic shown in Figure 4.10).

45° contour plot (Figure 4.11b) At the 45° contour plot all the negative error contour lines disappear from the tested strain region and even the positive error contour lines recede. There is however a region created by the 20% contour line at sphere overlaps around 45–50% and strains beyond 3.5%, which can yet again be attributed to the side contact of the rods.

60° contour plot (Figure 4.11c) & 90° contour plot (Figure 4.11d) Just like the Hertz contour plots, the contour plots at 60° and 90° are almost identical and only have two noticeable differences compared to the one at 45°. The greater one is the disappearance of the region created by the 20% contour line as the prominence of the side contact shifts to higher spherical overlaps and the minor difference being the receding of the positive error contour lines even higher up and towards the right of the plot.

Further discussion on Hertz and Tatara The greatest underprediction in both cases seems to be taking place at the exact same rod configurations at the maximum strains tested. For the contacts taking place at up to 45°, the configuration at which the side contact is most prominent can be located using the previously mentioned points for both comparisons. At a 30° angle that seems to be at a spherical overlap of 20% and at a 45° angle, that is around a 50% sphere overlap. Additionally, it can be seen that the positive error contour lines — located at the higher sphere overlaps — start receding as the angle of the contacts increases. That is probably due to the contact increasingly resembling that between two individual spheres.

What seems to be consistent with all contact models and collision angles evaluated is that when sphere overlaps surpass the 60-70% mark, the change in sphere overlap becomes the dominant factor driving the errors, as opposed to the strain applied. Rod configurations with

greater sphere overlaps should therefore be avoided when using spherical contact models for non-spherical particles.

Additional contact model comparisons

Two further contact models were tested; the linear contact model and the Advanced Multi-Sphere Method as implemented in Aspherix. Additional contact models involving correction parameters for Hertz were not included as they only seem to work up to the strains they have been calibrated for.

4.2.2.3 Linear (Hooke) model multi-spherical error evaluation

An evaluation of the contact model errors present when using the Linear contact model was also performed due to its popularity. The same approach was taken as in Sections 4.2.2.1 and 4.2.2.2 and the results are presented below, starting with the parallel contact in Figure 4.12.

The Linear contact model is given by Equation 2.8 but the constant k is arbitrarily selected. It is usually selected so that the resulting force F matches a target force at a specific deformation δ. Therefore, in this case it was set as $k = 16.8 \times 10^4$ so that, at the parallel contact of the three-sphere rods with 0% sphere overlap, the force was equivalent to the FEA force at a strain of 1.25%. The chosen strain was selected as a representative value to better showcase how the Linear contact model compares against the FEA forces. The selected k value was used for all angles to keep the results consistent.

Unlike the previous contact models tested, there is not a single large region in which the Linear contact model can accurately predict the normal contact force. That holds true even at low spherical overlaps and low strains, as can be seen from Figures 4.12 and 4.13. That is entirely dependent on how the normal contact stiffness k is calibrated.

The selection of the k value is the single determining factor of how the contour lines are placed on the plot. Since it can be arbitrarily selected, the green zero percent contour line can shift more towards the left or to the right of the plot. Thus, the force obtained from the linear contact model can match the FEA force at lower or higher strains respectively.

Parallel contact contour plot (Figure 4.12) In the parallel contact case, strain is the driver of the errors at spherical overlaps below roughly 70%, with the errors monotonically decreasing as the strain applied decreases. Since the value of k is calibrated to a specific strain (1.25% in this case), the force from the Linear contact model matches the FEA force only at the region that is close to those strains, up to about 70% spherical overlaps in the rod.

For rods with higher sphere overlaps, strain no longer is the main cause of the errors and the sphere overlap takes over, similar to the contact models shown previously. The main difference is, once again due to the calibration of k, the overprediction at low strains in the high sphere

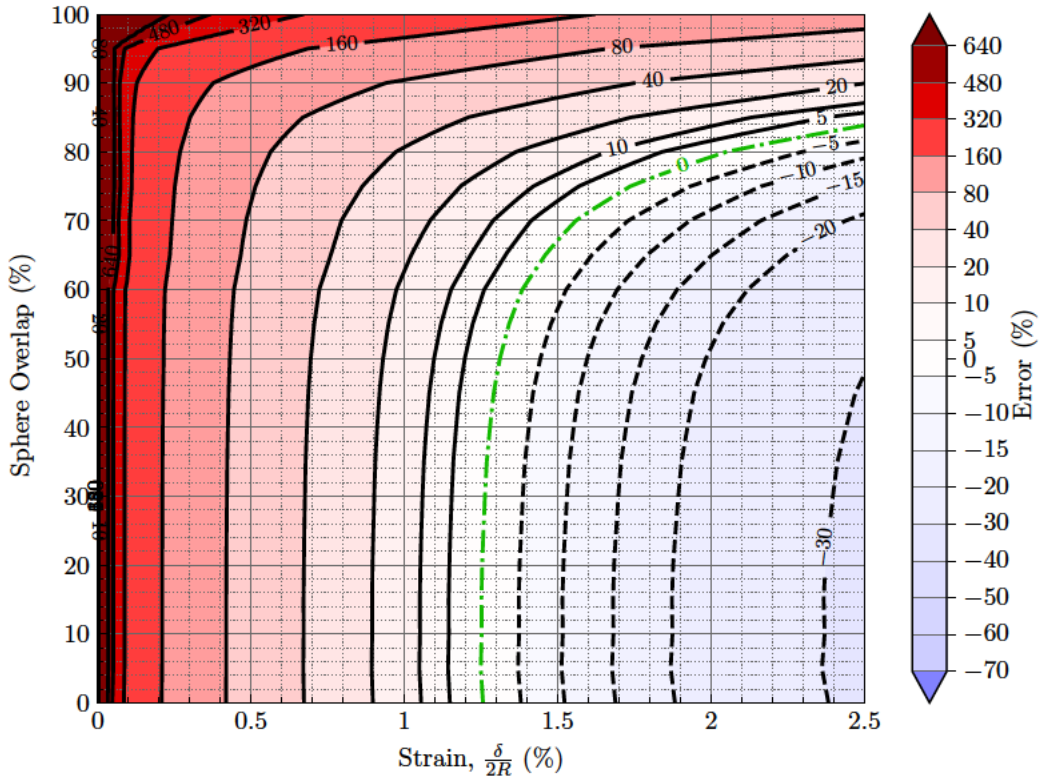

Figure 4.12: Comparison of the force response during parallel contact of a three-sphere rod at various sphere overlaps obtained through the FEA against the one obtained through the Linear contact model. The contours are indicating the relative errors present, while the signs of the errors represent whether the contact model is overpredicting (positive error) or underpredicting (negative error) the contact force based on the FEA results.

overlap region is up to 5 times larger compared to the one at higher strains. This is greatly affected by the fact that the relative error calculation is very sensitive to small strains.

Angled Collisions (Figures 4.13a–4.13d) As for the angled collision contour plots, they generally follow a very similar pattern. Additionally, just like the angled collision comparison with both Hertz and Tatara, the greatest underprediction within the tested configurations was at the 5% strain applied at the rods with 20% sphere overlaps.

Furthermore, at low strains there seems to be a discontinuity between strains of 0 and 0.5%. At these strains, the force is initially overpredicted before gradually being underpredicted by increasing the strain applied. That can be attributed to the lack of data since only 11 datapoints exist per rod configuration, leaving a large gap from 0 to 0.5% strain. This becomes more visible when k is calibrated for higher strains rather than the 1.25% strain selected for this study.

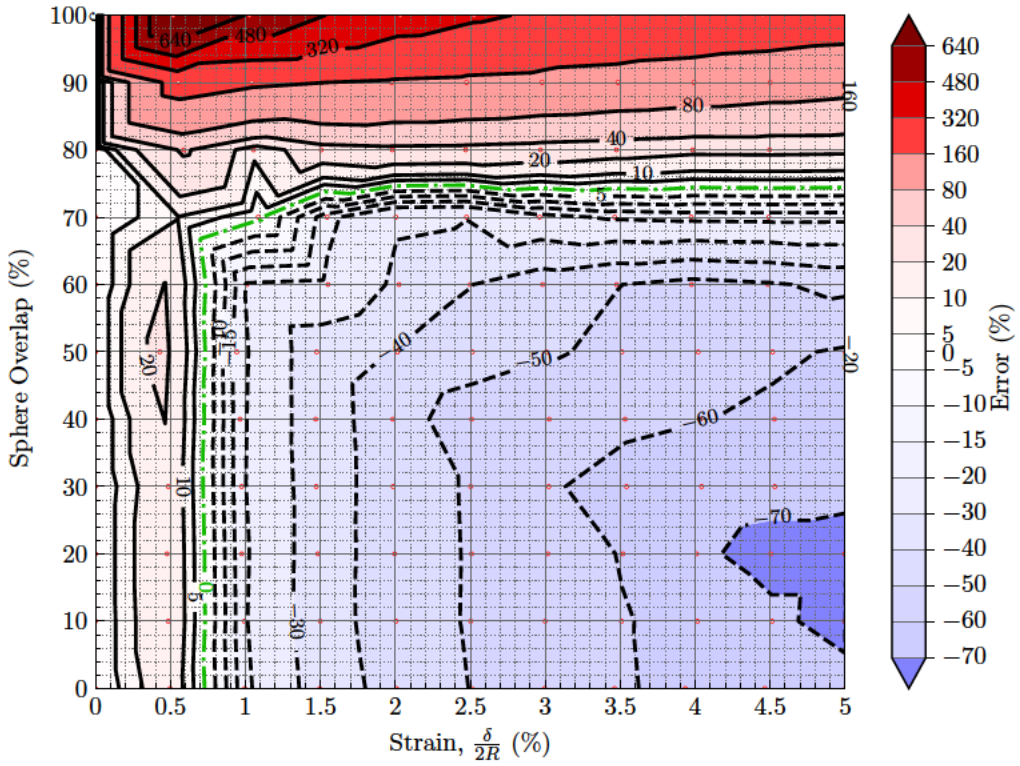

(a) 30° collision comparison with the Linear contact model

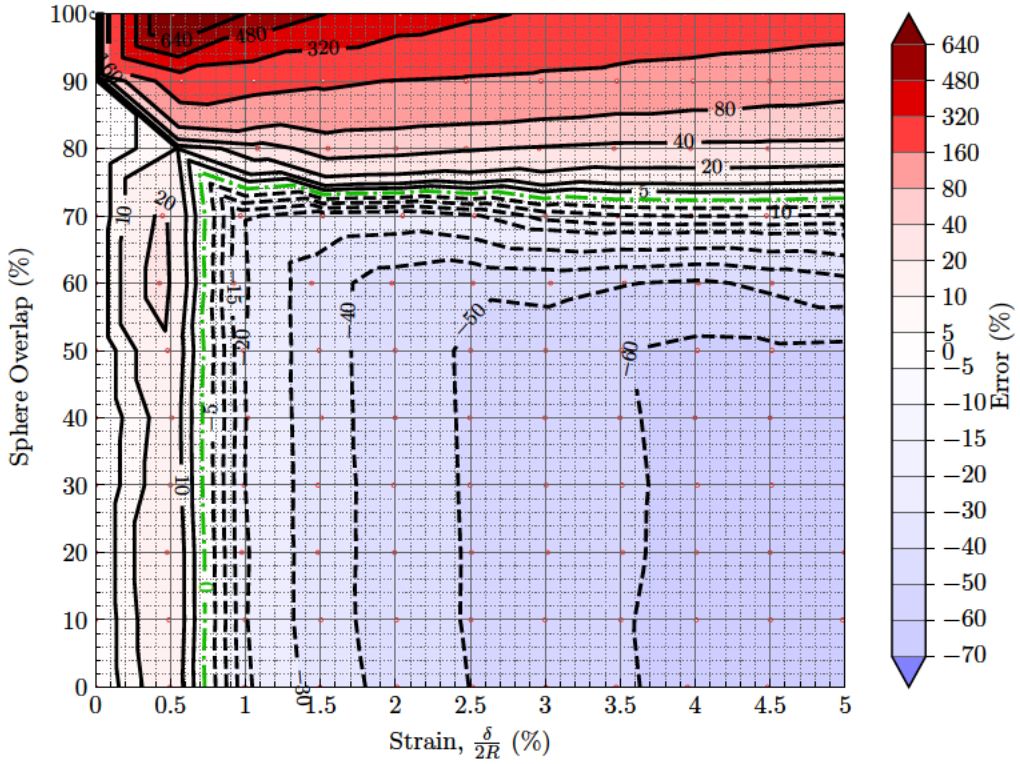

(b) 45° collision comparison with the Linear contact model

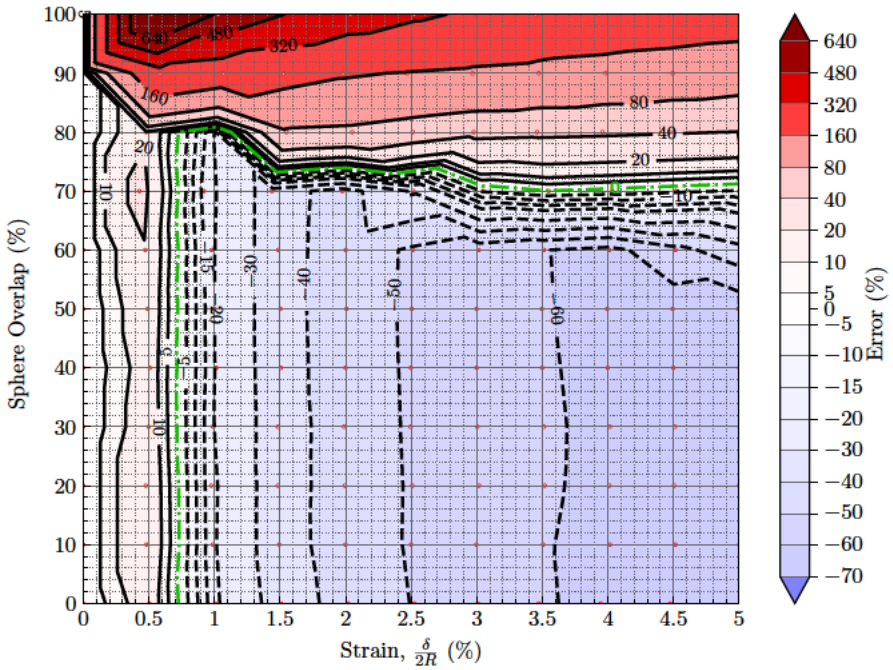

(c) 60° collision comparison with the Linear contact model

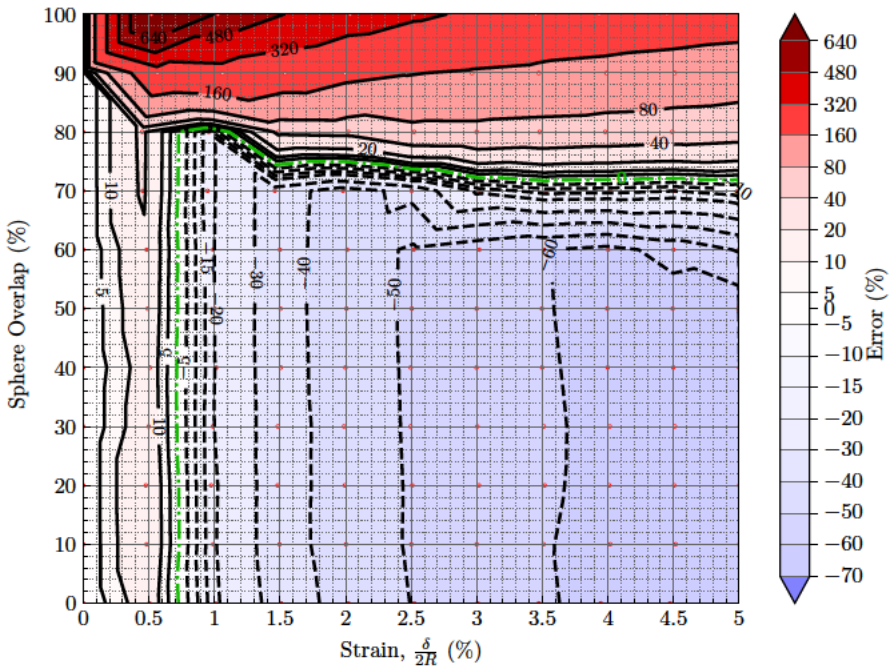

(d) 90° collision comparison with the Linear contact model

Figure 4.13: Contour plots showing the error bounds between the force responses of the MS rods in the FEA and the Linear contact model at the various angles. The positive errors in red indicate the configurations where the contact model overestimates the force response and the negative errors in blue indicate an underestimation of the force response when compared to that of the Finite Element model.

4.2.2.4 Aspherix Advanced Multi-Sphere Method

The method is implemented in the commercial DEM package Aspherix (DCS Computing, 2021) as a proposed partial solution to the Contact Model Errors being examined in this chapter. Therefore, it seemed appropriate to assess its performance. In order to do that, another PhD candidate (Oguzhan Erken) run a number of simulations in Aspherix identical to the kinematic collisions as specified in Section 4.1.1.

A total of five cases were tested for three-sphere rods coming into contact. Those were split in the parallel and perpendicular contact cases. For each type of contact three sphere overlaps were tested; 0% sphere overlap, 50% sphere overlap and the duplicate case of 100% sphere overlap. The force responses were compared against the FEM results and the Hertzian contact model since that is where it is based on. The results are presented in Figure 4.14. It is worth noting that since the parallel contact cases were run quasi-statically a larger number of datapoints are available from the FEM simulations as seen in Figure 4.14a. Furthermore, just like in the previous cases, the force responses for the parallel cases are only plotted up to 2.5% strain since there are two points of contact.

The Advanced Multi-Sphere Method seems to work using a form of an averaging algorithm. It is based on the Hertzian contact model, so the total force response obtained using Hertz is in a way divided by the number of spheres the MS rod consists of. Additional parameters are most probably included given that the Hertzian curve and the Advanced MS method curve do not line up when multiplied by three as seen in Figure 4.14, although they are consistently close throughout all plots with deviations of up to about 7.5%. However, given the large deviation from the FEM results as seen in the figures presented, the Advanced MS method cannot be recommended for use in MS DEM if the focus is to model accurate normal forces. It could perhaps be used for configurations with sphere overlaps beyond 70% although more testing is needed and it might work simply because of the averaging algorithm utilised. Hence, using the Hertzian model would be a more appropriate option.

4.2.2.5 Expanded Point of Contact regions

After the analysis was completed, it was determined that the designated 'point of contact' (PoC) region in the models where the mesh was more refined should perhaps be expanded to capture the side contact forces more accurately. Therefore the model was remeshed with a greater PoC region and an additional simulation was run. The radius of the sphere defining the size of the PoC region was changed from $0.3R$ to $0.7R$ as is shown in Figure 4.15 displaying the cross-section of the MS rod. As an indication of the impact this had on the mesh, the number of elements present in the remeshed model was approximately three times greater than the original model.

The configuration tested with the remeshed model was the 30° angled collision of the three-sphere rods with a 20% overlap when a 5% strain was applied. The specific configuration was selected as it was the point on the 30° angled collision contour plots (Figures 4.9a and 4.11a)

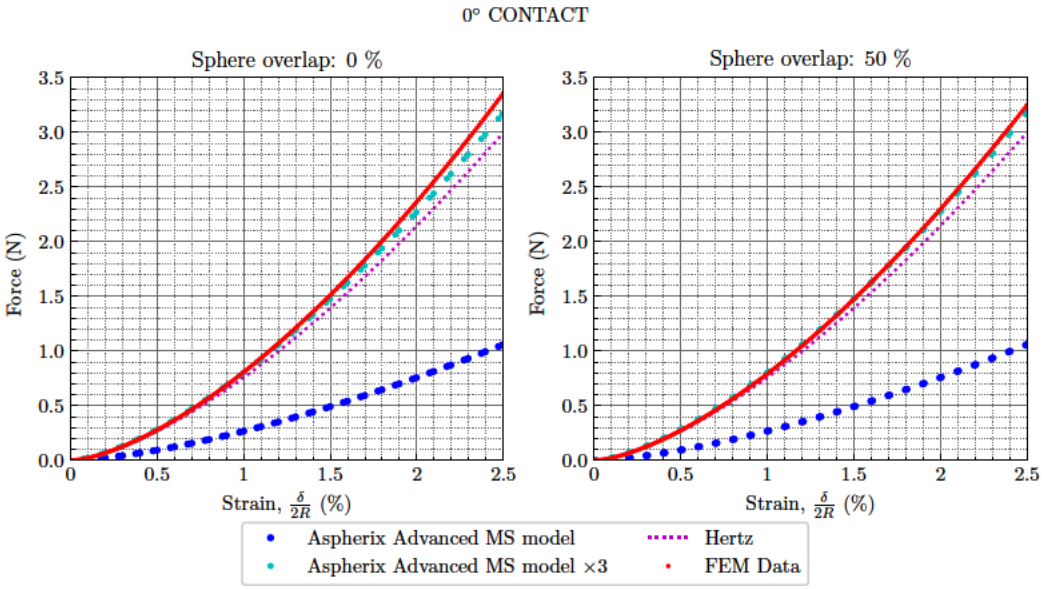

(a) Parallel rod contact.

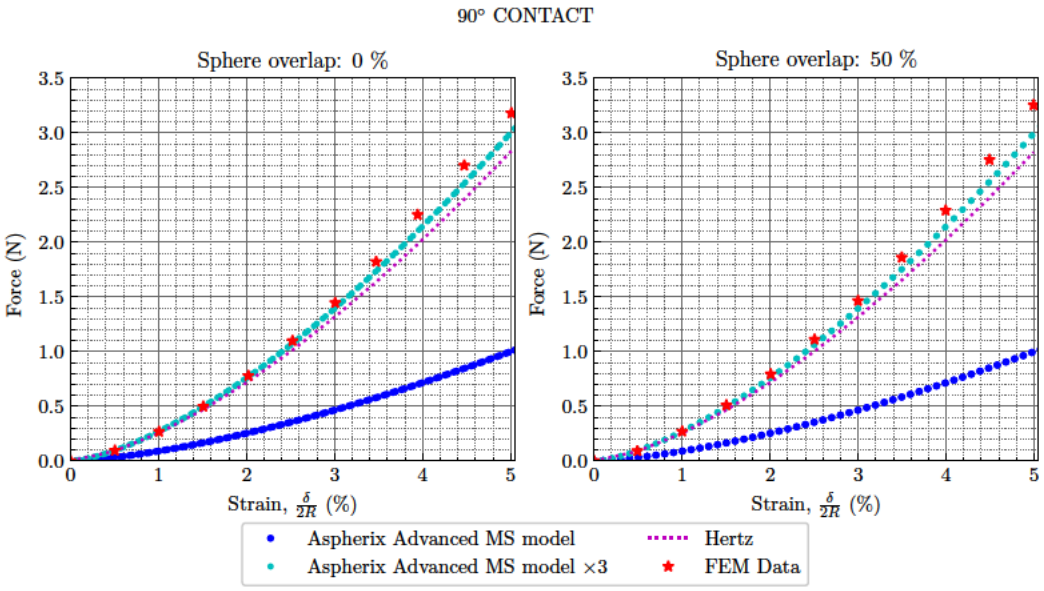

(b) Perpendicular rod contact.

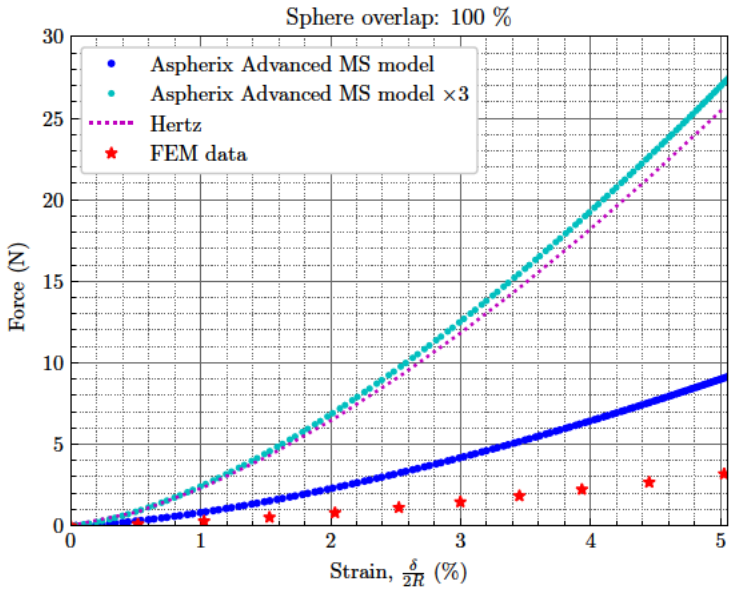

(c) Rod contact with 100% sphere overlap.

Figure 4.14: Aspherix Advanced Multi-Sphere Method comparison with FEM and Hertz in parallel and perpendicular three-sphere rod contacts.

for which the greatest underprediction was observed with both the Hertzian and Tatara contact models. The resulting force–strain curve was compared with the curve obtained from the initial model in Figure 4.16 and as can be seen they are virtually identical. The forces in the resulting endpoints were 4.682 N using the initial PoC, and 4.706 N using the expanded PoC, which give a relative difference of just 0.5% between them. This confirms that the previously selected PoC region and mesh capture the forces stemming from the side contacts with sufficient accuracy.

It should be noted that there is a seemingly non-conservative behaviour present in Figure 4.16, where the force increases after the maximum strain is reached creating a loop in the plot. That can be attributed to further contact happening in the non-parallel collisions after the defined endpoint in the simulations. It is also worth noting that this behaviour would be even more prominent if the rods coming into contact were longer.

As explained in Section 4.1.1 the simulation endpoint was selected as the moment when the maximum strain is obtained at the middle of the granule using a single node at the top and the bottom of it (shown in Figure 4.4). However, the force in Abaqus is calculated via the surface-to-surface contact interaction, which takes into account the entire rod rather than just the force calculated at the central node. Therefore, after the defined endpoint, the rods deform in a way that results in a 'hugging' motion due to the non-parallel collisions, which leads to an increasing force being recorded.

This has been confirmed by checking the force–strain curve obtained in a parallel collision, where that loop is not present. Furthermore, when the internal energy of the model — which

makes up 75% of the total energy at the endpoint — was plotted against strain, the curve obtained had a very similar shape which further confirms the premise.

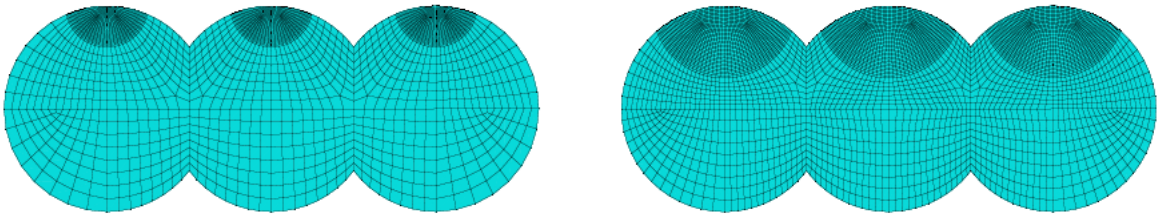

(a) Original Point of Contact region. (b) Expanded Point of Contact region.

Figure 4.15: (a) Original and (b) Expanded Point of Contact regions used to confirm that the side contact forces were captured properly in an angled collision. The original PoC region has a radius of $0.3R$ and the expanded PoC region has a radius of $0.7R$, where R is the rod radius. The side contacts of concern can be seen in the schematic in Figure 4.10.

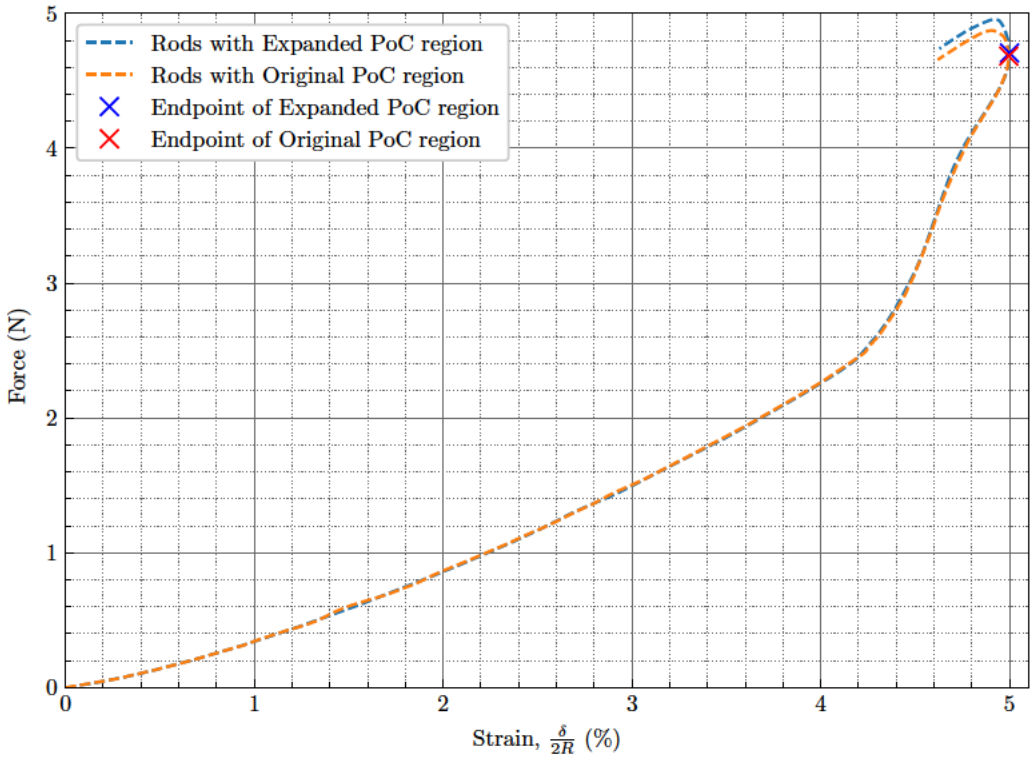

Figure 4.16: Comparison of the force–strain curves of two identical collision configurations, testing the impact of an expanded PoC region in the mesh. The force–strain curve of the model using the original PoC region is plotted in orange, while the one with the expanded PoC region is plotted in blue. Collision configuration: three-sphere rods, 30° angle, 20% sphere overlap, 5% strain.

4.3 Shape Approximation Errors

In order to focus on the errors stemming from the shape approximation when using the MS approach, the entire comparison is taking place within the FEM domain, rather than using any DEM contact models. FEM simulations of spherocylinders coming into contact were set up as outlined in Section 4.1, but for this part the length of the rods was fixed to achieve a 3:1 aspect ratio. The contact between two Perfect Spherocylinders (PSC) was set as the basis for the comparison against different MS rod configurations. The rods using the MS approach had the same length as the PSC, but they were consisting of different numbers of spheres in each case. Seven different rod configurations were compared against the force response of the PSC.

For the selection of the number of spheres used in the MS rods, the volume fraction occupied by the MS rod compared to the PSC was used. While initially the overlap fraction of the constituent spheres was used, it was disfavoured as the volume fraction method provides a clearer measure as to how close the MS rod can get to the PSC. Both measures are shown in Figure 4.18. Although the sphere overlap fraction covers a wider range, the volume fraction provides better resolution and a clearer cut-off point for the curves shown and hence it better signifies the extent to which the MS rod can approximate a PSC.

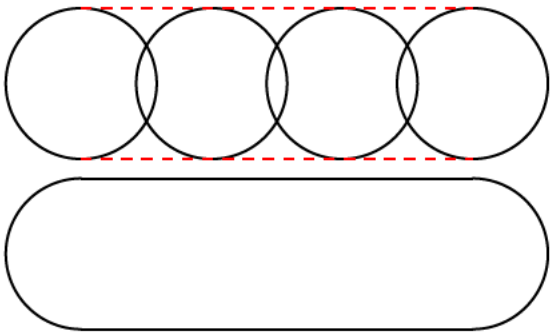

Figure 4.17: Schematic representation of the shape approximation error when modelling a perfect spherocylinder using the Multi-Sphere method.

As was already explained in Section 4.2.2, one of the constraints set was that the point of contact in all cases would have to be in the middle of the rod. Therefore the MS rods were limited to having an odd number of spheres in order to ensure a stable point of contact on the central sphere, rather than the gap between 2 constantly changing sphere positions. Consequently, and taking into account how the volume fraction occupied by the MS rods changes, MS rods consisting of 3, 5, 7, 9, 11, 13 and 21 spheres were examined. The rod configurations are shown in Table 4.2 and their properties are highlighted in Figure 4.18. The first 6 rods capture the entire curved part of the volume fraction curve, while the 21-sphere rod was added to demonstrate that the difference between that and the 13-sphere rod is relatively small. Table 4.3 shows the number of spheres comprising the rod configurations used in the simulations with their respective sphere overlaps as calculated using Equation 4.2.

It is important to note that in the FEM simulations the MS rods consisting of 3 spheres, that would normally have no overlap between them, were assigned a 0.1% distance overlap. This was done to ensure the FEM simulations would converge without any unwanted side-effects.

Table 4.2: Fixed-Length Rod configurations

Rod configuration	Fixed-Length Rod
3-sphere rod	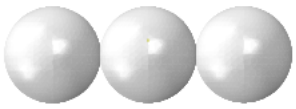
5-sphere rod	
7-sphere rod	
9-sphere rod	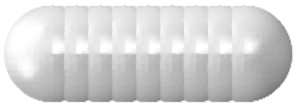
11-sphere rod	
13-sphere rod	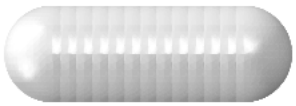
21-sphere rod	
Perfect Spherocylinder	

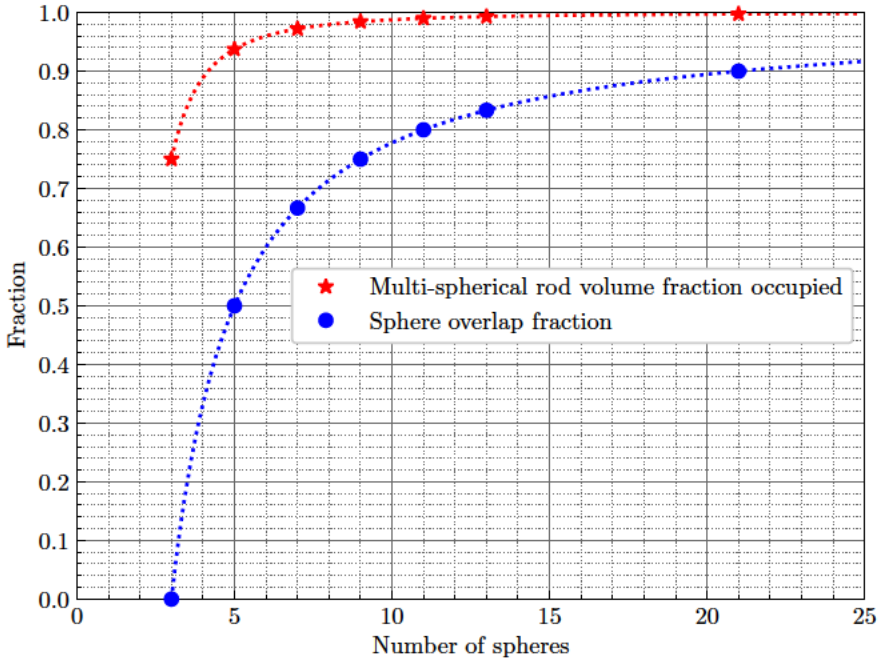

Figure 4.18: Comparison of two methods of MS rod characterisation: volume fraction occupied by the MS rod compared to the perfect spherocylinder and the overlap fraction of the constituent spheres in the MS rod.

4.3.1 Fixed-Length Multi-Spherical Rods vs. Perfect Spherocylinder

The results are summarised in the contour plots in Figure 4.19. Just like in the Contact Model comparison cases, the parallel contacts were simulated using quasi-static compressions of the different rods with a single simulation performed per rod configuration tested. However, for the angled collisions parametric studies were necessary to neglect the inertial effects and thus a single simulation was performed per strain value per rod configuration tested.

On account of this, additional rod configurations were included for the parallel contact to increase the contour plot's resolution. Moreover, since it is a parallel contact, the Fixed-Length Rods (FLR) are no longer constrained by the need to only be comprised of an odd number of spheres so some even-numbered sphere rods were also included as indicated in Table 4.3. A further 337 FEM simulations were performed in order to complete this analysis.

In order to expedite the data collection, part of the simulation set-up of the angled collisions was automated resulting in some of the datapoints' strain values not aligning perfectly together as seen in Figures 4.19b–4.19e. While this does not affect the results significantly, because the comparison is done against another set of defined datapoints (the force response of the PSC), a certain degree of interpolation had to be implemented to accurately measure the errors present. Following a similar format to Hertz's contact model, a power curve ($y = ax^b$) proved to be a good

fit to the data giving Goodness of Fit (R^2) values ranging from 0.9993 to 0.9999. An example of the curve fitting is provided in Figure C.2 in Appendix C. This curve fitting was not necessary in the parallel contact as the strain values in all the datasets are perfectly aligned together.

Table 4.3: Fixed-Length Rod configurations simulated with their respective sphere overlap percentages as well as the occupied volume fraction with respect to the PSC. The additional rod configurations used for the parallel contact are also displayed in the bottom section of the table.

Rod Configurations	Sphere Overlap	Volume Fraction
3 spheres	0 %	75.00 %
5 spheres	50 %	93.75 %
7 spheres	67 %	97.22 %
9 spheres	75 %	98.44 %
11 spheres	80 %	99.00 %
13 spheres	83 %	99.31 %
21 spheres	90 %	99.75 %
Additional Rod Configurations		
4 spheres	33 %	88.89 %
6 spheres	60 %	96.00 %
8 spheres	71 %	97.96 %
15 spheres	86 %	99.49 %
25 spheres	92 %	99.83 %
41 spheres	95 %	99.94 %
51 spheres	96 %	99.96 %
61 spheres	97 %	99.97 %
101 spheres	98 %	99.99 %

Parallel contact contour plot (Figure 4.19a) First of all there is some discontinuity in the contour lines, which can be attributed to the lower resolution towards the bottom of the plot. That is the limitation of this kind of analysis as the gaps are greater between the rod configurations at small sphere numbers. This is more clearly seen in Figure C.3 Appendix C, where the location of all datapoints is also included.

As expected, the greater the sphere overlap or number of spheres, the closer the force response of the FLR is to that of the PSC as is seen in Figures 4.20 and 4.21. That can also be seen by the smaller deviation in the top part of the contour plot (Figure 4.19a) as well as the 0% error region at the very top of the graph. Of particular interest, however, is the 0% contour line that reaches down to the 98% sphere overlap, where the 101-sphere rod lies. It is one of the additional rod configurations included and it occupies 99.99% of the volume of a PSC. This implies that beyond approximately 1.75% strain the force response of that MS rod is no longer affected by the difference in shape from that of the PSC. Or at least, the error seems to be smaller than Matplotlib's default tolerance value. That is most probably due to the interspherical gaps being small enough to be completely filled when that strain is applied on the MS rod at that specific

Poisson's ratio.

On the other hand, at the lower end of the sphere overlap percentages there are significant errors due to the missing material between the constituent spheres. The large interspherical gaps allow for the MS rods to deform more freely, relieving the stresses and hence causing the MS rods to generate a considerably lower force response compared to that of the PSC. The Poisson's ratio also has a role to play. Also noteworthy is the fact that the parallel contact is the only case where the greatest error exists at low strains in the low sphere overlap region. This can again be attributed to the large interspherical gaps since the contact takes place along the entire length of the rod.

Angled Collisions (Figures 4.19b–4.19e) First of all, there is a need to mention the biggest limitation of this analysis; that being the large jumps at the lowest sphere overlaps in the contour plots. Those are jumps from 0% sphere overlap to 50% sphere overlap that occur when testing the 3-sphere rod and the 50% sphere overlap. Hence, caution should be exercised when interpreting the results in those parts of the plots due to insufficient data.

Noting that in the angled collisions the plots cover a wider strain range up to 5%, the location

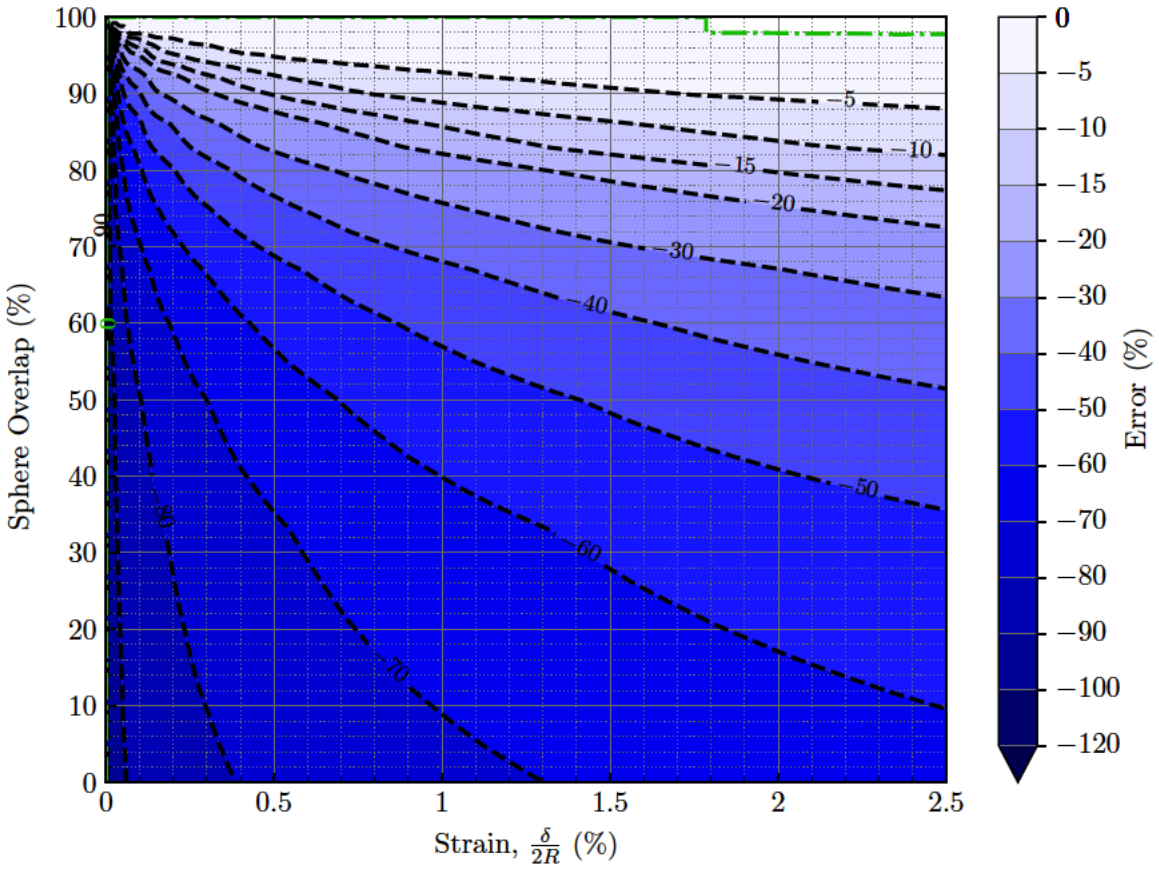

(a) Fixed-Length Rod Parallel contact

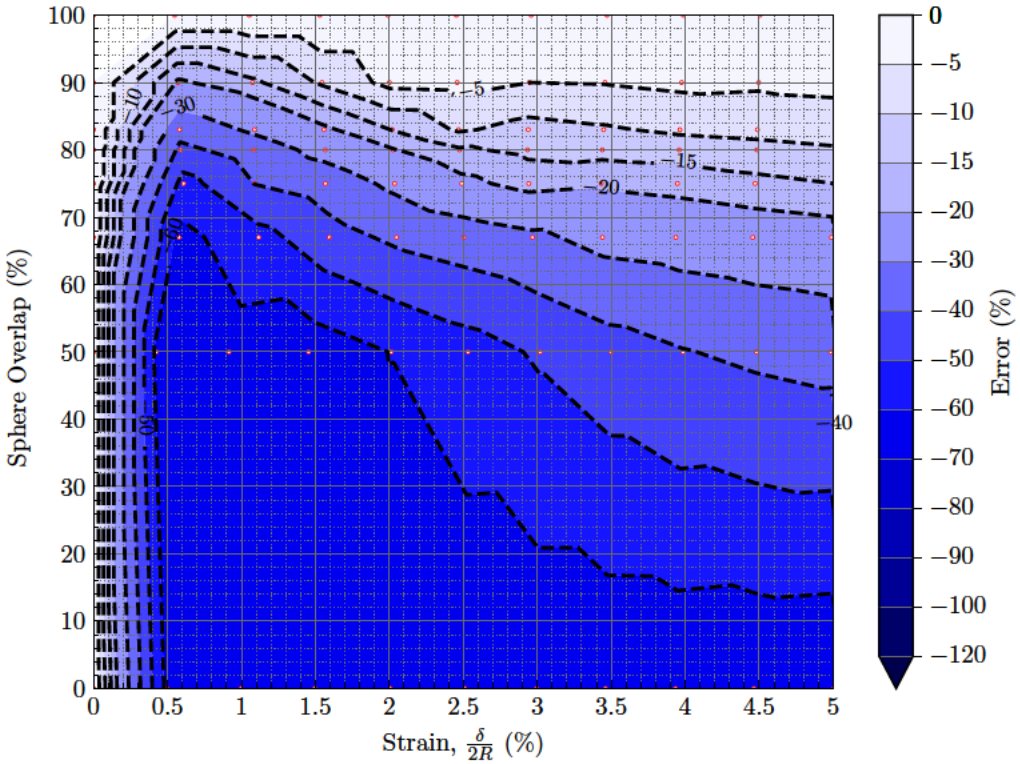

(b) Fixed-Length Rod 30° collision

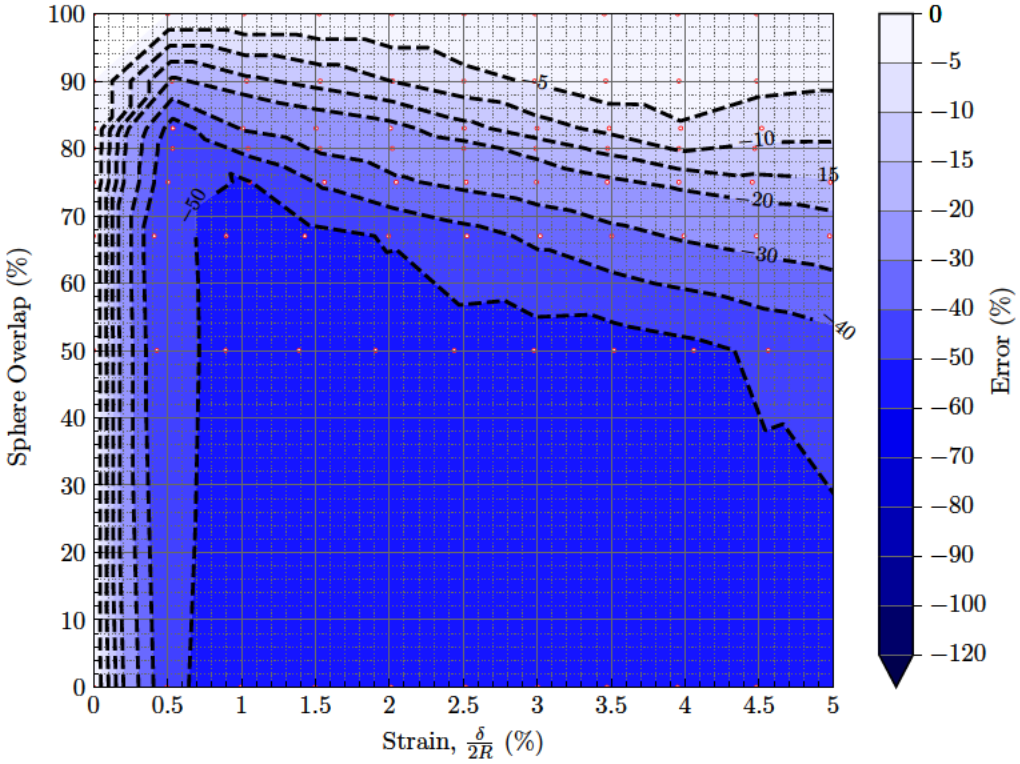

(c) Fixed-Length Rod 45° collision

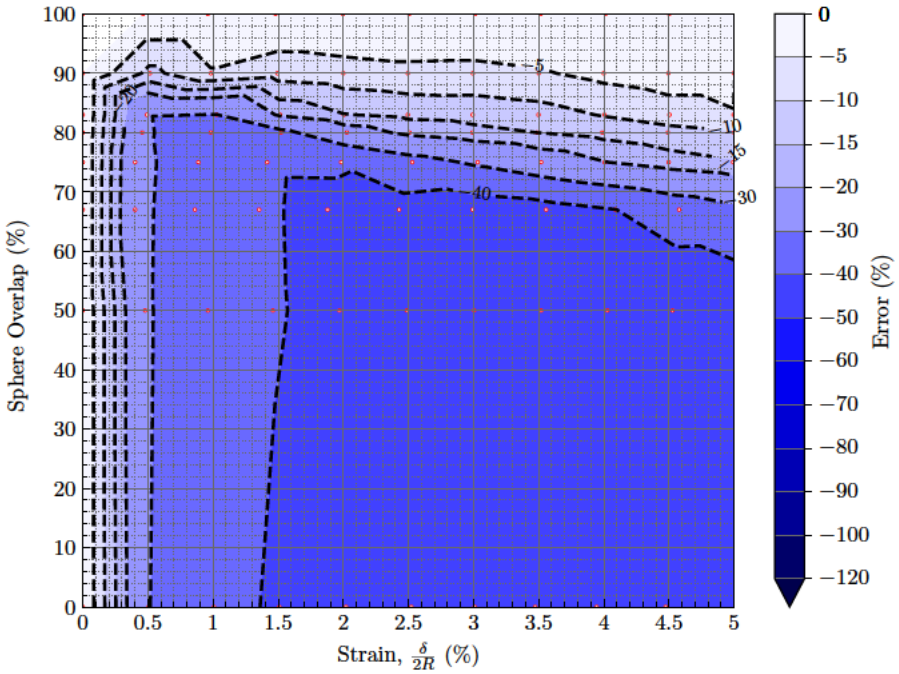

(d) Fixed-Length Rod 60° collision

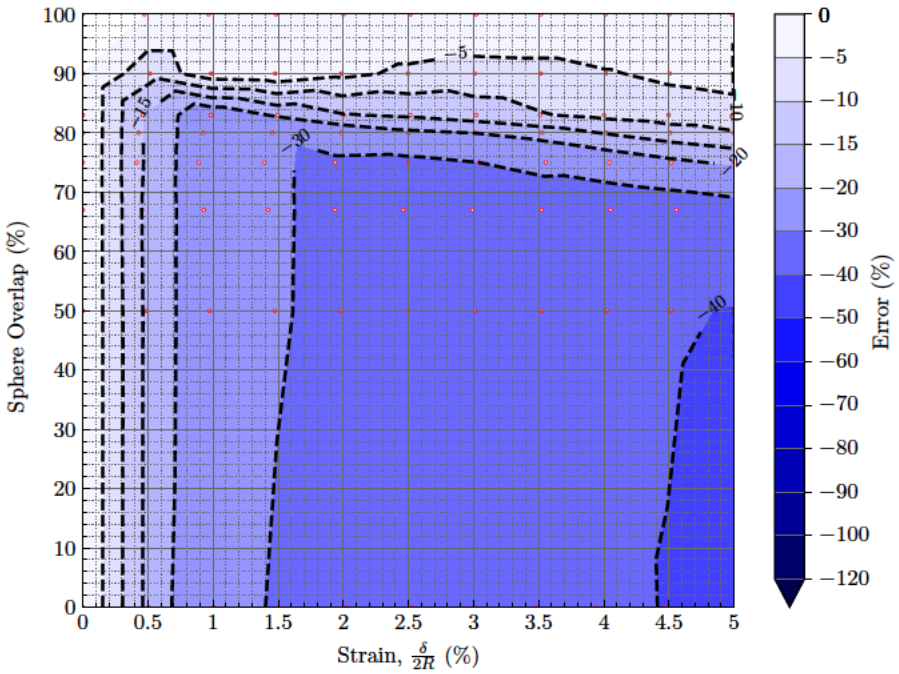

(e) Fixed-Length Rod 90° collision

Figure 4.19: Contour plot showing the error bounds between the force responses of the MS rods and the perfect spherocylinder. The negative errors in blue indicate the configurations where the MS rods underestimate the force response when compared to that of the perfect spherocylinder. Since the responses of the MS rods are compared against that of the perfect spherocylinder, all the errors are negative.

of the greatest error shifts from the bottom left corner of the plot (low strain-low sphere overlap region) to the bottom right corner (high strain-low sphere overlap region) and that is the case for all angled collisions. This is due to the difference in the contact areas between the contacting low sphere FLRs and PSCs, with the contact areas in the parallel contact being the most disparate. This can also be seen in the schematic shown in Figure 4.10.

Additionally, as the angle of the collisions increases, the contour lines uniformly recede. That can also be attributed to the contact areas between the 2 types of rods becoming more similar as the angle increases (Figure 4.10). Furthermore, this also affects the errors at the 60° and 90° collisions at sphere overlaps beyond 70%, where the sphere overlap becomes the greatest factor driving the errors present. Strain seems to have a minimal effect in those regions as opposed to the lower sphere overlap rod configurations where it has more weight. The reason being the large interspherical gaps, similar to the parallel contact cases.

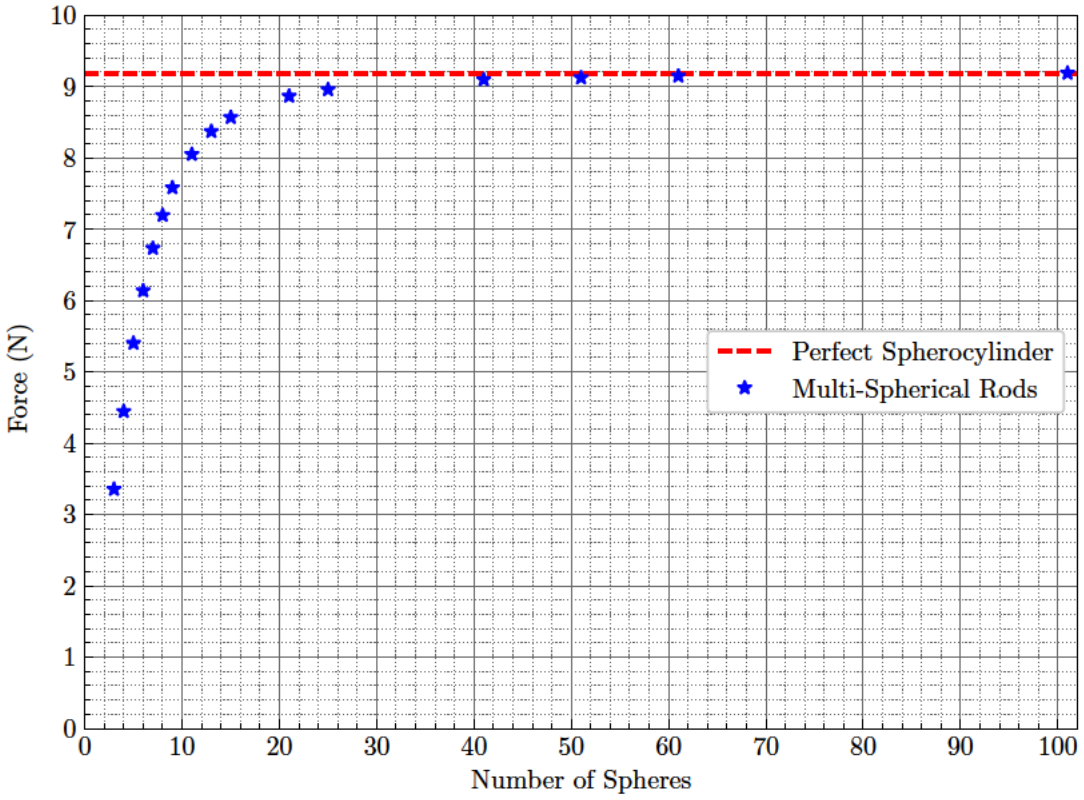

Figure 4.20: Force responses of rods at 2.5% strain at a parallel contact against the number of constituent spheres.

Further discussion on the Shape Approximation Error Although the shape approximation errors can be essentially eliminated by using an infinite amount of spheres, they still have significant impact in the errors present in multi-spherical DEM. This is more evident in the parallel contact cases where the difference in the contact areas between the contacting low

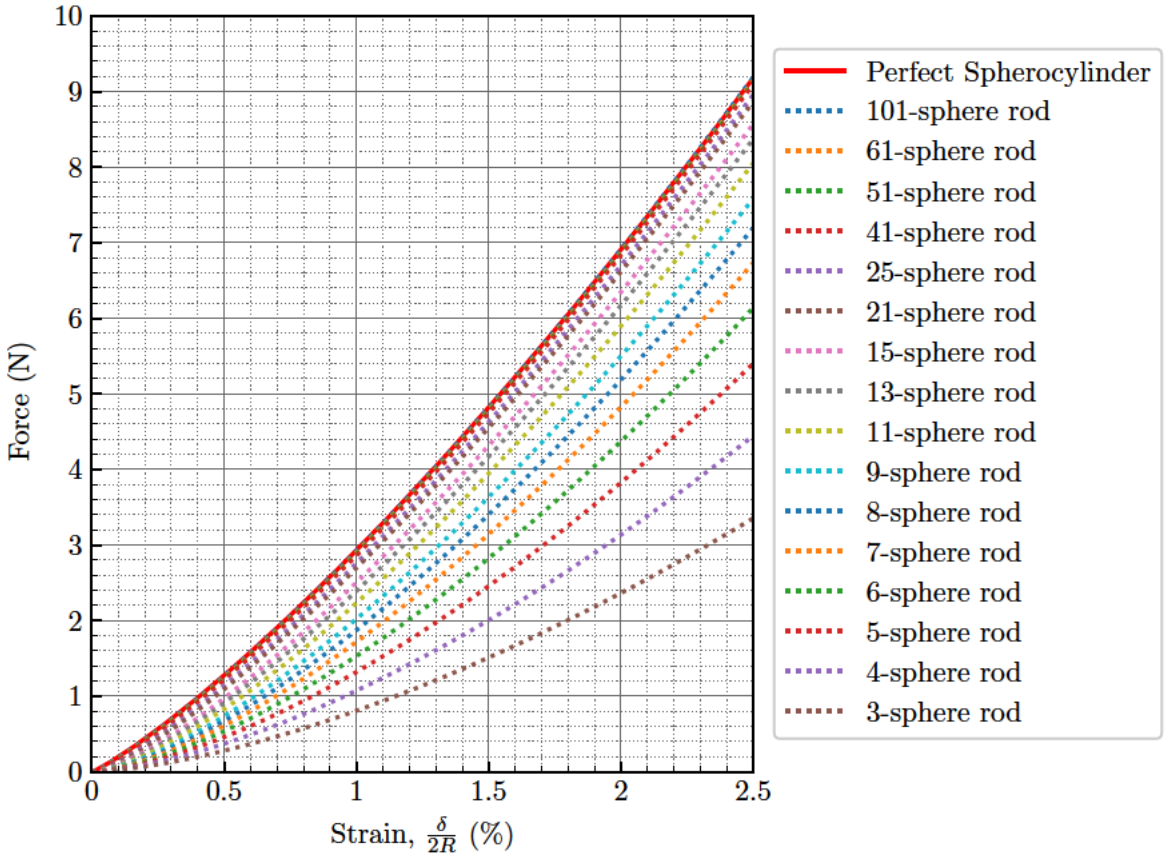

Figure 4.21: Comparison between MS rod and perfect spherocylinder force responses at a parallel contact up to 2.5% strain.

sphere FLRs and PSCs is the greatest. This is shown in the schematic in Figure 4.10.

It should be noted that even though the focus is on errors to do with the shape approximation when using the MS approach, any errors that deal with interlocking particles due to the different geometry are completely ignored. That was the main reason why MS rods with an odd number of constituent spheres were the only ones examined — besides the two-sphere parallel contacts (quasi-static compressions). Avoiding interlocking means that dealing with the tangential forces was also avoided since that is beyond the scope of this research.

4.4 Optimal rod configuration

When spherical contact models are used in non-spherical particle DEM simulations both contact model errors and shape approximation errors have a distinct presence in the results. Focusing on each error at their extremes it can be observed that the CM errors reach greater values and vary more throughout the different configurations evaluated, with the largest errors consistently reaching values $> 700\%$ or even greater in the case of the Linear CM. The shape approximation

error on the other hand never reaches errors beyond 100% in absolute terms. Additionally, by using a very large number of constituent spheres the shape approximation error can be effectively minimised. Furthermore, having an accurate shape representation of the non-spherical particles is also extremely important for contact detection, something that was not taken into account in this work. However, since having a large number of constituent spheres negatively impacts the contact model error, it automatically becomes an optimisation problem. Taking all of that into consideration, the optimal solution for using the MS approach seems to be particle configurations with sphere overlaps around 60%. These configurations ensure a reasonably accurate shape representation of the spherocylinders (in this case) while rod configurations remain in the region where strain rather than sphere-overlap is the greatest cause of CM errors.

4.5 Multi-Spherical errors conclusions

In this chapter, an FEM-based framework was established that allowed the quantification of two sources of errors present in DEM simulations when the multi-spherical approach is used to model non-spherical particles. The two types of errors quantified were: (i) the contact model error arising from adopting a contact model suitable for individual spheres and (ii) the shape approximation error arising from modelling a specific desired particle shape using a finite number of spheres.

Uniaxial compressions of spherocylindrical rods as well as collisions between identical spherocylinders were performed in FEM at different angles. In order to quantify the contact model error, a comparison was performed between the force responses of two-sphere and three-sphere rods obtained in the FEA and the force responses predicted by the various DEM contact models being evaluated.

Generally, the contact model errors seems to be driven mainly by the strains applied when the constituent spheres of the Multi-Spherical (MS) rods overlap by less than 60%. At greater sphere overlaps, the sphere overlap percentage becomes the main driving force of the errors almost completely overshadowing the effect strain has on those errors. At the angled collisions, the contact model error seems to be decreasing in absolute terms as the collision angle increases. This is possibly due to the contacts more closely resembling that between two individual spheres.

As for the shape approximation error, the comparison was done fully within FEM. The force response of the perfect spherocylinders was compared to that of MS rods with a varying number of constituent spheres. The shape approximation error can essentially be eradicated by using a very large number of constituent spheres to get an accurate representation of the desired granule shape. Hence, given the importance of having an accurate shape representation for contact detection — even though that was out of the scope of this thesis — the optimal rod configuration when using the MS approach seems to be a MS rod with sphere overlaps around 60%. While the error quantification in this chapter was focused on spherocylindrical particles, results using this exemplar shape are expected to be qualitatively applicable to any MS system.

Chapter 5

Contact: Depth of Penetration or Volume Overlap

Most established Discrete-Element Modelling (DEM) contact models are based on the overlap distance between the granules coming into contact as seen in Chapter 2. This chapter focuses on contact models that are based on the volume of the contact overlap. The two contact models that are examined are the one proposed by Feng (2021b,c) as well as a more simplified version of the same model that is used in Wang *et al.* (2021).

For the examination of these volume-based contact models, the Finite Element Method (FEM) was used to simulate the indentation of a spherical granule with different indenters. This chapter explores the contact models tested, how they compare with the FEM results and their applicability into DEM is discussed.

5.1 Volume overlap-based contact models

5.1.1 Feng contact model

Feng (2021b) presented an energy-conserving approach for modelling the contacts of arbitrarily shaped particles. The energy-conserving nature of the contact model ensures that the total energy of the system is conserved during particle interactions (Feng, 2021a,c).

According to Feng (2021b), a contact model (CM) has a geometric aspect and a physical aspect. Typically in DEM, since most existing CMs were developed for spheres, the geometric aspect is treated mainly for contact detection, whereas the physical aspect is specified by various contact interaction or constitutive laws. This results in a decoupled contact modelling framework, which can cause non-physical behaviours in DEM simulations of non-spherical granules in particular.

A good example is the case of a polygonal particle–wall collision where a typical single-contact model is used (Fraige *et al.*, 2008). As the contact is only defined at a single point — the point with the largest distance overlap — the position of the force vector is jumping around during the

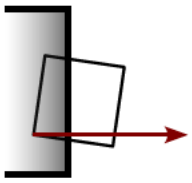

(a) Polygonal contact at t_1

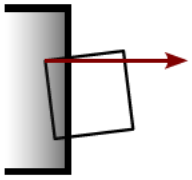

(b) Polygonal contact at t_2

Figure 5.1: The model detects two contact points at the vertices of the polygonal granule, but the force is calculated at the point with the largest overlap in (a). The particle then rotates and the position of the force vector "jumps" to the other contact point in (b). Schematic adapted from Fraige *et al.* (2008).

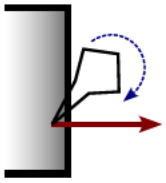

(a) Elongated particle contact at t_1

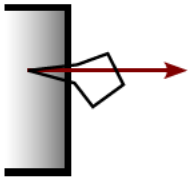

(b) Elongated particle contact at t_2

Figure 5.2: With enough rotational energy, an elongated particle can suddenly reach a position where its elongated part completely overlaps with a wall (or another particle) during contact. This can cause a massive spike in the contact force calculation due to the large distance overlap increase.

collision as shown in Figure 5.1.

Another good example is a case where a rotating elongated particle comes into contact with another particle or wall. As the elongated particle rotates, it can reach a position where suddenly the distance overlap massively increases, causing a spike in the contact force. This is shown in Figure 5.2.

Feng sought to solve these issues by defining the contact geometric features as well as the force magnitude in a more systematic way; by establishing a theoretical framework based on the condition that the potential energy of the particles coming into contact is conserved for an elastic impact. Feng established that the normal contact force must be the gradient of a scalar potential field, or the contact energy function $w(V_c)$, where $w(V_c) = kV_c^m$.

Therefore, according to Feng (2021c) the magnitude of the normal contact force, F, takes the form:

$$F_{\text{Feng}} = w'(V_c)\, S \Rightarrow F_{\text{Feng}} = mkV_c^{m-1} S \tag{5.1}$$

where constant $m \geq 1$, k is the normal stiffness index (albeit with different units), V_c is the contact volume overlap, S is the (scalar) contact area.

5.1.2 Linear Volume-Based (LVB) contact model

A Linear Volume-Based (LVB) contact model was used in Wang *et al.* (2021) for simplicity in their proposed spherical harmonic-based approach for irregular particle shape representation. This model assumes a linear relationship between the magnitude of the normal contact force and

the contact volume overlap and is given by:

$$F_{\mathrm{LVB}} = k_{\mathrm{LVB}} V_c \tag{5.2}$$

where k_{LVB} is the volumetric normal contact stiffness, which can be obtained from the material properties (indices of contact stiffness) of the granules in contact using the Equation 5.3:

$$k_{\mathrm{LVB}} = \frac{k_i k_j}{k_i + k_j} \tag{5.3}$$

For practical application the stiffness factors would need calibration based on experimental results.

5.2 Methodology: Spherical granule indentations

In order to test the volume-based contact models introduced, indentations of a granule were simulated using FEM. A spherical granule was used since that allows for a direct comparison with the already established contact models that were evaluated in Chapter 4. While two different materials were tested that had Poisson's ratios of $\nu = 0$ and $\nu = 0.3$, the rest of the material and model properties were left the same as defined in Chapter 3. The sphere had a radius of 0.1 mm and the Young's modulus remained the same at 6.1 GPa. The main variable in the different scenarios tested was the shape of the indenters, in order to focus on the variable volumetric deformations obtained during indentation.

Two different types of rigid indenters were used, both with different variations: conical indenters and cylindrical indenters. For both indenter types used, all tips and edges were rounded off in order to avoid any singularities where excessive stresses arise due to point loads (England, 1971). A sphere with radius 0.005 mm replaced the apex of the conical indenter, and the cylinder's edge was rounded using an identical radius. These are presented in Figure 5.3. Five conical indenters were used, characterised by the angle of the arc of the spherical cone apex, θ_i: 15°, 30°, 45°, 60° and 75°. For additional shape variability, three cylindrical indenters were used, characterised by their radius, r_i: 0.01 mm, 0.015 mm and 0.02 mm.

(a) Conical indenter (b) Cylindrical Indenter

Figure 5.3: Indenters used for the indentation tests. The apex of the conical indenter and the edges of the cylindrical indenter were rounded to a spherical surface with radius 0.005 mm.

Initially, an attempt was made to simulate these indentations by kinematically projecting the sphere onto the indenters to examine the volumetric deformations using a single point of contact. However, this method proved ineffective to obtain robust results at high enough strains while converging to a solution. Therefore, the simulations were performed quasi-statically, similar to the uniaxial compressions presented in the previous chapters.

Since these indentation simulations were performed quasi-statically, the sphere was placed between two identical indenters rather than using one indenter and a flat plate. Utilising symmetry ensured that the volumetric deformations between the top and bottom of the particle were also symmetric and uniform.

As the granule adopted for these indentation tests was spherical, axisymmetry was adopted to simplify the model in Abaqus. Using a similar meshing technique as in the previous chapters, 16040 CAX4 (4-node bilinear axisymmetric quadrilateral) elements were used. In order to better capture the contact surface area though, the elements at the point of contact were a hundred times finer. An additional symmetry plane was imposed horizontally as shown in Figure 5.4. The indenter in all cases was quasi-statically pressed onto the sphere causing it to deform. The data obtained was the indentation depth, the surface contact area and the change in volume of the spherical granule from where the volumetric deformation could be calculated. In these scenarios, the indenter displacement only reached strains of up to 2% per contact (as defined in Chapter 3) rather than 2.5%, because not all simulations were converging at strains $\geq 2.5\%$. That amounted to a 0.004 mm displacement of the indenter into the spherical granule.

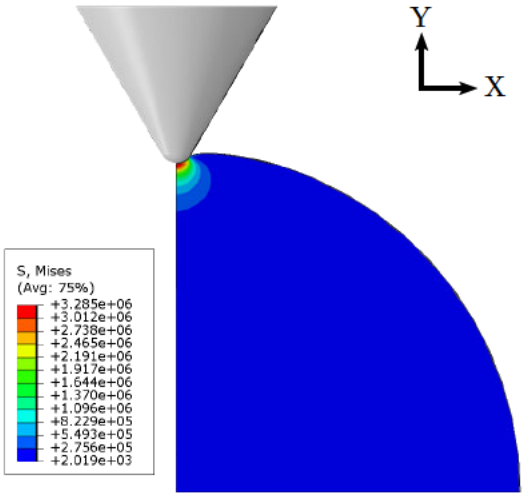

Figure 5.4: Axisymmetric model example used for the indentation tests. There is a symmetry plane at the bottom boundary while the left boundary is defined as the axis of axisymmetry for the spherical granule.

5.3 Indentation tests and discussion

5.3.1 Feng model evaluation

In order to evaluate the model proposed by Feng the indentation tests were performed with the five different conical indenters on both materials. From Equation 5.1, m and k were used as fitting parameters. They were expected to only depend on the material properties, since they are supposed to be independent of the shape (Feng, 2021c).

Table 5.1: Feng parameters m and k obtained after fitting as shown in Figure 5.5.

Poisson's ratio	0		0.3	
Angles	**m**	**k** $(\times 10^6)$	**m**	**k** $(\times 10^6)$
15°	1.079	2.801	1.081	3.165
30°	1.136	10.498	1.116	8.728
45°	1.354	200.919	1.309	144.869
60°	1.366	235.854	1.339	219.153
75°	1.366	235.854	1.339	219.153

The force responses obtained from FEM and Feng are shown in Figure 5.5. Additionally, the force responses predicted by Hertz and Tatara in those scenarios were also plotted as an indication of current practices. It should be noted that Hertz and Tatara force responses are constant for all different indenters in Figures 5.5a and 5.5b. That is because the distance overlap during contact with all the different indenters remains constant, even though the indenter's shape changes.

A very good fit between Feng and the FEM results can be achieved for all conical indenters as well as both materials; however, that is mainly due to having two fitting parameters. All Feng curves have a stepped shape due to the force response relying on the contact surface area obtained from FEM. The contact surface area is dependent on the size of the elements used in the simulations, so the finer they are (at the point of contact), the smoother the resulting curve will be.

While a good fit can be found, it is impractical as this process would have to be repeated for every type of different contact shapes in order to find suitable fitting parameters. The fitting parameters for Figures 5.5a and 5.5b are presented in Table 5.1. As Feng's contact model is in theory independent of shape, what was expected was that there would be a single pair of fitting parameters per material. Those parameters should be constant even though the shape of the indenters was changing. Instead, they drastically change as the angle of the arc of the spherical cone apex, θ_i increases. Especially the value of k is changing by entire orders of magnitude. The only exception is the conical indenters with $\theta_i = 60°$ and $\theta_i = 75°$. This, however, is due to the depth of the indentation applied on the sphere. As already mentioned in Section 5.2, the distance the indenters travel is 0.004 mm while the radius of the spherical cone apex is 0.005 mm. A greater indentation would need to be applied in order for the difference in the force responses to become visible, simply because the round apex is the only part of the indenter in contact with the granule.

Perhaps the reason the model parameters are changing with the shape of the indenters lies in the assumptions made for the development of the model. In particular, there is an assumption stating that the normal contact pressure is uniformly distributed across the contact region (Feng, 2021c). However, that is not the case as outlined in Johnson (1985), where the stress distribution at the surface of a spherical granule is presented as calculated by Hertz. A comparison between

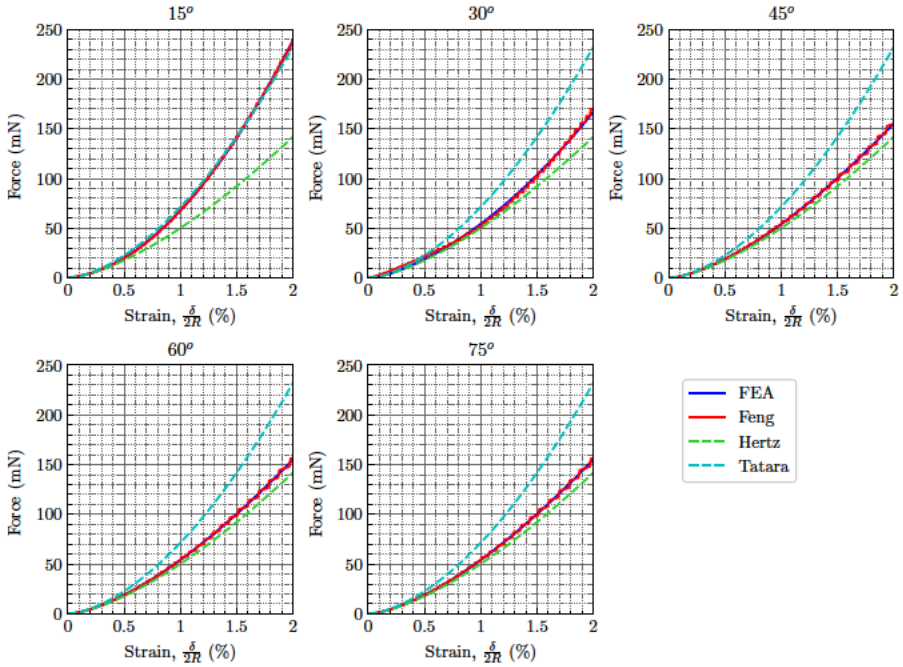

(a) Poisson's ratio = 0

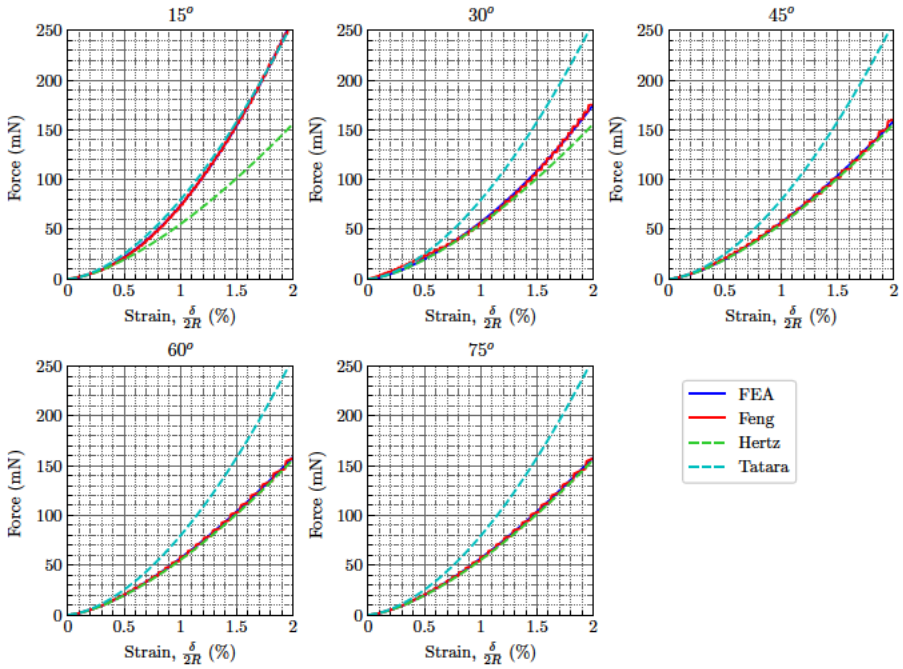

(b) Poisson's ratio = 0.3

Figure 5.5: Conical indentation force responses. Feng's fitted parameters are given in Table 5.1.

a uniform stress distribution and the Hertzian stress distribution is also presented in Figure 5.6 obtained from Johnson (1985, p. 94). While this is just speculative, it could be the reason why the model parameters m and k are not just dependent on the material properties.

Upon inspection of the resulting parameters in Table 5.1 obtained from curve fitting, it can be observed that the parameters are not greatly affected by the Poisson's ratio. It seems to have a greater effect on k, but both of them are much more affected by the change in the indenter angle θ_i. Another observation is that even though the parameters drastically change, the Force–Volume curves do not. There is a relatively large change from the 15° indentation to the 30° indentation, but the rest give a fairly similar force response.

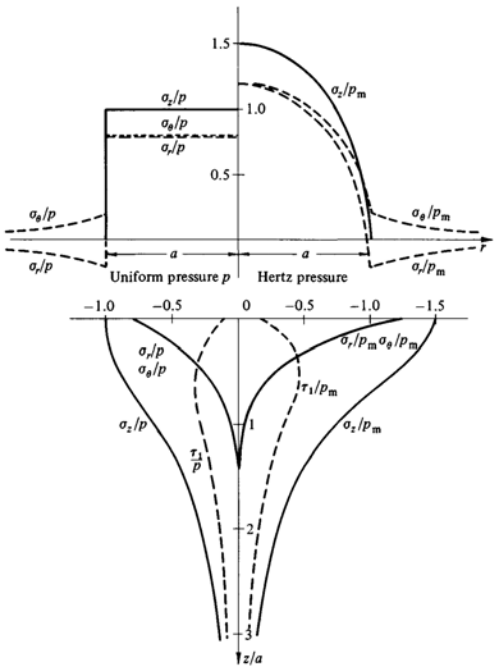

Figure 5.6: Stress distributions at the surface of a spherical granule and along the axis of symmetry caused by a uniform pressure (left) and a Hertzian pressure (right) acting on a circular area with radius a. Taken from Johnson (1985, p. 94).

It is important to note that these issues arise even when the volumetric deformations from the FEA are used. Very similar results are obtained when the analytical contact volume overlap and contact surface area are used for the Feng calculations. In a typical DEM simulation, the analytical values should be used, which adds a layer of complexity. The calculation process for both the analytical contact volume overlap and the contact surface area for the smooth cone indenters is shown in Appendix D. While these are not too tricky to obtain even for non-spherical particles, the difficulty increases with the shape complexity of the particles. Considering the impracticalities and the limitations presented above led to the need for testing the simpler LVB model used in Wang *et al.* (2021).

5.3.2 Linear Volume-Based (LVB) model evaluation

A very similar process was followed for the evaluation of the LVB model. The force responses obtained from the conical indentation tests in the FEA were plotted against the volumetric deformations obtained from the FEA. Since the volume of the elements comprising the granule at each timestep is available, the volumetric deformations in the FEA can be obtained by subtracting the total volume of the granule at each timestep from the original volume of the undeformed granule. The force responses obtained for both materials resulted in straight lines being produced, so additional simulations were performed using the three cylindrical indenters mentioned in

Section 5.2 to add to the indenters' shape variability. All of the force responses obtained were plotted together in Figure 5.7.

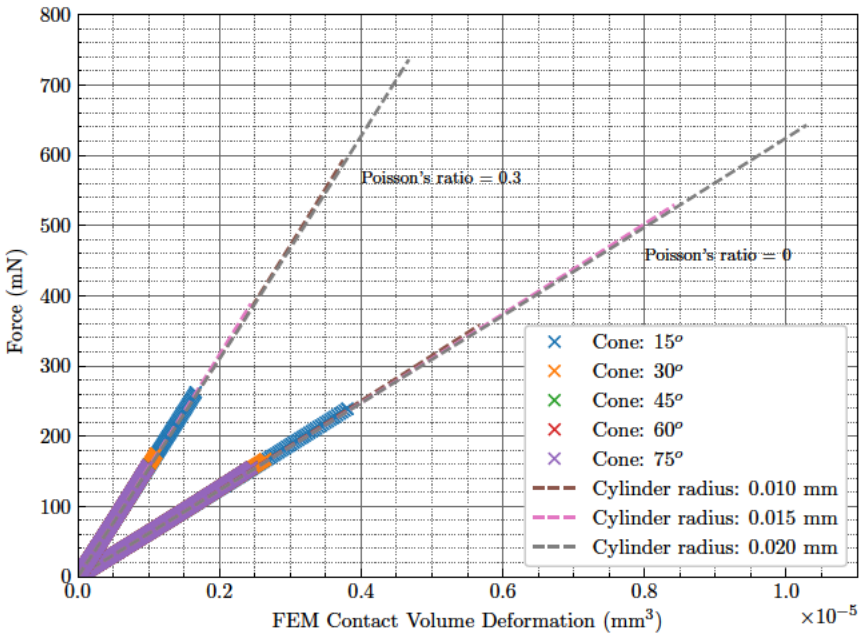

Figure 5.7: Indenter force responses of two different materials plotted against the volumetric deformation obtained from FEM.

As can be seen in the results plotted, the force responses of each material line up almost perfectly with each other independently of the shape of the indenter used to produce the response. This shows that k_{LVB} seems to be a material property rather than just a calibration parameter like in the other models, so there should be a way to relate it to the material's Young's modulus and its Poisson's ratio.

This linearity could be expected to a certain extent since the FEM model assumes linear elasticity; Abaqus' inbuilt elastic material model routine was used for the simulations. This is fine for small deformations which is nevertheless what is expected in DEM. The results, however, may vary if linear elasticity is not assumed.

One obvious limitation, however, is that the 'actual' volumetric deformation will not necessarily be available in a DEM simulation. Therefore, the analytical volume overlap of such a contact within DEM should be calculated and the force should be computed based on that volume instead. Obtaining this might be difficult for complicated particle shapes, but still feasible even for non-spherical particles. That has been done for the conical indentations and the results are shown in Figures 5.8a and 5.8b for the materials with Poisson's ratios of $\nu = 0$ and $\nu = 0.3$, respectively. The plots produced no longer consist of overlapping straight lines, unlike those created using the FEM-obtained volumetric deformations.

This issue could be resolved if a relation could be established mapping the analytical contact volume overlap to the actual volumetric deformations. The analytical contact volume overlap

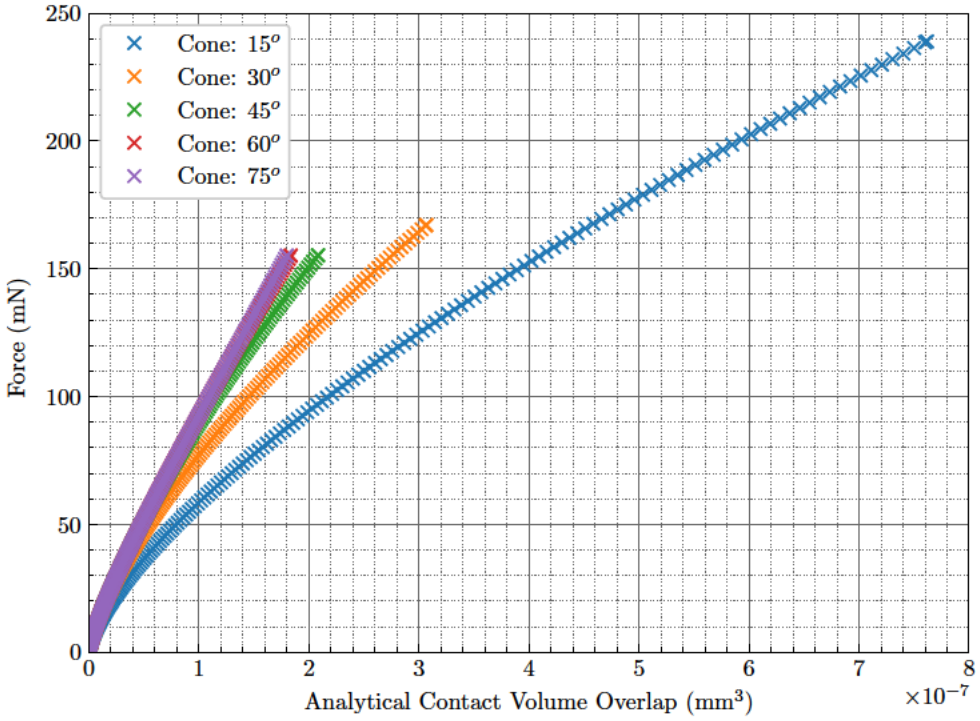

(a) Poisson's ratio = 0

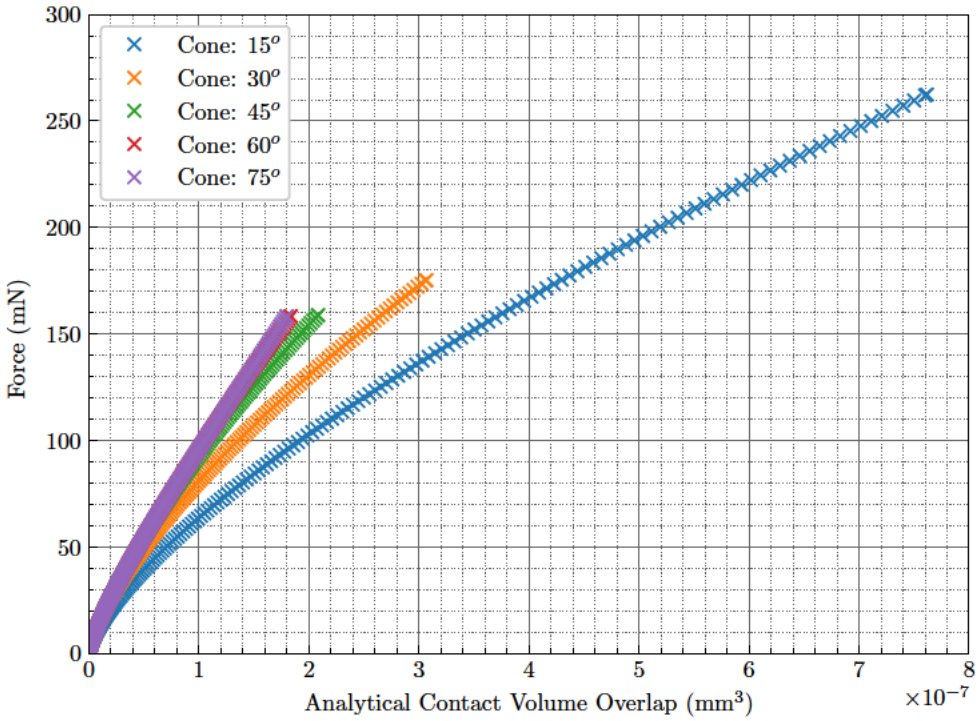

(b) Poisson's ratio = 0.3

Figure 5.8: Conical indentation force responses plotted against the analytical contact volume overlap rather than the volumetric deformation obtained from FEA.

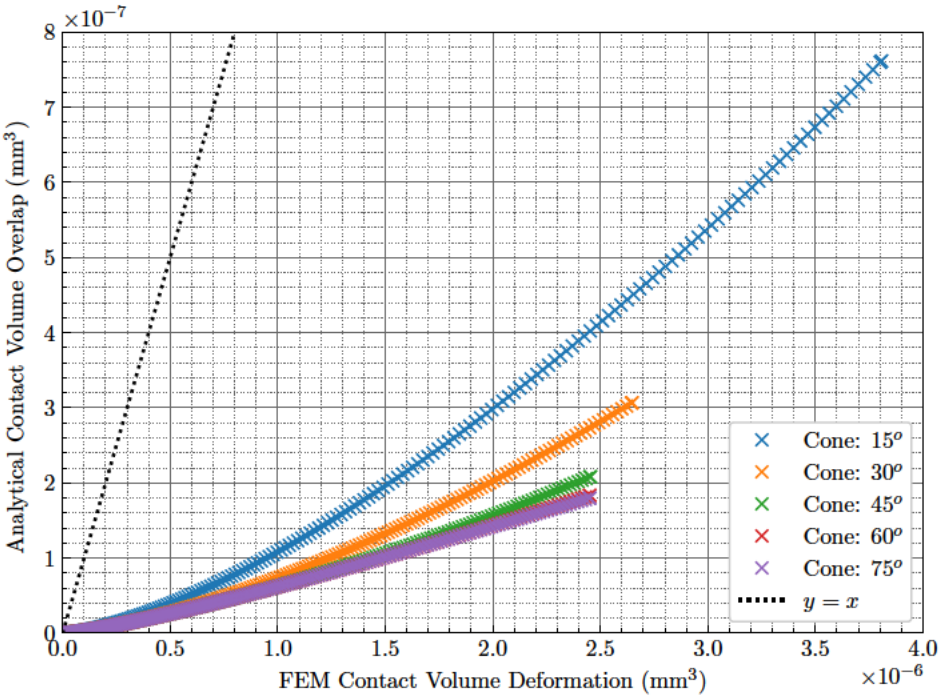

(a) Poisson's ratio = 0

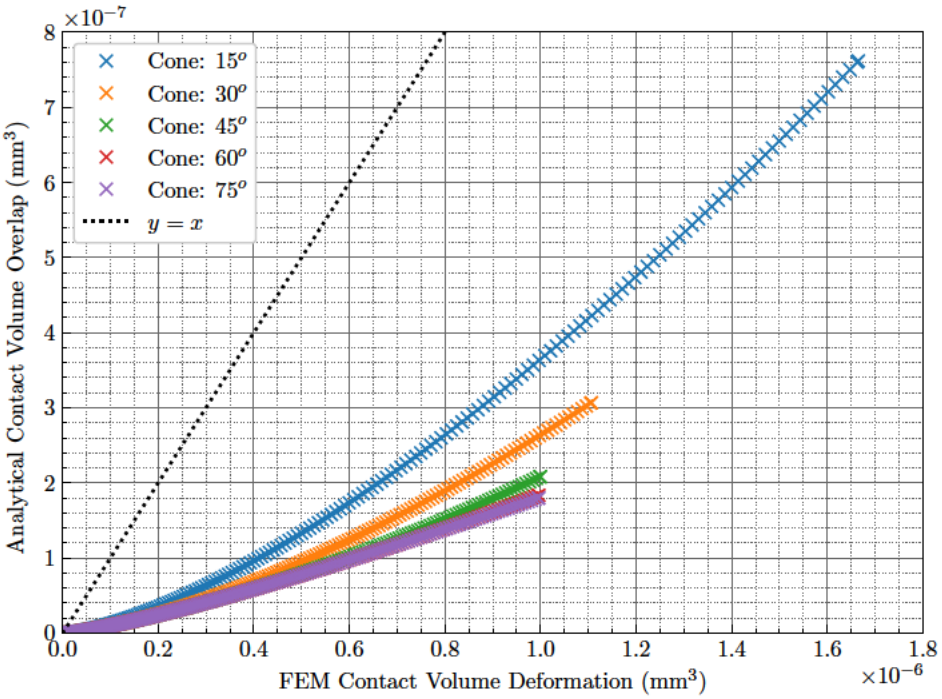

(b) Poisson's ratio = 0.3

Figure 5.9: The analytical contact volume overlap was plotted against the volumetric deformation obtained from FEA. The dotted line represents the $y = x$ line along which ideally all curves would lie.

using the conical indenters was plotted against the FEM-obtained volumetric deformation in Figures 5.9a and 5.9b for the materials with Poisson's ratios of $\nu = 0$ and $\nu = 0.3$, respectively. Ideally, there would be a 1:1 relation with all curves lying on top of a $y = x$ line. The $y = x$ line was also plotted to showcase how far off the deviation of their actual correlation is.

5.3.2.1 LVB comparison with conventional Linear contact model

To represent a more practical scenario for use in DEM, the force obtained with LVB using the analytical volume was compared with the relevant force responses in the conical indentations. The FEA force was included in the comparison as well as the ones obtained from the conventional linear model and Hertz. This is shown in Figures 5.10a and 5.10b for the materials with Poisson's ratios of $\nu = 0$ and $\nu = 0.3$ respectively. For comparison purposes, only one k value was selected per material, to showcase how the LVB operates. The values of k_{Linear} and k_{LVB} were arbitrarily calibrated to match the FEA force at the 30° conical indenter at 1.5% strain. The values used for the two materials are displayed in Table 5.2.

Table 5.2: k values used for the Conventional Linear CM and LVB for each material in the conical indentations. The k values for both models were calibrated with the force obtained at 1.5% with the 30° conical indenter.

Poisson's ratio	k_{Linear}	k_{LVB}
0	677.44×10^6	34.67×10^3
0.3	709.31×10^6	36.20×10^3

Since the distance overlap at the point of contact does not vary across all the different indenters, the forces obtained from the Hertz model and the conventional Linear model are constant. This makes it hard for any of the distance-based models to accurately predict the force response across the different indenters. In the meantime, as the LVB model is based on the volumetric deformations (or the analytical contact volume overlap in this case), it is the only contact model that produces a force response which is affected by the different indenters.

It is observed that at the small θ_i angles of the conical indenters, where the contact volume overlap is much greater, the LVB model greatly overpredicts the force response beyond strains of 1%. The greatest error is an overprediction of around 116% against the FEA force response. While that is a large overprediction, it is the only contact model that actually reacts to the different volumetric deformations taking place which in fact have a significant effect on the force response as is seen by the FEA results.

Conversely, if the LVB model is to be used for cases where there are no excessive volumetric deformations and k_{LVB} calibrated with those cases in mind, it can prove to be a much better alternative than the conventional linear model which is currently used in those situations. The LVB predicted force response actually follows a curve which is closer to the FEA force response. This can be further seen in the uniaxial compressions of a sphere between two flat plates.

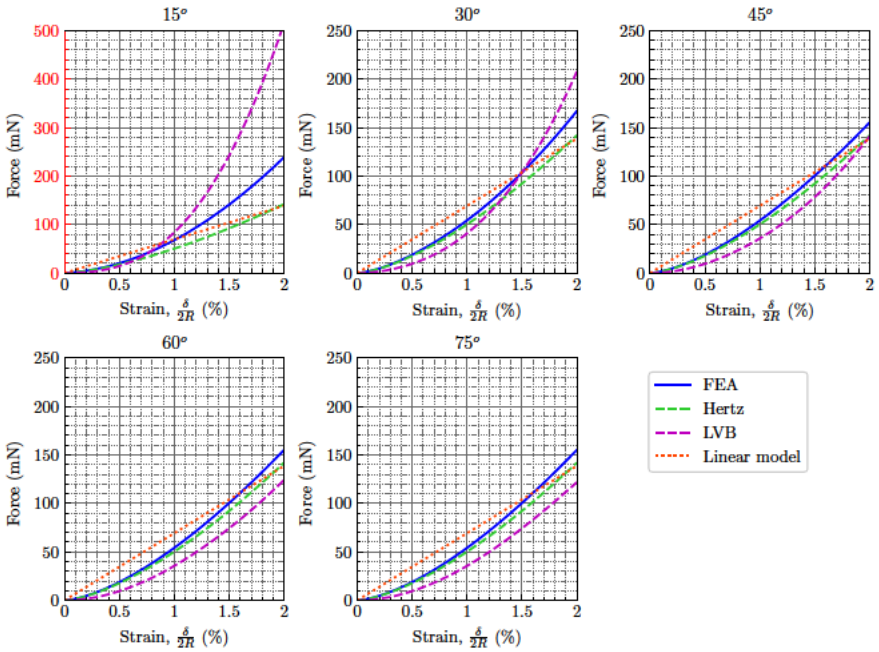

(a) Poisson's ratio = 0

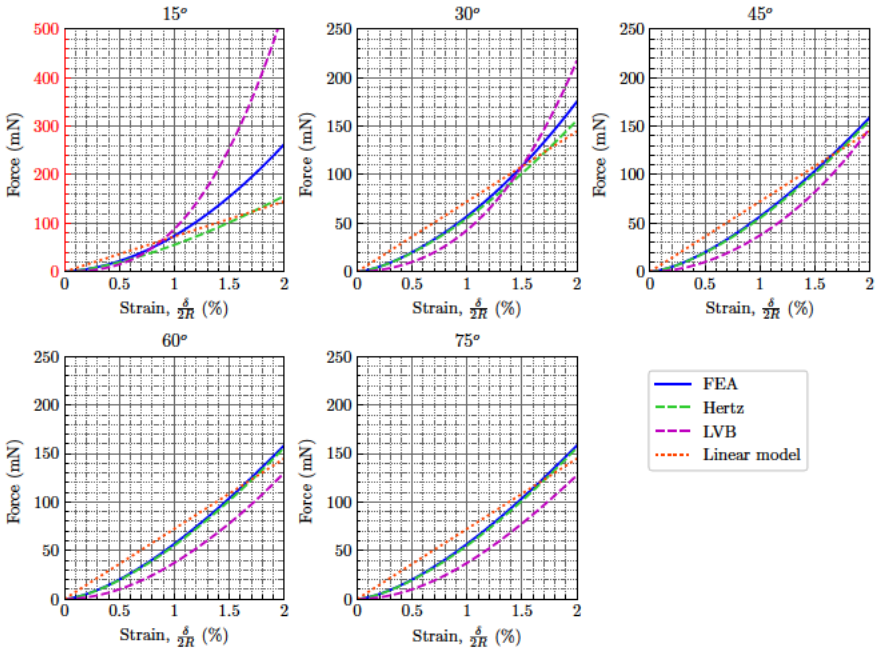

(b) Poisson's ratio = 0.3

Figure 5.10: Conical indentation force responses. Comparison between LVB and the Conventional Linear CM. The y-axis of the 15° conical indenter plot was coloured red to highlight the different scale used. The relative k values are shown in Table 5.2.

Uniaxial compressions of a sphere revisited Data from the FEA performed in Chapter 3 was used to evaluate the applicability of the LVB model (using the analytical contact volume overlap) and the conventional Linear model in more standard situations where spheres are in contact with a rigid wall. This analysis was performed for the material with Poisson's ratio of $\nu = 0.3$. Figure 5.11 showcases the force responses obtained. The force responses obtained from Hertz and Tatara were also included. Furthermore the errors obtained from all the models are displayed in Figure 5.12. This further establishes the argument that the LVB model should be used as an alternative to the conventional Linear model, at least for particle shapes were the analytical contact volume overlap is not too difficult to obtain.

An additional theoretical argument can be made for the LVB model for spheres when the force–deformation relationships are considered in the Hertzian contact model, the Linear contact model and the LVB contact model:

$$\begin{aligned} \text{Hertz} &: F \propto \delta^{3/2} \\ \text{Linear} &: F \propto \delta \\ \text{LVB} &: F \propto V_{\text{Spherical cap}} \Rightarrow F \propto \delta^2 (3r - \delta) \end{aligned}$$

Considering that Hertz is designed and performs well for spheres at low strains, the Linear CM has an error of order $\delta^{1/2}$ compared to Hertz. For LVB, in the case of a sphere and a flat plate, $\delta \ll r$ in DEM. Therefore, the error obtained is smaller than the Linear contact model's $\delta^{1/2}$ order error compared to Hertz due to the $-\delta^3$ correction.

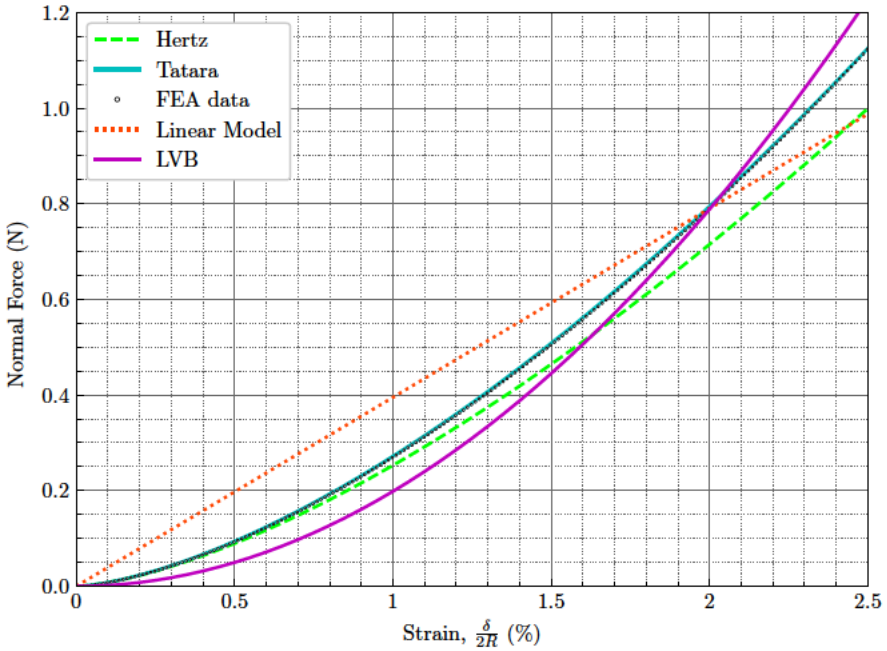

Figure 5.11: Uniaxial compressions of a sphere force responses.

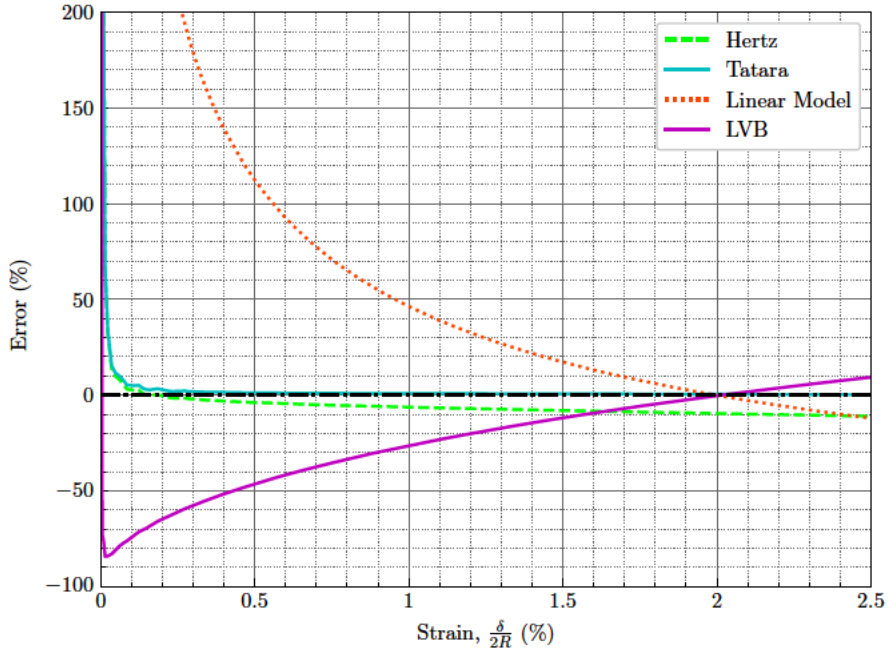

Figure 5.12: Percentage errors obtained from the contact models evaluated against the FEA. The positive errors represent an overprediction of the force response while the negative errors represent an underprediction when compared with the FEA results.

5.4 Summary

In this chapter, two contact models based on the volume of the contact overlap in DEM were evaluated by simulating indentation tests using different shaped indenters in FEM. While in theory Feng's energy-conserving model seems promising, the results obtained reveal that it is impractical. The model's parameters seem to be dependent on shape even though they were expected to only be dependent on material properties, perhaps due to some of the assumptions made for the model's development.

The LVB model on the other hand seems to be a viable alternative to the conventional linear spring model. However, there are still limitations. The analytical contact volume overlap is needed which might be difficult to obtain for complex shaped contacts. It would be ideal if the actual volumetric deformation was available to be used in conjunction with the LVB model rather than just the analytical contact volume overlap as that enhances the accuracy of the model according to results from the FEA. A correlation between the actual volumetric deformation and the analytical contact volume overlap would be beneficial. Considerable future work is needed to develop practical contact models for DEM for which the input parameters depend on material properties and not the detail of the shape at the contact point.

Chapter 6

Influence of the Poisson effect on the stress dependence of the elastic moduli of soil

In this chapter, the application of DEM in soil mechanics is explored, focusing on the elastic moduli of soil, G_0 and K_0, and their dependency on effective confining stress σ'. As mentioned in Section 2.6, experimental findings show that in the $G_0 \propto \sigma'^m$ relationship, the exponent $m \approx 1/2$ whereas Effective Medium Theory (EMT) predicts $m \approx 1/3$ at high confining stresses. One mechanism that seems to be linked to this discrepancy is contact asperities as proposed by Goddard (1990). Rough-surface DEM contact models — which consider contact asperities — show better alignment with experimental data, especially at low-to-moderate confining stresses (Yimsiri & Soga, 2000; Otsubo *et al.*, 2017). However, at high confining stresses, the 'small deformations' assumption in Hertzian mechanics becomes questionable, indicating a need for further refinement in order to obtain a realistic stress dependence of the elastic moduli in DEM simulations.

The hypothesis examined in this chapter is that the omission of the lateral extension term developed by Tatara contributes to the discrepancy between $m \approx 1/2$ for real soil and $m \approx 1/3$ in numerical analyses, particularly at high confining stresses. The Poisson effect is expected to complement the asperity deformation mechanism captured by rough-surface contact models in DEM: as the confining stress increases, asperities deform and their importance reduces whereas one would expect the Poisson effect to become increasingly influential. The Finite Element Method (FEM) is used to investigate this hypothesis. Firstly, the simulation approach is verified by comparing with the analytical solution of Tatara (1991) for uniaxial compression of a single unbreakable sphere. Then the sphere is isotropically compressed between six plates and the relationship between the small-strain bulk modulus, K_0, and the effective confining stress is explored. This takes the form $K_0 \propto \sigma'^n$, distinguishing between G_0 and K_0 relationships using

exponents m and n, respectively.

6.1 Verification by uniaxial compression

Following the methodology described in Chapter 3, the commercial package Abaqus FEA (Dassault Systèmes, 2015) was used to quasi-statically compress a sphere between two rigid plates as shown schematically in Figure 6.1. The particle and material parameters match Yimsiri & Soga (2000): radius R of 1 mm, density of 2,600 kg/m^3, Young's modulus E of 69.6 GPa and Poisson's ratio ν of 0.2. The elasticity is modelled using the inbuilt routine in Abaqus for isotropic materials which requires only E and ν. An octant of the entire sphere was simulated using three planes of symmetry and 15,484 'C3D20R' (20-node quadratic brick, reduced integration) elements as shown in Figure 6.2. The octant mesh was refined in three regions, even though there is only one contact point for uniaxial compression, as the same mesh was used for the isotropic compression simulations with three contact points. The sphere was compressed up to 5% average strain: a common heuristic for the maximum permissible contact overlap between spheres in DEM simulations. The results of this simulation are compared with the analytical solutions of Hertz (1882) and Tatara (1991) given in Equation 2.3 and Equations 2.9–2.11 respectively. The comparison with the latter allows the reliability of these implicit simulations to be verified against an analytical solution developed for non-infinitesimal strains.

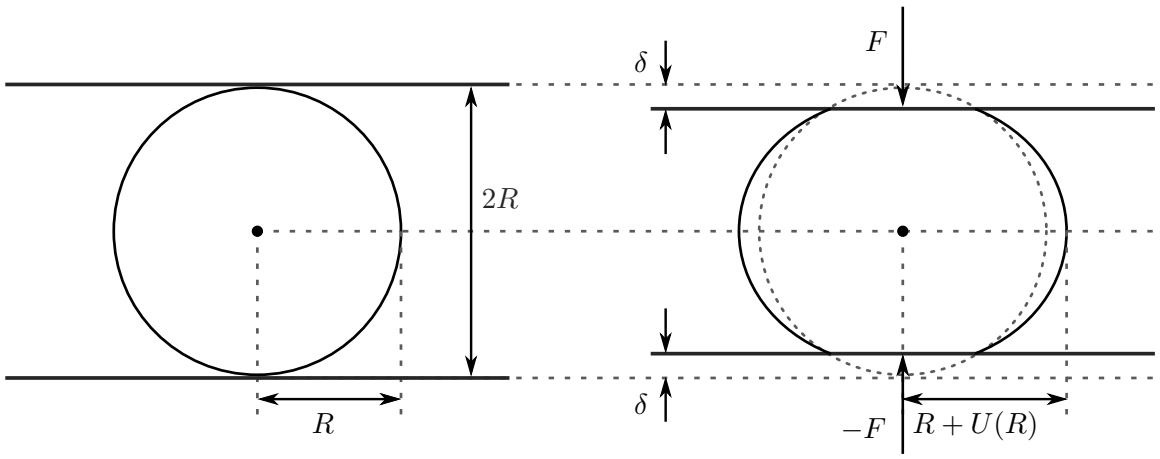

Figure 6.1: Schematic showing a single sphere before (left) and after (right) uniaxial compression between rigid plates. The lateral extension at the central diameter of the sphere is represented by $U(R)$. Deformations have been exaggerated to enhance clarity of representation.

The lateral extension at the central diameter of the sphere, $U(R)$, is zero for a Hertzian sphere. For the linear elasticity case, $U(R)$ is given by Tatara (1991) as:

$$U(R) = \frac{F(1+\nu)}{\pi E R}\left[\frac{1}{2\sqrt{2}} - (1-2\nu)\left(1 - \frac{1}{\sqrt{2}}\right)\right] \tag{6.1}$$

For real soils with $\nu > 0$, $U(R) > 0$ according to Equation 6.1. $U(R)$ is obtained from the FEM

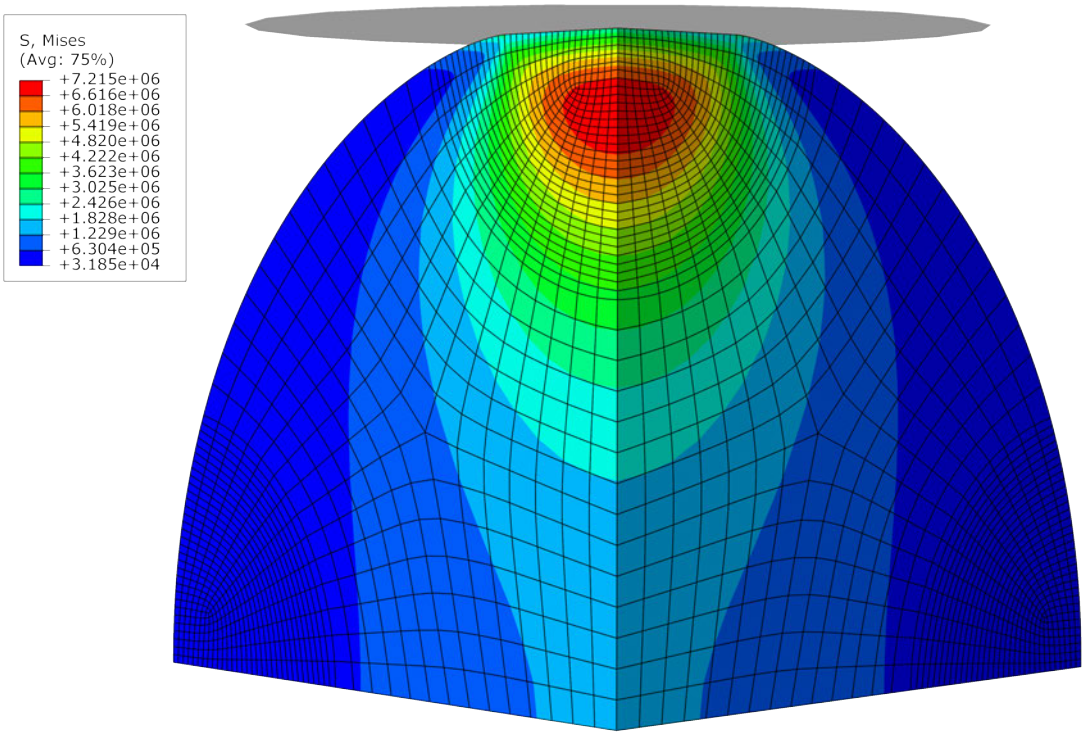

Figure 6.2: The octant of the sphere simulated in Abaqus FEA at a total compressive strain of 5%. The contours represent the von Mises stress measured in Pa.

data at any strain by identifying the subset of nodes that form the quadrant arc around the base of the sphere octant and finding the average radial distance for that subset.

Both F and $U(R)$ are plotted against the total compressive strain on the granule in Figure 6.3. The disparity between the FEM force data and the Tatara analytical solution stabilises at around 2% at strains beyond 2%. This is considered acceptable for the purposes of verification. By contrast, the disparity between the Hertz and Tatara forces increases monotonically with strain, in both absolute and relative terms, as the lateral extension effect becomes significant: the disparity increases in magnitude from 5% at 1% strain to 9% at 3% strain to 11.7% at 5% strain.

While the FEM simulation captures Tatara's analytical F very well, the same is not true of $U(R)$. Figure 6.3b shows that $U(R)$ is overestimated by a factor of around 2 in the simulation compared to Equation 6.1. When Tatara *et al.* (1991) compared their theory with experiments for uniaxial compression of a rubber sphere, they found a good agreement for both F (error $\leq 4\%$) and $U(R)$ (error $\leq 16\%$) up to 40% strain applied (per contact), implying that the disparity in Figure 6.3b is attributable to the FEM rather than a deficiency of the analytical prediction. Additional simulations show that the margin of the overestimate in $U(R)$ depends on the Poisson's ratio – for example, fourfold at $\nu = 0.01$. While the Poisson effect is apparent in FEM, which represents an improvement on Hertzian mechanics for which $U(R) = 0$, it is exaggerated. For the FEM simulations of isotropic compression, the Poisson effect is also likely to be exaggerated.

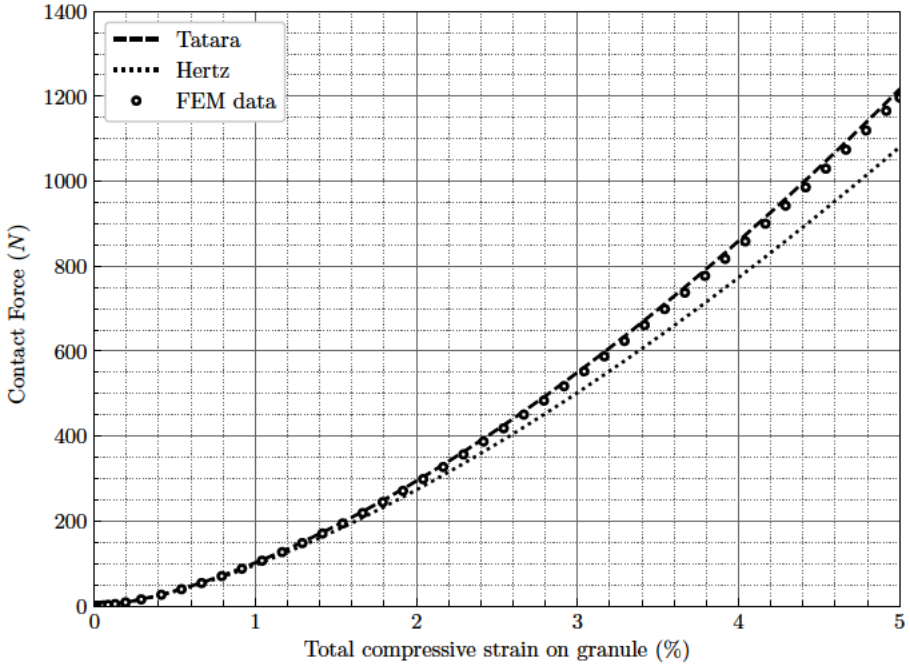

(a)

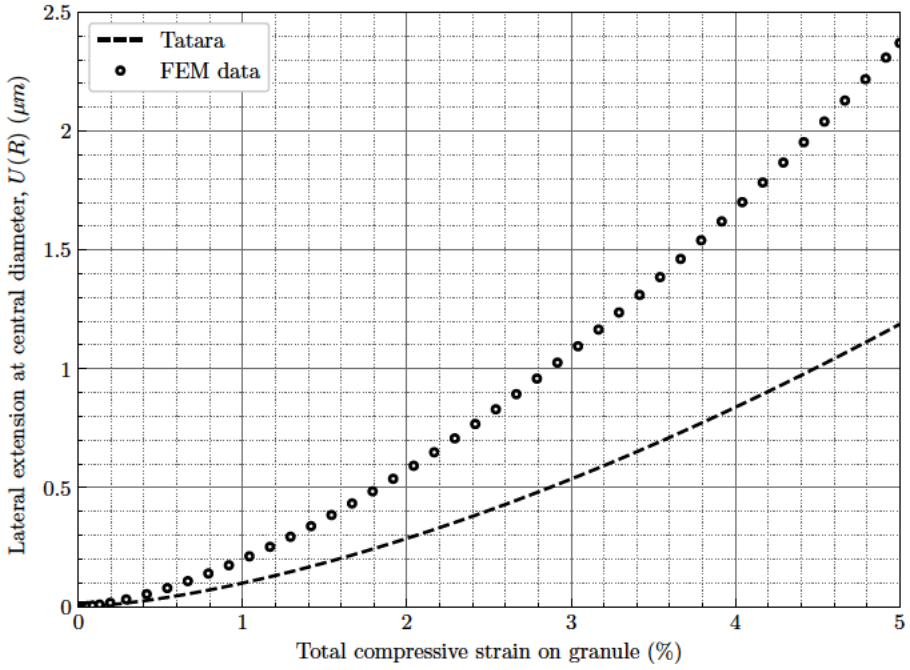

(b)

Figure 6.3: Relationships between (a) contact force, F, and total compressive strain on granule and (b) lateral extension at the central diameter of the sphere, $U(R)$, and total compressive strain on granule for a single sphere subjected to uniaxial compression in FEM, compared with analytical curves of Hertz (1882) and Tatara (1991).

6.2 Isotropic compression and data analysis

Having established the capacity of FEM to predict the contact force for uniaxial compression and display the Poisson effect, albeit more pronounced than the analytical solution of Tatara (1991) indicates, isotropic compression of a sphere between six plates was simulated. The same parameters and octant of a sphere are used as for the uniaxial compression (Figure 6.4) except the Poisson's ratio, ν, is varied from 0.01 to 0.49. Data was exported from the simulations at logarithmically spaced intervals. The data included the displacement of each plate from its initial position, δ, and the force on each plate. The displacements are identical for each plate; the forces, which are multiplied by four to give the forces for a complete sphere, F, are the same within a small margin of numerical error.

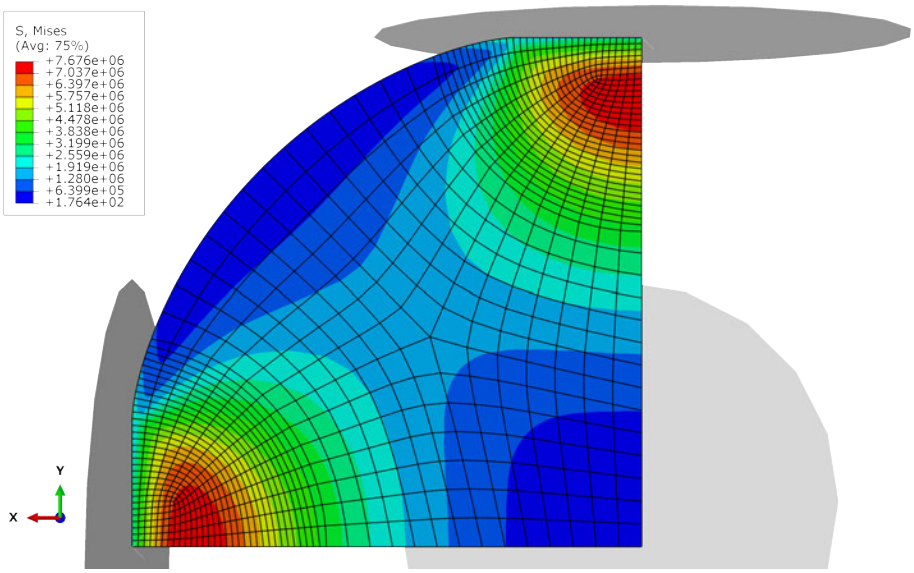

Figure 6.4: Octant of spherical granule being isotropically compressed. The contours represent the von Mises stress measured in Pa when the maximum confining stress is applied.

The average stress along each rigid boundary is calculated as:

$$\overline{\sigma}_b = \frac{F}{(2R - 2\delta)^2} \tag{6.2}$$

The denominator represents the surface area of each rigid boundary enclosing the sphere. Since these average stresses are the same for each boundary, the effective confining stress $\sigma' = \overline{\sigma}_b$. The elastic bulk modulus K_0 is computed as:

$$K_0 = \frac{\delta\sigma'}{\delta\epsilon_v} \tag{6.3}$$

where $\delta\sigma'$ is the increment of effective confining stress and $\delta\epsilon_v$ is the logarithmic volumetric strain increment – that is, the incremental change in volume enclosed by the boundaries divided

by the current enclosed volume.

Elastic bulk moduli are also calculated for a single Hertzian sphere compressed between rigid plates following Equations 6.2–6.3. At any effective confining stress σ', $\delta\sigma'$ is fixed at a small value of 100 Pa and $\delta\epsilon_v$ is computed at stresses of $\sigma' \pm 50$ Pa. The corresponding plate displacements, δ, are obtained by substituting Equation 2.3 into Equation 6.2 and solving numerically.

6.3 Results and discussion

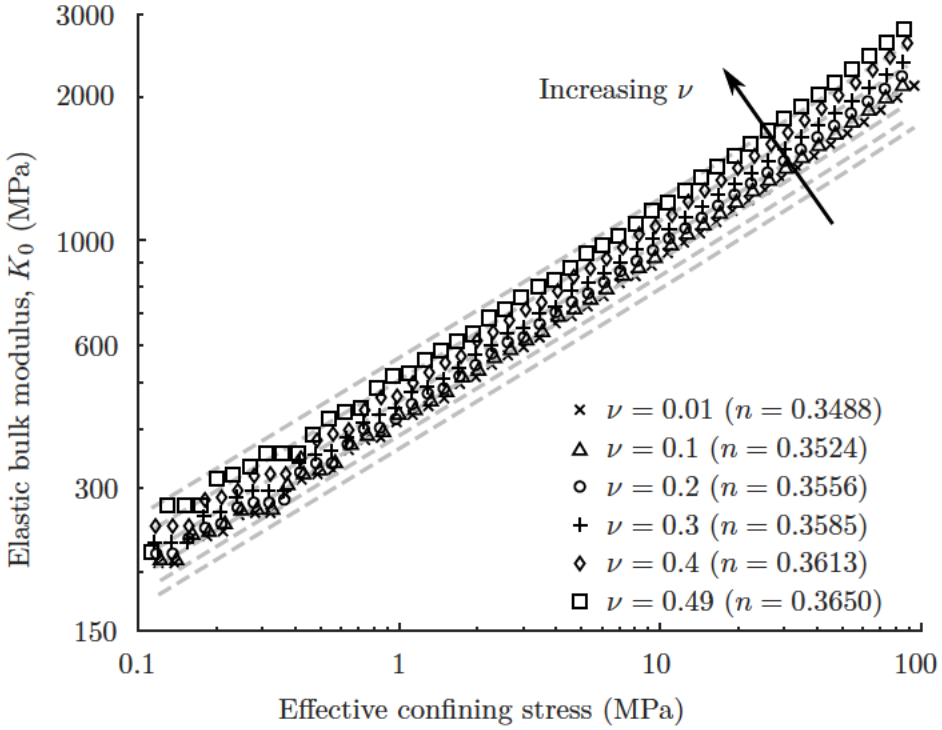

Figure 6.5: Elastic bulk modulus, K_0, against effective confining stress, σ', at six Poisson's ratios, ν. The FEM data is shown using black markers; results for a Hertzian sphere are shown as grey dashed lines. The slopes of the best-fit linear regressions to the FEM data, n, are provided in the legend.

Figure 6.5 shows the elastic (small-strain) bulk modulus, K_0, against effective confining stress, σ', at Poisson's ratios, ν, of 0.01, 0.1, 0.2, 0.3, 0.4 and 0.49. The range of confining pressures considered, 100 kPa–100 MPa, matches that in Yimsiri & Soga (2000). Linear regressions fit the data very well but are not displayed on Figure 6.5 for clarity: the coefficients of determination $R^2 > 0.9975$ for the FEM data, with the lowest R^2 corresponding to the largest Poisson's ratio of 0.49. $R^2 > 0.9999$ for the Hertzian sphere regressions.

As ν increases, so too does K_0 at a fixed σ' for both the FEM and perfect Hertzian spheres. The slopes of the linear regressions, n, increase systematically with increasing ν for the FEM data, from 0.3488 at $\nu = 0.01$ to 0.3650 at $\nu = 0.49$. This is in line with the proposed hypothesis; as the Poisson's ratio increases, the particle expands more due to the increased Poisson effect

and so will behave more stiffly when subjected to isotropic compression. The FEM simulations capture, and in fact overemphasise, the 'lateral extension' effect (Figure 6.3b). For the Hertzian spheres, this effect is absent and n varies negligibly from 0.3388 at $\nu = 0.01$ to 0.3367 at $\nu = 0.49$. Although close, these slopes are not exactly $1/3$ because of significant sphere deformations, which violate a key assumption of Hertzian theory. At $\sigma' = 100$ MPa, δ ranges from 18.6 µm ($\nu = 0.49$) to 28.6 µm ($\nu = 0.01$): equivalent to 1.86%–2.86% of the sphere's radius. As $\delta \to 0$, $n \to 1/3$ for the Hertzian spheres.

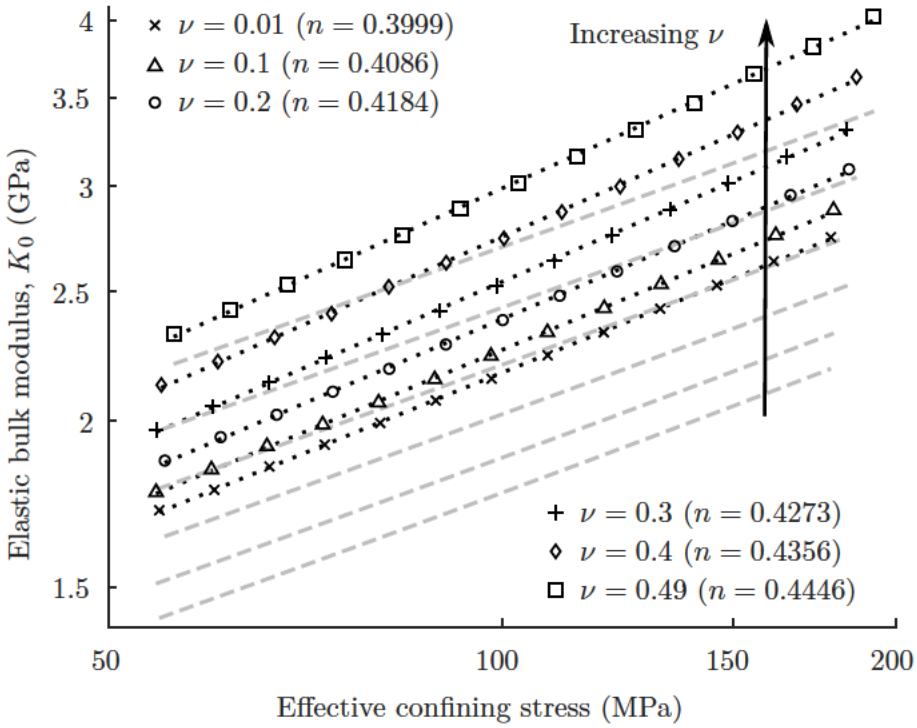

Figure 6.6: The elastic bulk modulus, K_0, against the effective confining stresses, σ', at Poisson's ratios, ν, of 0.01, 0.1, 0.2, 0.3, 0.4 and 0.49 for effective confining stresses of 50 MPa–200 MPa. Black dotted linear regressions are shown for the FEM data (black markers). As for Figure 6.5, results for a Hertzian sphere are shown as grey dashed lines

.

The Poisson effect is expected to become more pronounced at large strains. This is confirmed in Figure 6.6 in which the range of effective confining stresses has been increased to 50 MPa–200 MPa compared to Figure 6.5. On Figure 6.6, as for Figure 6.5, n values for the FEM data increase with increasing ν: from 0.3999 at $\nu = 0.01$ to 0.4446 at $\nu = 0.49$. For all of these regressions, $R^2 > 0.9995$. The equivalent Hertzian spheres significantly underpredict K_0 at these high confining stresses and the regressions have much smaller slopes, ranging from $n = 0.3648$ at $\nu = 0.01$ to $n = 0.3546$ at $\nu = 0.49$.

For real soils, confining stresses of 50 MPa–200 MPa would cause enormous particle crushing even for silica sands (Altuhafi & Coop, 2011; Hanley *et al.*, 2015). Asperities on particle surfaces would certainly be crushed. As a result, rough-surface contact models in DEM analyses of

unbreakable spheres become ineffectual at such high stresses. Therefore, the inclusion of the Poisson effect would be a viable option to give a reasonable stress dependency of the elastic moduli. It is questionable, however, whether one should run DEM simulations at such large stresses without including a particle crushing mechanism. At lower stresses, the Poisson effect has a negligible effect; the two mechanisms discussed by Goddard (1990) and Mcdowell & Bolton (2001) are far more influential. Recalling that the Poisson effect is overestimated in these FEM simulations, based on a comparison with the analytical solution of Tatara (1991) for uniaxial compression (Figure 6.3b), its effect at low stresses is even less than indicated by Figure 6.5. The adoption of rough-surface contact models – for example, Otsubo *et al.* (2017), remains the most justifiable way of matching experimental measurements using DEM simulations.

While this chapter has focused on a single spherical particle, the results are relevant for multi-particle assemblies, even randomly packed ones. The behaviour of a multi-particle assembly is a direct consequence of the behaviours of each individual particle comprising the assembly. Each particle in an idealised cubic packing has an identical stress state so any single particle is representative. Random packings of smooth particles have comparable exponents in the $G_0 \propto \sigma'^m$ relationship (Otsubo *et al.*, 2017). It is also noted that a strictly elastic soil does not allow for sliding at interparticle contacts or buckling of force chains (Mcdowell & Bolton, 2001). This indicates that contact mechanics is the critical factor for soil elasticity rather than the evolving soil fabric.

6.4 Conclusions

A novel hypothesis is presented and explored in this chapter regarding the dependence of the elastic moduli of soil on the effective confining stress, σ'. For real soils, the $G_0 \propto \sigma'^m$ relationship typically has an exponent $m \approx 1/2$; for Hertzian spheres, $m \approx 1/3$. It was hypothesised that the omission of the Poisson effect in Hertzian mechanics contributes to the discrepancy between these exponents, particularly at high confining stresses. By simulating a single spherical particle in FEM, it is observed that the Poisson effect has a measurable but very limited influence at low to moderate confining stresses. Using simulation parameters appropriate for a silica sand, the Poisson effect became significant only at confining stresses on the order of 100 MPa. Consequently, rough-surface contact models are far more effective for obtaining a realistic stress dependence of the elastic moduli in DEM simulations.

Chapter 7

Conclusions & Future work

The main objective of this work was to investigate contact models for DEM simulations of non-spherical particles. In order to perform the investigation, a framework was developed using FEM that allowed the evaluation of various DEM contact models in different situations.

7.1 Conclusions

Quantifying the errors in Multi-Sphere DEM

After verifying the FEM models used in Chapter 3, the errors present when the Multi-Spherical (MS) approach is used to represent non-spherical particles were identified and quantified for the exemplar shape of spherocylinders in Chapter 4. The two types of errors identified were: (i) the contact model error arising from adopting a contact model suitable for individual spheres and (ii) the shape approximation error arising from modelling a specific desired particle shape using a finite number of spheres.

Uniaxial compressions of spherocylindrical rods as well as collisions between identical spherocylinders were performed in FEM at different angles. In order to quantify the contact model error, a comparison was performed between the force responses of two-sphere and three-sphere rods obtained in the FEA and the force responses predicted by the various DEM contact models being evaluated.

It was observed that the contact model errors are mainly driven by the strains applied when the constituent spheres of the MS rods overlap by less than 60%. At greater sphere overlaps, the sphere overlap percentage becomes the main driving force of the errors almost completely overshadowing the effect strain has on those errors. For the angled collisions, the contact model error seems to be decreasing in absolute terms as the collision angle increases. This is possibly due to the contacts more closely resembling those between two individual spheres.

The quantification of the shape approximation error was performed fully within the FEM regime. The force responses of the perfect spherocylinders were compared to those of MS rods

with varying numbers of constituent spheres. The shape approximation error can essentially be eradicated by using a very large number of constituent spheres to get an accurate representation of the desired granule shape. Hence, given the importance of having an accurate shape representation for contact detection — even though that was out of the scope of this thesis — the optimal rod configuration when using the MS approach seems to be a MS rod with sphere overlaps around 60%. While the error quantification in this work was focused on spherocylindrical particles, results using this exemplar shape are expected to be qualitatively applicable to any MS system.

Contact: Depth of Penetration or Volume Overlap

In Chapter 5, two contact models (Feng and LVB) based on the volume of the contact overlap in DEM were evaluated by simulating indentation tests on a spherical granule using different shaped indenters in FEM. While in theory Feng's energy-conserving model seems promising, the results obtained reveal that it is impractical. The model's parameters seem to be dependent on shape even though they were expected to only be dependent on material properties, perhaps due to some of the assumptions made for the model's development.

The LVB model on the other hand seems to be a viable alternative to the conventional linear spring model. However, there are still certain limitations. The analytical contact volume overlap is needed which might be difficult to obtain for complex shaped contacts. It would be ideal if the actual volumetric deformation was available to be used in conjunction with the LVB model rather than just the analytical contact volume overlap as that enhances the accuracy of the model according to results from the FEA.

Influence of the Poisson effect on the stress dependence of the elastic moduli of soil

In Chapter 6, it was examined whether the omission of the Poisson effect in Hertzian spheres contributes to the inability of smooth-sphere DEM simulations to correctly capture the stress dependence of the elastic moduli of soil. This was done by isotropically compressing a spherical granule of silica sand using FEM. At low-to-moderate confining stresses the Poisson effect had a measurable but very limited influence. It was observed that the Poisson effect became significant only at confining stresses on the order of 100 MPa. Thus, at lower stresses, rough-surface contact models remain the most justifiable way to match the stress–stiffness response measured in laboratory testing using DEM simulations.

7.2 Recommendations and further research

Based on the present work, some recommendations as well as a non-exhaustive list of areas for future research is provided below.

Recommendations

- When using the MS approach to represent non-spherical particles in DEM simulations, avoid having the overlaps of the constituent spheres' exceed 60% as that greatly increases the errors regardless of the type of contact model used (based on the currently established contact models).
- If the contact volume overlap can be obtained at an acceptable computational cost, start using the LVB contact model instead of the conventional Linear model as that generally can produce results that better resemble reality compared to the Linear model.

Future research

- Apply the same framework developed in Chapter 4 to quantify errors when: (i) spherocylindrical rods have different aspect ratios, (ii) different materials are used, (iii) different shapes are used or (iv) simply compare with different contact models that may be in development.
- Some correction factors based on the contour plots obtained could potentially be applied to both the contact model error as well as the shape approximation error to further improve the accuracy of using the MS approach in non-spherical DEM simulations.
- The force response of a single sphere when uniaxially compressed is essentially the same as that of a three-sphere rod when multiplied by 3. The force response of a perfect cylinder when uniaxially compressed along its length is the same as that of a perfect spherocylinder minus the force response of a single sphere. If there is a way to correlate the force response of a MS rod to that of the perfect spherocylinder with the same aspect ratio, it would effectively create a way to predict the force response of a cylinder of any length from that of a sphere that has the same radius. While this would only be applicable for uniaxial compressions along the length of the cylinders, it is something that could be expanded further from spherocylinders to 3D 'flat' plates to cuboids. This could potentially be applied to obtain the force response of an arbitrary shaped particle just from knowing the force response of a sphere of the same material.
- Find a way to relate the analytical contact volume overlap to either the actual volumetric deformations or perhaps the ones obtained through FEA. That would greatly increase the accuracy of the LVB model.
- Relate k_{LVB} to physical properties (Young's modulus, Poisson's ratio) similar to how other contact models operate.
- Considerable future work is needed to develop practical contact models for DEM for which the input parameters depend on material properties and not the detail of the shape at the contact point.

- Perhaps Machine Learning can be applied similar to Lai *et al.* (2022) but instead of utilising it for contact detection, use it to predict the force responses of arbitrarily shaped particles. One way this could be achieved is by performing a number of particle collisions with FEM using various shapes, training a model based on the force responses obtained and, using the trained model, predict the forces resulting from different collision scenarios within a DEM simulation.

Nomenclature

δ	Deformation (or DEM overlap) of a granule in contact
$\delta\epsilon_v$	Logarithmic volumetric strain increment
$\delta\sigma'$	Increment of effective confining stress
δ_{ij}	Kronecker delta
$\mathbf{I}^{\text{cluster}}$	MS cluster moments of inertia about a local Cartesian axis centered at the cluster centroid
$\mathbf{I}^s$	Inertia relative to the sphere local Cartesian axis
$\mathbf{x}^{\text{cluster}}$	Vector describing the MS cluster centroid
$\mathbf{x}^s$	Vector describing the constituent sphere centroid
ν	Poisson's ratio
$\overline{\sigma}_b$	Average stress along each rigid boundary
σ'	Effective confining stress
a	Radius of circular contact area
c	Function of a in the Tatara set of equations
D	Diameter of constituent spheres
E	Elasticity/Young's modulus
E^*	Effective elasticity
F	Normal contact force
G_0	Elastic (small-strain) shear modulus
K	Bulk modulus

k	Constant index of normal stiffness
K_0	Elastic (small-strain) bulk modulus
L	Length between centers of constituent spheres
m	Constant in Feng's contact model
m	Exponent in $G_0 - \sigma'$ relationship
m^s	Mass of constituent sphere
n	Exponent in $K_0 - \sigma'$ relationship
N_s	Number of spheres in MS cluster
R	Radius of sphere/rod
R^*	Effective radius
S	Contact surface area (scalar)
$U(R)$	Lateral extension at central diameter of sphere
V_c	Volume of contact overlap
AMS	Advanced Multi-Sphere
CFD	Computational Fluid Dynamics
CM	Contact Model
DEM	Discrete-Element Method/Modelling
DoF	Degrees of Freedom
FEM	Finite Element Method/Modelling
FLR	Fixed-Length Rod
FSR	Fixed-Sphere Rods
LVB	Linear Volume-Based
MFM	Modified Hertzian Force Model
MS	Multi-Spherical
PoC	Point of Contact
PSC	Perfect Spherocylinder

Reference List

Agnolin, I. & Roux, J.-N. (2007). Internal states of model isotropic granular packings. III. Elastic properties. *Physical Review E* **76**, No. 6, 061304, doi: 10.1103/PhysRevE.76.061304.

Ai, J., Chen, J.-F., Rotter, J. M. & Ooi, J. Y. (2011). Assessment of rolling resistance models in discrete element simulations. *Powder Technology* **206**, No. 3, 269–282, doi: 10.1016/j.powtec.2010.09.030.

Altuhafi, F. N. & Coop, M. R. (2011). The effect of mode of loading on particle-scale damage. *Soils and Foundations* **51**, No. 5, 849–856, doi: 10.3208/sandf.51.849.

Arifuzzaman, S. M., Dong, K., Hou, Q., Zhu, H. & Zeng, Q. (2020). Explicit contact force model for superellipses by Fourier transform and application to superellipse packing. *Powder Technology* **361**, 112–123, doi: 10.1016/j.powtec.2019.10.018.

Barr (1981). Superquadrics and Angle-Preserving Transformations. *IEEE Computer Graphics and Applications* **1**, No. 1, 11–23, doi: 10.1109/MCG.1981.1673799.

Berry, N., Zhang, Y. & Haeri, S. (2021). Lees-Edwards boundary conditions for the multi-sphere discrete element method. *Powder Technology* **389**, 292–308, doi: 10.1016/j.powtec.2021.05.025.

Boon, C. W., Houlsby, G. T. & Utili, S. (2013). A new contact detection algorithm for three-dimensional non-spherical particles. *Powder Technology* **248**, 94–102, doi: 10.1016/j.powtec.2012.12.040.

Cantor, D., Cárdenas-Barrantes, M., Preechawuttipong, I., Renouf, M. & Azéma, E. (2021). Bulk modulus of soft particle assemblies under compression. *EPJ Web Conf.: Powders & Grains 2021* **249**, 14014, doi: 10.1051/epjconf/202124914014.

Capozza, R. & Hanley, K. J. (2021). A hierarchical, spherical harmonic-based approach to simulate abradable, irregularly shaped particles in DEM. *Powder Technology* **378**, 528–537, doi: 10.1016/j.powtec.2020.10.015.

Cavarretta, I., Coop, M. & O'Sullivan, C. (2010). The influence of particle characteristics on the behaviour of coarse grained soils. *Géotechnique* **60**, No. 6, 413–423, doi: 10.1680/geot.2010.60.6.413.

Chang, C. S., Misra, A. & Sundaram, S. S. (1991). Properties of granular packings under low amplitude cyclic loading. *Soil Dynamics and Earthquake Engng* **10**, No. 4, 201–211, doi: 10.1016/0267-7261(91)90034-W.

Chen, X., Wang, L. G., Morrissey, J. P. & Ooi, J. Y. (2022). DEM simulations of agglomerates impact breakage using Timoshenko beam bond model. *Granular Matter* **24**, No. 3, 74, doi: 10.1007/s10035-022-01231-9.

Cheng, Y. P., Nakata, Y. & Bolton, M. D. (2003). Discrete element simulation of crushable soil. *Géotechnique* **53**, No. 7, 633–641, doi: 10.1680/geot.2003.53.7.633.

Cleary, P. W. (2004). Large scale industrial DEM modelling. *Engineering Computations* **21**, No. 2/3/4, 169–204, doi: 10.1108/02644400410519730.

Cleary, P. W. & Sawley, M. L. (2002). DEM modelling of industrial granular flows: 3D case studies and the effect of particle shape on hopper discharge. *Applied Mathematical Modelling* **26**, No. 2, 89–111, doi: 10.1016/S0307-904X(01)00050-6.

Constandinou, S. & Hanley, K. J. (2022). Influence of the Poisson effect on the stress dependence of the elastic moduli of soil. *Géotechnique Letters* **12**, No. 1, 80–84, doi: 10.1680/jgele.21.00135.

Cundall, P. A. & Strack, O. D. L. (1979). A discrete numerical model for granular assemblies. *Géotechnique* **29**, No. 1, 47–65, doi: 10.1680/geot.1979.29.1.47.

Das, N., Giordano, P., Barrot, D., Mandayam, S., Sukumaran, B. & Ashmawy, A. K. (2008). Discrete Element Modeling And Shape Characterization of Realistic Granular Shapes. In *The Eighteenth International Offshore and Polar Engineering Conference*, OnePetro, pp. 525–533.

Dassault Systèmes (2015). Abaqus/CAE user's manual, version 2016. Simulia Corp.

Davis, A. D., West, B. A., Frisch, N. J., O'Connor, D. T. & Parno, M. (2021). ParticLS: Object-oriented software for discrete element methods and peridynamics. *Computational particle mechanics* , 1–13doi: 10.1007/s40571-021-00392-3.

DCS Computing (2021). Aspherix®. DCS Computing.

DEM Solutions Ltd. (2019). EDEM 2019.1 user guide.

Dintwa, E., Tijskens, E. & Ramon, H. (2008). On the accuracy of the Hertz model to describe the normal contact of soft elastic spheres. *Granular Matter* **10**, No. 3, 209–221, doi: 10.1007/s10035-007-0078-7.

Duffy, J. & Mindlin, R. D. (1957). Stress–strain relations and vibrations of a granular medium. *J. Appl. Mech., ASME* **24**, No. 4, 585–593, doi: 10.1115/1.4011605.

Eliáš, J. (2014). Simulation of railway ballast using crushable polyhedral particles. *Powder Technology* **264**, 458–465, doi: 10.1016/j.powtec.2014.05.052.

England, A. (1971). On stress singularities in linear elasticity. *International Journal of Engineering Science* **9**, No. 6, 571–585, doi: 10.1016/0020-7225(71)90039-5.

European Cooperation in Science and Technology (2023). Memorandum of Understanding for the implementation of the COST Action "Open Network on DEM Simulations" (ON-DEM) CA22132.

Favier, J. F., Abbaspour-Fard, M. H. & Kremmer, M. (2001). Modeling Nonspherical Particles Using Multisphere Discrete Elements. *Journal of Engineering Mechanics* **127**, No. 10, 971–977, doi: 10.1061/(ASCE)0733-9399(2001)127:10(971).

Favier, JF., Abbaspour-Fard, M. H., Kremmer, M. & Raji, A. (1999). Shape representation of axi-symmetrical, non-spherical particles in discrete element simulation using multi-element model particles. *Engineering Computations* **16**, No. 4, 467–480, doi: 10.1108/02644409910271894.

Feng, Y. (2021a). A generic energy-conserving discrete element modeling strategy for concave particles represented by surface triangular meshes. *International Journal for Numerical Methods in Engineering* **122**, No. 10, 2581–2597, doi: 10.1002/nme.6633.

Feng, Y., Han, K., Owen, D. & Loughran, J. (2009). On upscaling of discrete element models: Similarity principles. *Engineering Computations* **26**, No. 6, 599–609, doi: 10.1108/02644400910975405.

Feng, Y. T. (2021b). An energy-conserving contact theory for discrete element modelling of arbitrarily shaped particles: Basic framework and general contact model. *Computer Methods in Applied Mechanics and Engineering* **373**, 113454, doi: 10.1016/j.cma.2020.113454.

Feng, Y. T. (2021c). An energy-conserving contact theory for discrete element modelling of arbitrarily shaped particles: Contact volume based model and computational issues. *Computer Methods in Applied Mechanics and Engineering* **373**, 113493, doi: 10.1016/j.cma.2020.113493.

Fraige, F. Y., Langston, P., George Z. Chen & Chen, G. (2008). Distinct element modelling of cubic particle packing and flow. *Powder Technology* **186**, No. 3, 224–240, doi: 10.1016/j.powtec.2007.12.009.

Garcia, X., Latham, J.-P., Xiang, J. & Harrison, J. (2009). A clustered overlapping sphere algorithm to represent real particles in discrete element modelling. *Géotechnique* **59**, No. 9, 779–784, doi: 10.1680/geot.8.T.037.

Ghaboussi, J. & Barbosa, R. (1990). Three-dimensional discrete element method for granular materials. *International Journal for Numerical and Analytical Methods in Geomechanics* **14**, No. 7, 451–472, doi: 10.1002/nag.1610140702.

Giannis, K., Schilde, C., Finke, J. H. & Kwade, A. (2021). Modeling of High-Density Compaction of Pharmaceutical Tablets Using Multi-Contact Discrete Element Method. *Pharmaceutics* **13**, No. 12, 2194, doi: 10.3390/pharmaceutics13122194.

Goddard, J. D. (1990). Nonlinear elasticity and pressure-dependent wave speeds in granular media. *Proc. R. Soc. A: Math., Phys. Engng Sci.* **430**, No. 1878, 105–131, doi: 10.1098/rspa.1990.0083.

Govender, N., Cleary, P. W., Kiani-Oshtorjani, M., Wilke, D. N., Wu, C.-Y. & Kureck, H. (2020). The effect of particle shape on the packed bed effective thermal conductivity based on DEM with polyhedral particles on the GPU. *Chemical Engineering Science* **219**, 115584, doi: 10.1016/j.ces.2020.115584.

Govender, N., Wilke, D. N., Wu, C.-Y., Rajamani, R., Khinast, J. & Glasser, B. J. (2018). Large-scale GPU based DEM modeling of mixing using irregularly shaped particles. *Advanced Powder Technology* **29**, No. 10, 2476–2490, doi: 10.1016/j.apt.2018.06.028.

Guo, Y., Wassgren, C., Curtis, J. S. & Xu, D. (2018). A bonded sphero-cylinder model for the discrete element simulation of elasto-plastic fibers. *Chemical Engineering Science* **175**, 118–129, doi: 10.1016/j.ces.2017.09.029.

Haeri, S. (2017). Optimisation of blade type spreaders for powder bed preparation in Additive Manufacturing using DEM simulations. *Powder Technology* **321**, 94–104, doi: 10.1016/j.powtec.2017.08.011.

Hale, L. C. L. C. (1999). *Principles and techniques for designing precision machines*. Thesis, Massachusetts Institute of Technology.

Hanley, K. J., O'Sullivan, C. & Huang, X. (2015). Particle-scale mechanics of sand crushing in compression and shearing using DEM. *Soils and Foundations* **55**, No. 5, 1100–1112, doi: 10.1016/j.sandf.2015.09.011.

Harkness, J. (2009). Potential particles for the modelling of interlocking media in three dimensions. *International Journal for Numerical Methods in Engineering* **80**, No. 12, 1573–1594, doi: 10.1002/nme.2669.

Harkness, J., Zervos, A., Le Pen, L., Aingaran, S. & Powrie, W. (2016). Discrete element simulation of railway ballast: Modelling cell pressure effects in triaxial tests. *Granular Matter* **18**, No. 3, 65, doi: 10.1007/s10035-016-0660-y.

Hart, R., Cundall, P. A. & Lemos, J. (1988). Formulation of a three-dimensional distinct element model—Part II. Mechanical calculations for motion and interaction of a system composed of many polyhedral blocks. *International Journal of Rock Mechanics and Mining Sciences & Geomechanics Abstracts* **25**, No. 3, 117–125, doi: 10.1016/0148-9062(88)92294-2.

Hertz, H., Jones, D. E. & Schott, G. A. (1896). *Miscellaneous papers*. London: Macmillan, New York, Macmillan and co.

Hertz, H. R. (1882). Über die Beruhrüng fester elastischer Körper. *Journal fur die Reine und Angewandte Mathematik* **92**, 156–171, doi: 10.1515/crll.1882.92.156.

Höhner, D., Wirtz, S., Kruggel-Emden, H. & Scherer, V. (2011). Comparison of the multi-sphere and polyhedral approach to simulate non-spherical particles within the discrete element method: Influence on temporal force evolution for multiple contacts. *Powder Technology* **208**, No. 3, 643–656, doi: 10.1016/j.powtec.2011.01.003.

Houlsby, G. T. (2009). Potential particles: A method for modelling non-circular particles in DEM. *Computers and Geotechnics* **36**, No. 6, 953–959, doi: 10.1016/j.compgeo.2009.03.001.

Huang, X., Hanley, K. J., O'Sullivan, C. & Kwok, C.-Y. (2017). Implementation of rotational resistance models: A critical appraisal. *Particuology* **34**, 14–23, doi: 10.1016/j.partic.2016.08.007.

Hunter, J. D. (2007). Matplotlib: A 2D graphics environment. *Computing in Science & Engineering* **9**, No. 3, 90–95, doi: 10.1109/MCSE.2007.55.

Johnson, K. L. (1985). *Contact Mechanics*. Cambridge: Cambridge University Press, doi: 10.1017/CBO9781139171731.

Kawamoto, R., Andò, E., Viggiani, G. & Andrade, J. E. (2016). Level set discrete element method for three-dimensional computations with triaxial case study. *Journal of the Mechanics and Physics of Solids* **91**, 1–13, doi: 10.1016/j.jmps.2016.02.021.

Kildashti, K., Dong, K., Samali, B., Zheng, Q. & Yu, A. (2018). Evaluation of contact force models for discrete modelling of ellipsoidal particles. *Chemical Engineering Science* **177**, 1–17, doi: 10.1016/j.ces.2017.11.004.

Kloss, C., Goniva, C., Hager, A., Amberger, S. & Pirker, S. (2012). Models, algorithms and validation for opensource DEM and CFD–DEM. *Progress in Computational Fluid Dynamics, an International Journal* .

Knowles, J., Ma, Y. & Evans, T. M. (2021). DEM modelling of 3D polyhedra with applications to gabion rockfall barriers. *EPJ Web of Conferences* **249**, 14008, doi: 10.1051/epjconf/202124914008.

Kodam, M., Bharadwaj, R., Curtis, J., Hancock, B. & Wassgren, C. (2010). Cylindrical object contact detection for use in discrete element method simulations. Part I – Contact detection algorithms. *Chemical Engineering Science* **65**, No. 22, 5852–5862, doi: 10.1016/j.ces.2010.08.006.

Kruggel-Emden, H., Rickelt, S., Wirtz, S. & Scherer, V. (2008). A study on the validity of the multi-sphere Discrete Element Method. *Powder Technology* **188**, No. 2, 153–165, doi: 10.1016/j.powtec.2008.04.037.

Kumar, R., Sarkar, A., Ketterhagen, W., Hancock, B., Curtis, J. & Wassgren, C. (2018). Influence of normal contact force model on simulations of spherocylindrical particles. *AIChE Journal* **64**, No. 6, 1986–2001, doi: 10.1002/aic.16082.

Lai, Z., Chen, Q. & Huang, L. (2022). Machine-learning-enabled discrete element method: Contact detection and resolution of irregular-shaped particles. *International Journal for Numerical and Analytical Methods in Geomechanics* **46**, No. 1, 113–140, doi: 10.1002/nag.3293.

Lin, X. & Ng, T.-T. (1995). Contact detection algorithms for three-dimensional ellipsoids in discrete element modelling. *International Journal for Numerical and Analytical Methods in Geomechanics* **19**, No. 9, 653–659, doi: 10.1002/nag.1610190905.

Liu, J. & Hanley, K. J. (2023). CFD–DEM modelling of the infiltration of non-spherical slurry particles in granular soils. *Computers and Geotechnics* **164**, 105845, doi: 10.1016/j.compgeo.2023.105845.

Lu, G., Third, J. R. & Müller, C. R. (2015). Discrete element models for non-spherical particle systems: From theoretical developments to applications. *Chemical Engineering Science* **127**, 425–465, doi: 10.1016/j.ces.2014.11.050.

Mahajan, V. V., Nijssen, T. M. J., Kuipers, J. A. M. & Padding, J. T. (2018). Non-spherical particles in a pseudo-2D fluidised bed: Modelling study. *Chemical Engineering Science* **192**, 1105–1123, doi: 10.1016/j.ces.2018.08.041.

Makse, H. A., Gland, N., Johnson, D. L. & Schwartz, L. M. (1999). Why effective medium theory fails in granular materials. *Phys. Review Lett.* **83**, No. 24, 5070–5073, doi: 10.1103/PhysRevLett.83.5070.

Marigo, M. & Stitt, E. H. (2015). Discrete Element Method (DEM) for Industrial Applications: Comments on Calibration and Validation for the Modelling of Cylindrical Pellets. *KONA Powder and Particle Journal* **32**, No. 0, 236–252, doi: 10.14356/kona.2015016.

Markauskas, D., Kačianauskas, R., Džiugys, A. & Navakas, R. (2010). Investigation of adequacy of multi-sphere approximation of elliptical particles for DEM simulations. *Granular Matter* **12**, No. 1, 107–123, doi: 10.1007/s10035-009-0158-y.

Mcdowell, G. R. & Bolton, M. D. (2001). Micro mechanics of elastic soil. *Soils and Foundations* **41**, No. 6, 147–152, doi: 10.3208/sandf.41.6_147.

Nguyen, T. D. & Plimpton, S. J. (2019). Aspherical particle models for molecular dynamics simulation. *Computer Physics Communications* **243**, 12–24, doi: 10.1016/j.cpc.2019.05.010.

O'Donovan, J., O'Sullivan, C., Marketos, G. & Muir Wood, D. (2015). Analysis of bender element test interpretation using the discrete element method. *Granular Matter* **17**, No. 2, 197–216, doi: 10.1007/s10035-015-0552-6.

O'Sullivan, C. (2011a). Particle-Based Discrete Element Modeling: Geomechanics Perspective. *International Journal of Geomechanics* **11**, No. 6, 449–464, doi: 10.1061/(ASCE)GM.1943-5622.0000024.

O'Sullivan, C. (2011b). *Particulate discrete element modelling : A geomechanics perspective*. 1st ed.. edn., Applied Geotechnics ; v. 4, London ; New York: Spon Press/Taylor & Francis.

Otsubo, M., O'Sullivan, C., Hanley, K. J. & Sim, W. W. (2017). The influence of particle surface roughness on elastic stiffness and dynamic response. *Géotechnique* **67**, No. 5, 452–459, doi: 10.1680/jgeot.16.P.050.

Park, E. H., Kindratenko, V. & Hashash, Y. M. A. (2021). Shared memory parallelization for high-fidelity large-scale 3D polyhedral particle simulations. *Computers and Geotechnics* **137**, 104008, doi: 10.1016/j.compgeo.2021.104008.

Podlozhnyuk, A., Pirker, S. & Kloss, C. (2017). Efficient implementation of superquadric particles in Discrete Element Method within an open-source framework. *Computational Particle Mechanics* **4**, No. 1, 101–118, doi: 10.1007/s40571-016-0131-6.

Pournin, L., Weber, M., Tsukahara, M., Ferrez, J.-A., Ramaioli, M. & Liebling, Th. M. (2005). Three-dimensional distinct element simulation of spherocylinder crystallization. *Granular Matter* **7**, No. 2, 119–126, doi: 10.1007/s10035-004-0188-4.

Rathbone, D., Marigo, M., Dini, D. & van Wachem, B. (2015). An accurate force–displacement law for the modelling of elastic–plastic contacts in discrete element simulations. *Powder Technology* **282**, 2–9, doi: 10.1016/j.powtec.2014.12.055.

Rojek, J., Oñate, E., Labra, C. & Kargl, H. (2011). Discrete element simulation of rock cutting. *International Journal of Rock Mechanics and Mining Sciences* **48**, No. 6, 996–1010, doi: 10.1016/j.ijrmms.2011.06.003.

Santamarina, J. C. & Cascante, G. (1996). Stress anisotropy and wave propagation: A micromechanical view. *Canadian Geotechnical Journal* **33**, No. 5, 770–782, doi: 10.1139/t96-102-323.

Sassel, T. S., Patino-Ramirez, F., Hanley, K. J. & O'Sullivan, C. (2023). Linking the macro-scale response of granular materials during drained cyclic loading to the evolution of micro-structure, contact network and energy components. *Granular Matter* **25**, No. 2, 23, doi: 10.1007/s10035-023-01308-z.

Shire, T., O'Sullivan, C. & Hanley, K. J. (2016). The influence of fines content and size-ratio on the micro-scale properties of dense bimodal materials. *Granular Matter* **18**, No. 3, 52, doi: 10.1007/s10035-016-0654-9.

Soltanbeigi, B., Podlozhnyuk, A., Papanicolopulos, S.-A., Kloss, C., Pirker, S. & Ooi, J. Y. (2018). DEM study of mechanical characteristics of multi-spherical and superquadric particles at micro and macro scales. *Powder Technology* **329**, 288–303, doi: 10.1016/j.powtec.2018.01.082.

Tang, X., Zakhvatayeva, A., Zhang, L., Wu, Z.-F., Sun, P. & Wu, C.-Y. (2020). Flow behaviour of pharmaceutical powders during rotary die filling with a paddle feeder. *International Journal of Pharmaceutics* **585**, 119547, doi: 10.1016/j.ijpharm.2020.119547.

Tatara, Y. (1989). Extensive Theory of Force-Approach Relations of Elastic Spheres in Compression and in Impact. *Journal of Engineering Materials and Technology* **111**, No. 2, 163–168, doi: 10.1115/1.3226449.

Tatara, Y. (1991). On compression of rubber elastic sphere over a large range of displacements – Part 1: Theoretical study. *Journal of Engineering Materials and Technology* **113**, No. 3, 285–291, doi: 10.1115/1.2903407.

Tatara, Y., Shima, S. & Lucero, J. C. (1991). On compression of rubber elastic sphere over a large range of displacements – Part 2: Comparison of theory and experiment. *Journal of Engineering Materials and Technology* **113**, No. 3, 292–295, doi: 10.1115/1.2903408.

Thornton, C., Cummins, S. J. & Cleary, P. W. (2011). An investigation of the comparative behaviour of alternative contact force models during elastic collisions. *Powder Technology* **210**, No. 3, 189–197, doi: 10.1016/j.powtec.2011.01.013.

Walton, K. (1987). The effective elastic moduli of a random packing of spheres. *Journal of The Mechanics and Physics of Solids* **35**, No. 2, 213–226, doi: 10.1016/0022-5096(87)90036-6.

Wang, X., Yin, Z.-Y., Xiong, H., Su, D. & Feng, Y.-T. (2021). A spherical-harmonic-based approach to discrete element modeling of 3D irregular particles. *International Journal for Numerical Methods in Engineering* **122**, No. 20, 5626–5655, doi: 10.1002/nme.6766.

Wensrich, C. M. & Katterfeld, A. (2012). Rolling friction as a technique for modelling particle shape in DEM. *Powder Technology* **217**, 409–417, doi: 10.1016/j.powtec.2011.10.057.

Wu, C.-Y. (2001). *Finite element analysis of particle impact problems*. Ph.D. thesis, Aston University, Birmingham, UK.

Yang, C., Guo, J., Lian, J. & Wang, Z. (2020). Study on Microscopic Roadbed Grouting Mechanism Based on CFD-DEM Coupling Algorithm. *Mathematical Problems in Engineering* **2020**, e4948738, doi: 10.1155/2020/4948738.

Yang, J., Wu, C.-Y. & Adams, M. (2015). Numerical Modelling of Agglomeration and Deagglomeration in Dry Powder Inhalers: A Review. *Current Pharmaceutical Design* **21**, No. 40, 5915–5922, doi: 10.2174/1381612821666151008150845.

Yimsiri, S. & Soga, K. (2000). Micromechanics-based stress–strain behaviour of soils at small strains. *Géotechnique* **50**, No. 5, 559–571, doi: 10.1680/geot.2000.50.5.559.

Zhao, S., Zhang, N., Zhou, X. & Zhang, L. (2017). Particle shape effects on fabric of granular random packing. *Powder Technology* **310**, 175–186, doi: 10.1016/j.powtec.2016.12.094.

Zheng, H., Shi, Z., Shen, D., Peng, M., Hanley, K. J., Ma, C. & Zhang, L. (2021). Recent Advances in Stability and Failure Mechanisms of Landslide Dams. *Frontiers in Earth Science* **9**.

Zheng, Q., Zhou, Z. & Yu, A. (2013). Contact forces between viscoelastic ellipsoidal particles. *Powder Technology* **248**, 25–33, doi: 10.1016/j.powtec.2013.03.020.

Zhong, W., Yu, A., Liu, X., Tong, Z. & Zhang, H. (2016). DEM/CFD-DEM Modelling of Non-spherical Particulate Systems: Theoretical Developments and Applications. *Powder Technology* **302**, 108–152, doi: 10.1016/j.powtec.2016.07.010.

Appendix A

Kumar contact model evaluation

Spherocylinders were set to collide at 5 different angles in order to evaluate the model proposed by Kumar *et al.* (2018). Using the spherocylinder collision models introduced in Chapter 4, a comparison was drawn between the FEA results and the force response predicted by the contact model. The results are summarised in Figure A.1. The predicted force response displays good agreement with the FEA results obtained at low strains, yet the errors increase monotonically as the strain increases. This was expected since the method used to derive it could not be used for higher strains. As mentioned in Chapter 2, the FEA in Kumar *et al.* (2018) was performed quasi-statically and hence some artificial boundary conditions had to be imposed. At low strains their effect on the force responses is expected to be minimal, but for high strains further testing should be performed to evaluate the model's applicability. Overall, the proposed contact model for spherocylinders performs well at low strains based on the limited testing conducted.

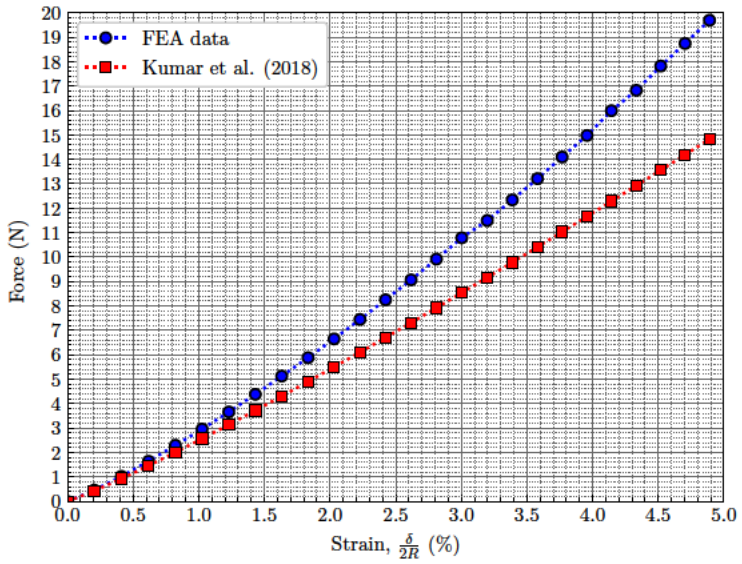

(a) Parallel spherocylinder collision comparison with Kumar

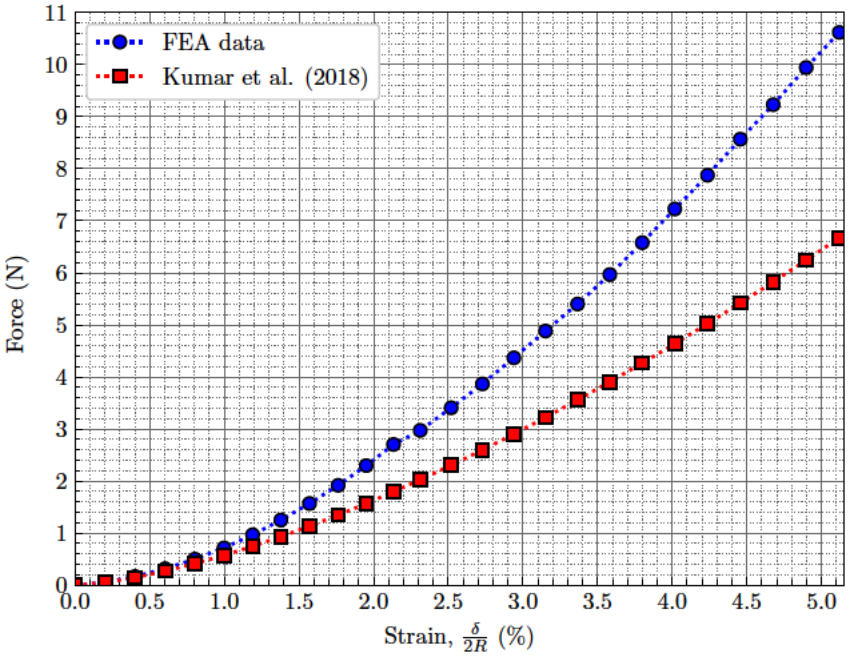

(b) 30° spherocylinder collision comparison with Kumar

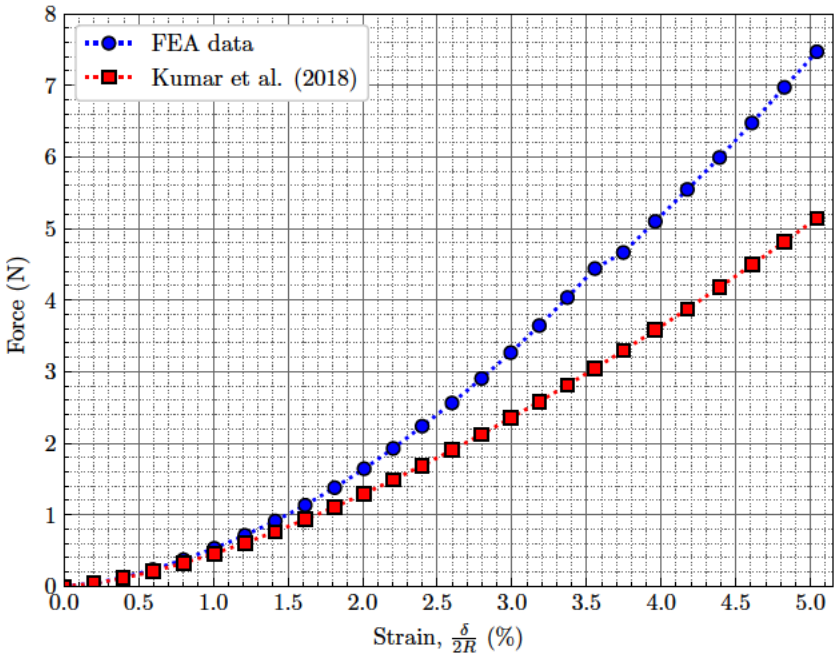

(c) 45° spherocylinder collision comparison with Kumar

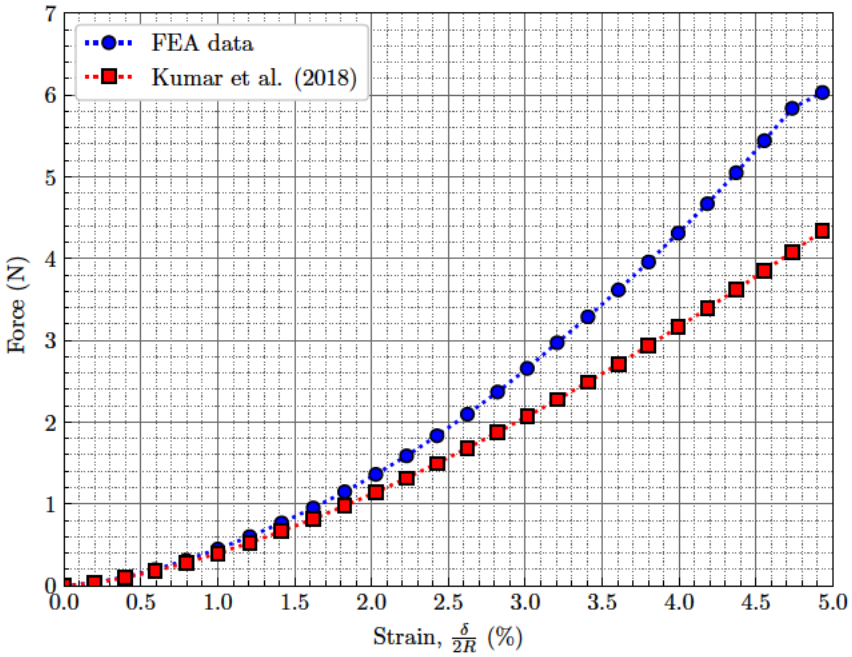

(d) 60° spherocylinder collision comparison with Kumar

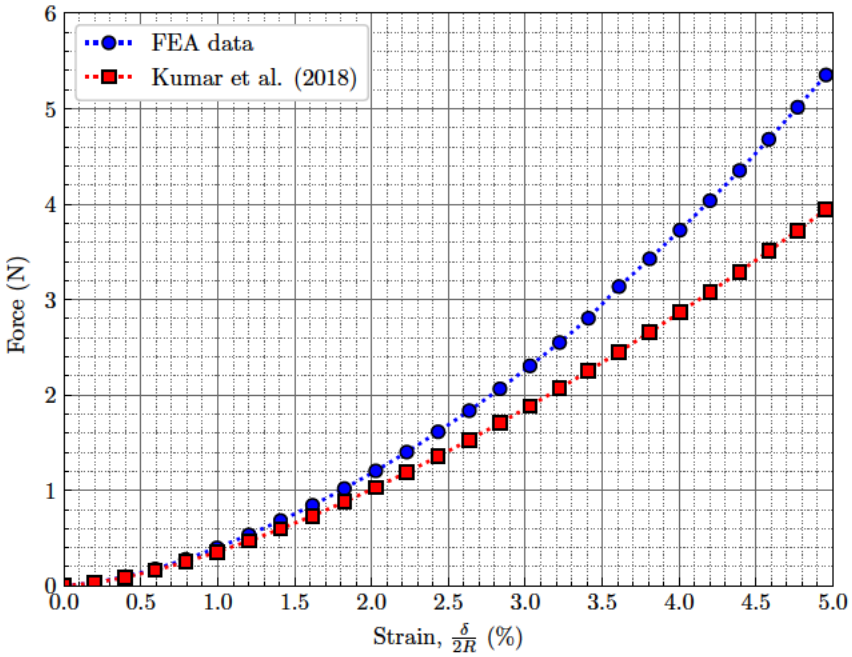

(e) 90° spherocylinder collision comparison with Kumar

Figure A.1: Force responses of spherocylinder collisions at various angles. Comparison between the FEA results and the contact model by Kumar *et al.* (2018).

Appendix B

Additional Abaqus set-up options

B.1 Step properties

The step types used were the *Static, General* for all the quasi-static compressions and the *Dynamic, Explicit* for all the kinematic collisions. The non-linear geometry option was always applied since there were large deformations present in the majority of the simulations performed and their effect should be taken into account.

B.2 Interaction properties

All interactions were defined as surface-to-surface contacts with the surface pairs pre-selected. Whenever present the plate was always acting as the *Master surface* and the granule was acting as the *Slave surface*.

Contact properties Hard contact was selected as the pressure-overclosure relationship for all cases, with a direct constraint enforcement method applied for the quasi-static compressions.

B.3 Overview of models

B.3.1 Uniaxial compressions

Assembly (Figure 3.3):

- Octant of granule (regardless of shape) modelled as a 3D deformable solid
- Rigid plate modelled as 3D rigid shell with a large enough radius to cover the entire length of the rod or as large as the radius of the sphere being compressed

Boundary conditions:

- Three planes of symmetry going through the center of the granule being compressed
- The plate is being displaced by a predefined distance towards the center of the granule

Mesh properties:

- Standard linear hexahedral elements: *C3D8R (8-node linear brick, reduced integration with hourglass control)*
- Distortion Control: *Off*
- Hourglass Control: *Default (included with element type)*

B.3.2 Kinematic collisions

Assembly (Figure 4.4): Two whole granules modelled as a 3D deformable solids.

Initial conditions: Both granules are given the same initial velocity but with opposite directions along the y-axis so that they collide vertically. The velocities are (iteratively) defined in order to achieve a specific maximum strain during the collision.

Mesh properties:

- Explicit linear hexahedral elements: *C3D8R (8-node linear brick, reduced integration with hourglass control)*
- Distortion Control: *On (length ratio = 0.1)*
- Hourglass Control: *Enhanced*

B.3.3 Indentations

Assembly (Figure 5.4):

- Axisymmetric slice of a sphere modelled as a deformable shell
- Rigid indenter modelled as a 3D analytical rigid shell

Boundary conditions:

- One plane of symmetry going through the center of the granule being compressed and perpendicular to the axis of symmetry (y-axis)
- The indenter is being displaced by a predefined distance towards the center of the granule

Mesh properties:

- Standard linear quadrilateral elements: *CAX4 (4-node bilinear axisymmetric)*
- Distortion Control: —
- Hourglass Control: —

B.3.4 Isotropic compressions

Assembly (Figure 6.4):

- Octant of sphere modelled as a 3D deformable solid
- Three rigid plates modelled as 3D rigid shells, each with a radius $R_plate = 0.5 \times R_sphere$

Boundary conditions:

- Three planes of symmetry going through the center of the sphere being compressed
- The plates are being displaced by a predefined distance towards the center of the sphere

Mesh properties:

- Standard quadratic hexahedral elements: *C3D20R (20-node quadratic brick, reduced integration)*
- Distortion Control: —
- Hourglass Control: —

Appendix C

Multi-Sphere DEM errors: additional figures

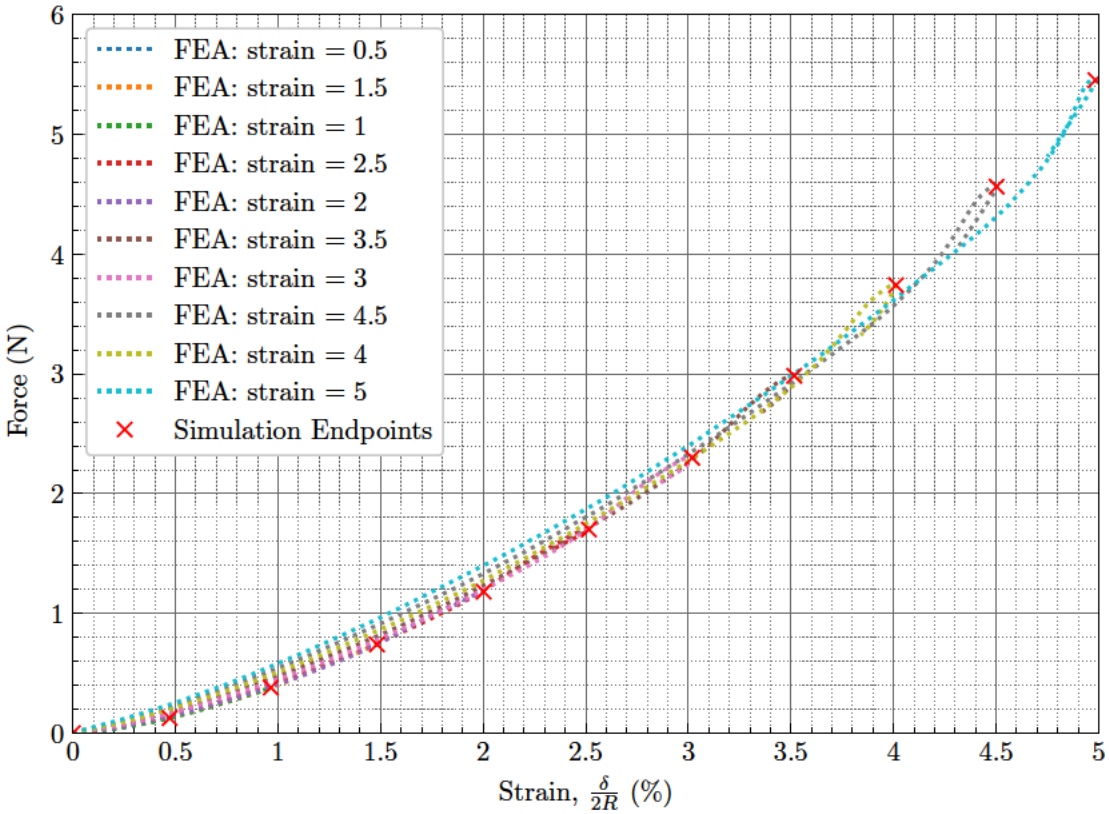

Figure C.1: Force–strain plots shown of the parametric study performed in order to obtain the force response of perfect spherocylinders colliding at a 90° angle. The endpoints of each simulation which contribute to the final force response of the specific contact scenario are also shown.

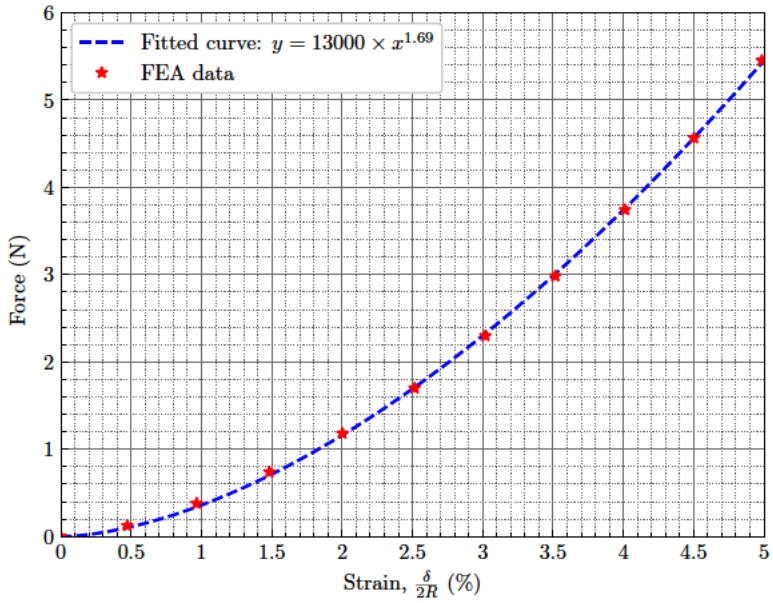

Figure C.2: Example of curve fitting performed for the Fixed-Length Rod collisions at 90° for more accurate comparison of the force response of the perfect spherocylinder and the FLRs

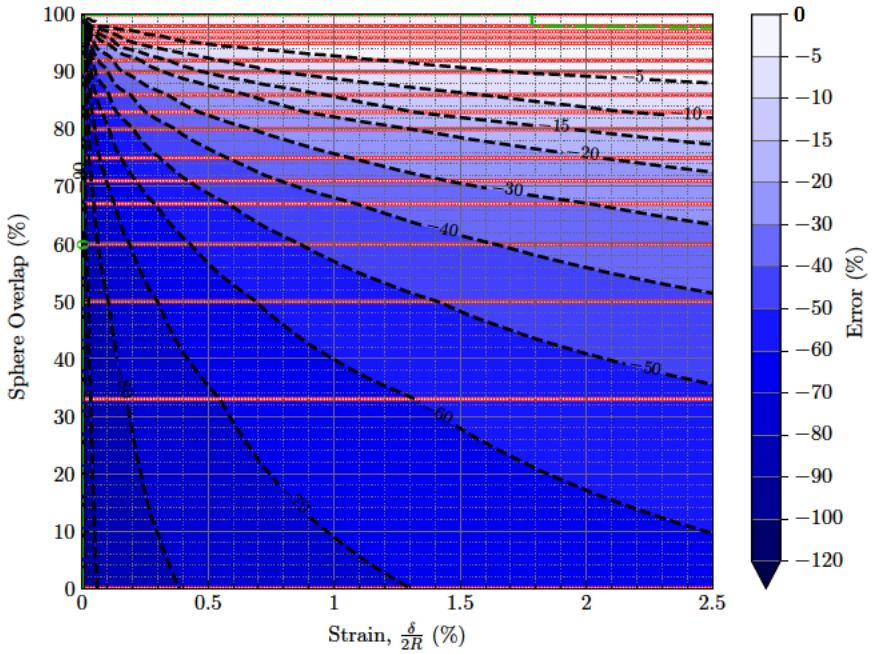

Figure C.3: Fixed-Length Rod parallel contact contour plot displaying the location of all datapoints where errors were calculated.

Appendix D

Smooth Cone contact

D.1 Smooth cone measurements

Calculations for the smooth cone volume overlap and contact area are given below for the two different cases, when viewed from a DEM perspective; (i) the overlap of the granule and smooth cone is limited to the spherical tip of the cone and (ii) when the overlap surpasses the spherical tip and reaches the body of the cone as well. The two cases are indicated in Figures D.1a and D.1b respectively. While two indenters were used in the simulations, the figures just show a single indenter for clarity. As the cone moves towards the center of the sphere D, the transition between the two cases happens when the chord EF exceeds the distance GH.

During the setup of the simulations, the following dimensions are known: The radius of the sphere on the smoothed cone tip, denoted by r, as well as the radius of the spherical granule, denoted by R. The angles θ and ϕ as shown in Figures D.1 are also given. Through the simulations the deformation δ — or distance overlap in DEM terms — is obtained. The distance between the centers of the two spheres CD is denoted by d, and is given by Equation D.1:

$$d = R + r - \delta \tag{D.1}$$

D.1.1 Spherical overlap

For the first case, shown in Figures D.1a, the volume overlap of the two spheres was calculated by using the Equation D.2:

$$V_{\text{Sphere-Sphere Intersection}} = \frac{\pi \left(R + r - d\right)^2 \left(d^2 + 2d\left(r + R\right) - 3\left(r - R\right)^2\right)}{12d} \tag{D.2}$$

As for the surface area of the contact, it was calculated using the following equation:

$$A_{\text{Spherical Cap}} = 2\pi r h \tag{D.3}$$

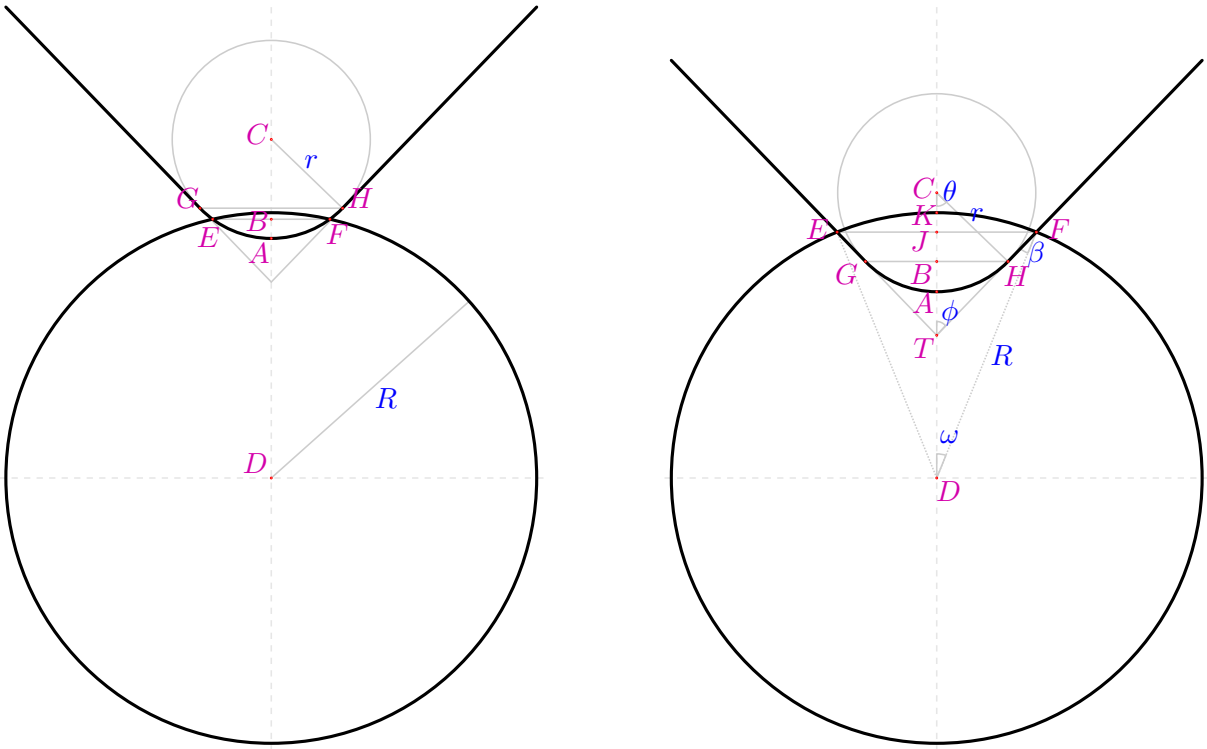

Figure D.1: Contact between a spherical granule and a smoothed cone from a DEM perspective. In (a) the overlap is limited to the spherical tip of the cone, whereas in (b) the conical body also overlaps with the granule.

where the height of the spherical cap of the smaller sphere h, denoted by the distance AB in the figure, was calculated using:

$$h_{\text{Spherical Cap}} = \frac{(R - r + d)(R + r - d)}{2d} \tag{D.4}$$

D.1.2 Overlap beyond spherical tip of cone

Starting from distance BH in Figure D.1b and AB:

$$BH = r \sin\theta \tag{D.5}$$

$$AB = r\,(1 - \cos\theta) \tag{D.6}$$

In order to calculate the length TA use:

$$\cos\phi = \frac{AB + TA}{r \tan\theta} \Rightarrow TA = r \tan\theta \cos\phi - AB \tag{D.7}$$

For $h_{\text{Small Cone}}$ which is denoted by the distance TB:

$$h_{\text{Small Cone}} = TA + AB \tag{D.8}$$

$$TD = R - \delta - TA \tag{D.9}$$

where δ is the deformation of the sphere, also denoted by the distance AK. Then using sine rule to obtain angle β:

$$\frac{TD}{\sin\beta} = \frac{R}{\sin(180 - \phi)} \Rightarrow \sin\beta = \frac{TD}{R}\sin\phi \tag{D.10}$$

In order to calculate the length JF use:

$$\omega = \phi - \beta \tag{D.11}$$

$$JF = R \sin\omega \tag{D.12}$$

$$h_{\text{Large Cone}} = \frac{JF}{\tan\phi} \tag{D.13}$$

$$h_{\text{Frustum}} = h_{\text{Large Cone}} - h_{\text{Small Cone}} \tag{D.14}$$

$$KJ = R - TD - h_{\text{Large Cone}} \tag{D.15}$$

where $h_{\text{Large Cone}}$ is denoted by TJ and h_{Frustum} is denoted by BJ.

Having obtained all the necessary values mentioned, the analytical contact volume overlap can be calculated from the addition of the volume of the conical frustum, and the volume of the two spherical caps. The volume of the frustum is given by the equation:

$$V_{\text{Frustum}} = \frac{\pi h}{3}\left(R^2 + Rr + r^2\right) = \frac{\pi(BJ)}{3}\left((JF)^2 + (JF)(BH) + (BH)^2\right) \tag{D.16}$$

The contact surface area can be calculated from the addition of the area of the spherical cap of the indenter and the curved area of a frustum given by Equation D.17:

$$A_{\text{Frustum}} = \pi L\left(R + r\right) = \pi L\left((JF) + (BH)\right) \tag{D.17}$$

where:

$$L^2 = h^2 + (R + r)^2 \Rightarrow L^2 = (BJ)^2 + \left((JF) + (BH)\right)^2 \tag{D.18}$$